Probabilistic Modeling of Brittle and Quasi-Brittle Fracture: First-Passage and Weakest-Link Analyses

A DISSERTATION
SUBMITTED TO THE FACULTY OF THE GRADUATE SCHOOL
OF THE UNIVERSITY OF MINNESOTA
BY

Zhifeng Xu

IN PARTIAL FULFILLMENT OF THE REQUIREMENTS
FOR THE DEGREE OF
DOCTOR OF PHILOSOPHY

Jia-Liang Le, Adviser

May 2019

Acknowledgements

First and foremost, I want to thank my adviser Professor Jia-Liang Le. It is my great honor to pursue my doctoral degree under his guidance. It is him who provided me with this precious opportunity to study at this university. He is my mentor of research, and even for future career. He taught me not only technical knowledge of probabilistic mechanics but also general research methodologies. I am grateful to him for his constant support and encouragement.

I want to express my gratitude to my committee members: Professor Ellad Tadmor, Professor Henryk Stolarski and Professor Otto Strack. Professor Tadmor guided me on the failure analysis of microelectromechanical systems structures and I was deeply touched by his passion for research. Professor Stolarski provided me with precious TA opportunities for two semesters. Professor Strack taught me tools for solving partial differential equations, which is of great value for my research.

Besides, I want to thank Ms. Jiahui Chen, Ms. Anna Gorgogianni, Ms. Anu Tripathi, Mr. Chen Hu, Dr. Feitao Zeng, Dr. Jianwen Peng, Dr. Lu Yu, Ms. Miaolin Fan, Mr. Rongsheng Chen, Mr. Qiming Zhu, Dr. Teng Man, Mr. Tianhao Yan, Ms. Ting Jiang, Mr. Weijian Jiao, Mr. Yuan Wang, for their friendship.

I also gratefully acknowledge the funding sources that made my Ph.D. study possible, which include the Department of Civil, Environmental and Geo-Engineering at the University of Minnesota, and the U.S. National Science Foundation. I thank the staff members in the Department of Civil, Environmental and Geo-Engineering at the University of Minnesota for their supports.

Last but not the least, I sincerely thank my father Yaohan Xu, my mother Xianmin Yin, my grandfather Yuming Yin, uncle Kun and uncle Yaowu for their supports.

Abstract

Reliability-based design of engineering structures aims to ensure an extreme low failure risk ($P_f \approx 10^{-6}$), which requires accurate predictions of the left tail of failure strength distributions. For determining the structural strength distribution, the probabilistic methods become the mainstream methods because they could characterize the strength distribution using a relatively small amount of data points. By contrast, the statistical methods, such as direct experimental testing or Monte Carlo simulations, are usually prohibited since an extremely large sample size is needed.

For ductile structures, the stress redistribution mechanism implies that the random structural strengths can be modeled by the Gaussian distribution. On the other hand, for brittle and quasi-brittle structures, the damage localization mechanism indicates that the structure can be represented by, in a statistical sense, a chain of material elements, which is referred to as the weakest-link model. The weakest-link model assumes that the failure of each material element is statistically independent. However, for modeling the strength statistics of some quasi-brittle structures, such as polycrystalline silicon (poly-Si) microelectromechanical systems (MEMS) structures, one needs to consider the spatially correlated features of both the random applied stress and the random material strength. The finite weakest-link model involves an intrinsic length scale for the discretization. However, the relationship between this length scale and material properties remains unclear. This research aims to resolve these fundamental issues of the conventional weakest-link model of failure statistics of brittle and quasi-brittle structures.

A continuous probabilistic model for the strength statistics of brittle and quasi-brittle structures is proposed based on the first-passage analysis of random fields,

which is referred to as the first-passage model. The first-passage model is derived in a 1-dimensional setting and is applied to the strength statistics of poly-Si MEMS structures. The failure of poly-Si MEMS structures is considered to be triggered by fracture initiation from the side-walls governed by a non-local failure criterion. The model is formulated within the contexts of both stationary and non-stationary random fields in order to consider different loading configurations. Through the comparison with the experimental data, it is shown that the model is able to yield accurate predictions on strength distributions of MEMS structures of different sizes using the same model parameters. The model is further used to predict the strength distribution of poly-Si MEMS beams under three-point-bending, and the result agrees well with the corresponding Monte Carlo simulation. The model predicts intricate size effects on both the structural strength distribution and the mean structural strength.

To improve the computational efficiency for predicting the strength distribution of MEMS devices, a renewal weakest-link model is developed. The model takes into account the detailed statistical information of the randomly distributed side-wall defects, which includes the random defect geometry, the random spacing between defects, and the local random material strength. The large-size asymptotic behavior of the model is derived based on the stability postulate. The comparison between the measured strength distributions of poly-Si MEMS specimens of different sizes and the corresponding model predictions shows that the model is capable of capturing the size-dependence of the strength distribution, which is essential for design extrapolations of MEMS devices across a wide size range.

The 1-dimensional first-passage model is generalized to higher dimensions. The generalized model is applied to the study of the origin of the power-law tail behavior of strength distribution of brittle and quasi-brittle structures. The model shows that the power-law behavior of the left tail of structural strength distribution stems from the left power-law tail of material strength distribution, which is also mildly affected

by the dimensionality of the analysis and the applied stress field. Flaw statistics (or the random stress field) introduces additional randomness to the structural strength, but does not dictate the power-law form of the tail distribution of structural strength.

Lastly, the relationship between the internal length scale of the finite weakest-link model and the material length scales is investigated by analyzing the size effect on the mean structural strength. The mathematical form of this relationship is derived through the dimensional analysis, and the relationship is calibrated by matching the size effect curves yielded by the finite weakest-link model and the stochastic finite element simulations. It is shown that the internal length scale of the finite weakest-link model can be explicitly related to the Irwin characteristic length and the crack band width.

Contents

List of Figures

Chapter 1

Introduction

Modern engineering structures need to be designed against an extreme low failure risk (e.g. a failure probability on the order of 10^{-6}) [24, 40]. This design objective requires accurate predictions of the left tail of strength distributions. In order to determine the distribution of structural strength, one can resort to either statistical methods or probabilistic methods[47, 38, 80, 8, 43]. However, the statistical methods, such as direct experimental testing or Monte Carlo simulations, are usually prohibited since an extremely large number of samples is required. The probabilistic methods become the mainstream methods for determining the structural strength distribution due to the ability to predict a low failure risk using a relatively small amount of data [98, 7, 24, 65, 101, 25].

The probabilistic methods are anchored by some mathematical models, and the corresponding model parameters to be determined by optimum fitting with experimental data [7, 25]. The fitting process can be regarded as a simplified method of maximizing the likelihood function, which ensures the obtained model parameters are optimal for the given data[91]. Probabilistic modeling centers at a valid mathematical model. However, choosing an empirical probabilistic model could be dangerous. Taking the fitting of the tensile strength distribution of polycrystalline silicon (poly-Si) microelectromechanical systems (MEMS) specimens as an example [85], as shown

in Figure 1.1, one can fit the experimental data with different probabilistic models equally good for the bulk part of the strength distribution, yet their predictions of the left tail part, which is of paramount importance for reliability-based design, can deviate from each other significantly [25]. To this end, the probabilistic model has to be developed based on the understanding of the failure mechanism of the structure as well as the corresponding statistical properties. In the following sections, we briefly review the existing probabilistic models for the strength statistics of ductile, brittle and quasi-brittle structures.

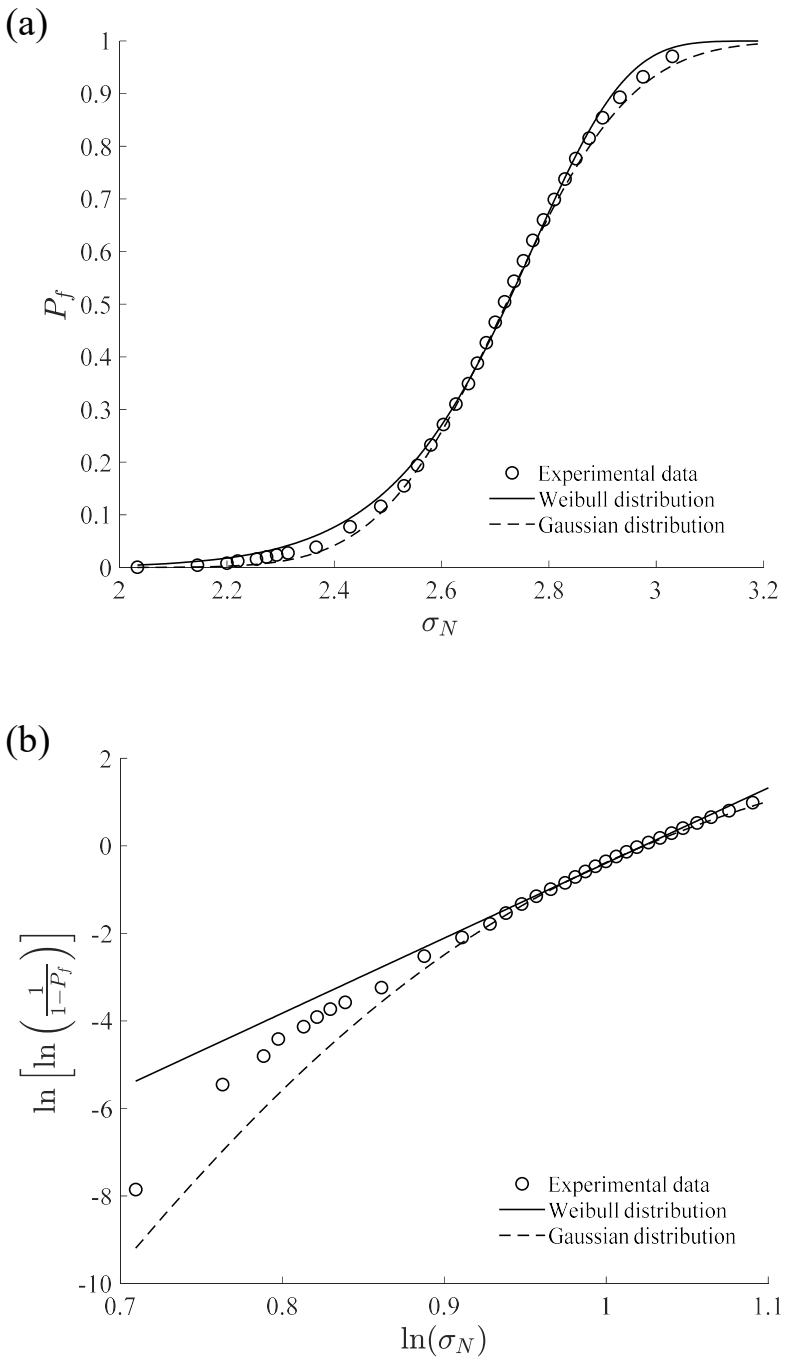

Figure 1.1: Optimum fittings for the tensile strength distribution of Poly-Si MEMS specimens: (a) linear scale, (b) Weibull scale.

1.1 Bundle model for strength statistics of ductile structures

The strength statistics of ductile structures can be modeled as a weighted sum of the random strength of material elements [75, 23]. Consider a ductile tensile specimen subjected to a nominal stress σ_N (shown in Figure 1.2 (a)). As shown in Figure 1.2 (b), the failure cross-section can be statistically modeled as a bundle of material elements, where the number of total material elements is a deterministic number n and the random strength of ith material element is represented by a random variable f_{t_i}. Since the material is ductile, each material element can sustain its peak load after failure (as shown in Figure 1.2 (c)). Consequently, the strength of the entire bundle, represented by σ_N, can be regarded as the weighted sum of the random strength of each material element, i.e.:

$$\sigma_N = \sum_{i=1}^{n} \omega_i f_{t_i} \tag{1.1}$$

where ω_i is a weighting factor, and each f_{t_i} is assumed to be statistically independent. Since the macro structure size is usually far grater than the size of material inhomogeneity, resulting in that the total element number n to be sufficiently large. From the central limit theorem[41, 9], we can obtain that

$$f_{\sigma_N}(x) = \frac{1}{\sqrt{2\pi}\delta} \exp\left[-\frac{(x-\mu)^2}{2\delta^2}\right] \tag{1.2}$$

where $f_{\sigma_N}(x)$ is the probability density function (PDF) of σ_N; μ, δ are the mean and the standard deviation of σ_N. Although Eq. (1.2) allows a negative value of x, which is not physically admissible, the probability of a negative value of x is negligibly small.

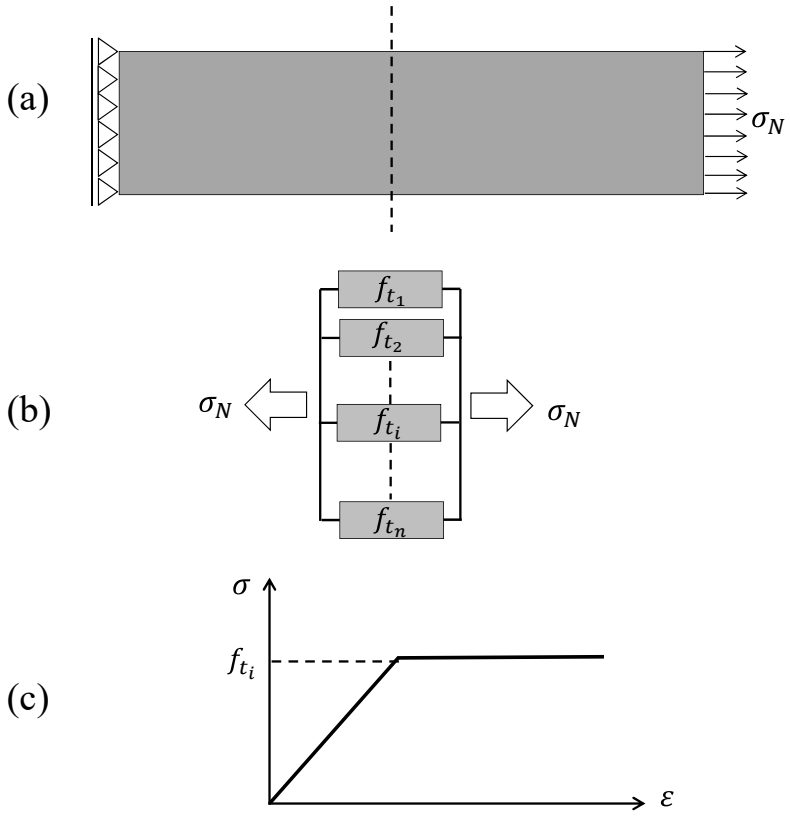

Figure 1.2: The bundle model for strength distribution of ductile structures:
(a) the loading configuration, (b) the bundle model, (c) the stress-strain curve of a material element.

1.2 Infinite weakest-link model for strength statistics of brittle structures

As shown in Figure 1.3 (a), the failure of brittle and quasi-brittle structures is featured by the damage localization mechanism [24], in which the failure of a macro-crack triggers the failure of the entire structure (under controlled load). Based on this failure mechanism, the strength statistics of brittle structures is usually modeled by a chain of material elements (shown in Figure 1.3 (b)). The total number of material elements n is considered to be a deterministic number, and the random strength of ith material element is represented by a random variable f_{t_i}. The failure criterion is that the failure of any material element in the chain will trigger the failure of the entire structure. As a result, the structural strength, represented by the random variable σ_N, is determined by the weakest material element in the chain, i.e:

$$\sigma_N = \min\{f_{t_i}, i = 1, 2, ...n\} \tag{1.3}$$

This model is therefore referred to as the weakest-link model.

By further assuming each f_{t_i} is independent and identically distributed (i.i.d.), the cumulative distribution function(CDF) of structural strength σ_N can be written as the following expression:

$$\begin{aligned} F_{\sigma_N}(x) &= \Pr.\left[\sigma_N = \min\{f_{t_i}, i = 1, 2, ...n\} < x\right] \\ &= \Pr.\left[\exists f_{t_i} < x, i = 1, 2, ...n\right] \\ &= 1 - \Pr.\left[\forall f_{t_i} > x, i = 1, 2, ...n\right] \\ &= 1 - \prod_{i=1}^{n} \left(1 - \Pr.\left[f_{t_i} < x\right]\right) \\ &= 1 - \left[1 - F_{f_t}(x)\right]^n \end{aligned} \tag{1.4}$$

where Pr.[·] represents the probability of event ·, and F_{f_t} is the CDF of f_{t_i}.

Moreover, for brittle structures, the size of damage localization zone or fracture process zone is usually negligibly small compared to the overall structural size. Consequently, the total number of material element n can be treated as infinite. In this case, the weakest-link model is further called the infinite weakest-link model, which has been widely used to describe the strength distribution of brittle structures.

In order to study the statistical properties of the infinite weakest-link model, the set $\{f_{t_1}, f_{t_2}, ..., f_{t_n}\}$ is regrouped into p number of subsets $\left\{f_{t_{j1}}, f_{t_{j2}}, ..., f_{t_{jm}}\right\}$, where $j = 1, 2, ...p$, and $n = mp$ (shown in Figure 1.3 (c)). Since $n \to \infty$ and p is finite, we have $m \to \infty$. From Eq. (1.4), the CDF of the minimum of a subsets is

$$F_{sub}(x) = 1 - [1 - F_{f_t}(x)]^m \tag{1.5}$$

By substituting Eq. (1.5) and the condition $n = mp$ into Eq. (1.4), we obtain

$$1 - F_{\sigma_N}(x) = [1 - F_{sub}(x)]^p \tag{1.6}$$

Since both $F_{\sigma_N}(x)$ and $F_{sub}(x)$ are the CDFs of the minimum of a set of infinite number of i.i.d. random variables, it is reasonable to assume that they share the same functional form, which implies that $F_{sub}(x)$ and $F_{\sigma_N}(x)$ differ by a linear transformation of the argument, i.e.:

$$F_{sub}(x) = F_{\sigma_N}\left(\frac{x-b}{a}\right) \tag{1.7}$$

Substituting Eq. (1.7) into Eq. (1.6) yields

$$1 - F_{\sigma_N}(x) = \left[1 - F_{\sigma_N}\left(\frac{x-b}{a}\right)\right]^p \tag{1.8}$$

The expression represented by Eq. (1.8) is referred to as the stability postulate [49]. It has been shown that, if $F_{\sigma_N}(x)$ is not a degenerating function, there are only three functions satisfying Eq. (1.8), which are:

$$F_{Gumbel}(x) = \exp\left\{-\exp\left[-\left(\frac{x-\mu}{s}\right)\right]\right\} \tag{1.9}$$

$$F_{Fréchet}(x) = \begin{cases} 0, & x < 0 \\ \exp\left[-\left(\frac{x}{s}\right)^{-m}\right], & x \geq 0 \end{cases} \tag{1.10}$$

$$F_{Weibull}(x) = \begin{cases} 1-\exp\left[-\left(\frac{x}{s}\right)^{m}\right], & x \geq 0 \\ 0, & x < 0 \end{cases} \tag{1.11}$$

where s, μ and m are three paramters, s and m are positive. These three distributions are referred to as the extreme value distributions [49, 51, 98, 59]. The distribution represented by $F_{Gumbel}(x)$ is referred to as the Gumbel distribution, or the Type I extreme value distribution; $F_{Fréchet}(x)$ represents the Fréchet distribution, or the Type II extreme value distribution; $F_{Weibull}(x)$ is the CDF of Weibull distribution, or the Type III extreme value distribution. In the Weibull distribution, m is referred to as the Weibull modulus, and s is referred to as the Weibull scale parameter. In the statistics of structural strength, the choice of which distribution should be applied is determined by the left-tail of $F_{\sigma_N}(x)$, which is referred to as the domain of attraction.

Experimental data has shown that the Weibull distribution is applicable for many different types of brittle structures [58, 97, 98]. One essential trait of the Weibull distribution is that its left tail is a power-law function, which can be seen by taking a limit of Eq. (1.11):

$$\lim_{x\to 0^+} \approx \left(\frac{x}{s}\right)^m \tag{1.12}$$

In the infinite weakest-link model, the size-dependence of structural strength dis-

tribution can be captured by treating s as a function of the structural size, i.e.:

$$s = \sigma_0 (V_N/V_0)^{-1/m} \tag{1.13}$$

where V_N is the structural size, V_0 is a defined unit size, σ_0 is a constant stress.

The explicit form of size-dependent Weibull type strength distribution can be obtained by substituting Eq.(1.13) into Eq. (1.11), i.e.:

$$F_{\sigma_N}(x) = 1 - \exp\left[-\frac{V_N}{V_0}\left(\frac{x}{\sigma_0}\right)^m\right],\ x \geq 0 \tag{1.14}$$

The size effect curve of the mean structural strength is defined as

$$\bar{\sigma}_N(D) = \int_0^\infty [1 - F_{\sigma_N}(x)]\,\mathrm{d}x \tag{1.15}$$

where D is a characteristic length of the structure, for example, the depth of a beam. The structural size can be related to this characteristic length through

$$V_n = cD^n \tag{1.16}$$

where c is a constant for the consideration of structural shape, and n is the dimensionality of the structure. The size-dependent structural strength yields a size-dependent mean structural strength. Substituting Eqs. (1.14) and (1.16) into Eq. (1.15) yields

$$\bar{\sigma}_N(D) = \left(\frac{V_n}{V_0}\right)^{-(1/m)} \bar{\sigma}_0 = \left[\left(\frac{c}{V_0}\right)^{-(1/m)} \bar{\sigma}_0\right] \cdot D^{-n/m} \tag{1.17}$$

where $\bar{\sigma}_0$ is a characteristic mean structural strength. Eq. (1.17) represents the Weibull size effect on the mean structural strength [24, 15]. Eq.(1.17) indicates that $\bar{\sigma}_N$ is a power-law decay function of D, whose exponent is $-n/m$.

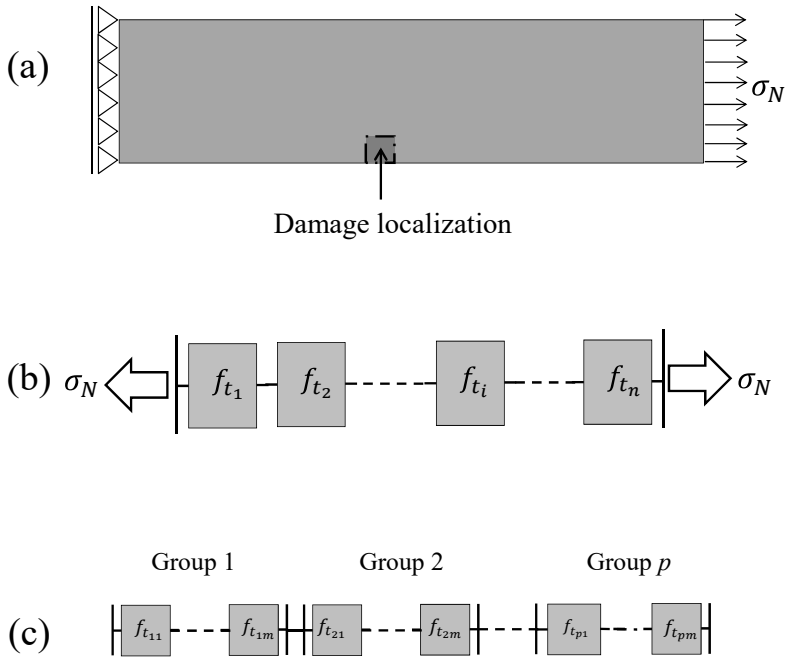

Figure 1.3: Illustration of the infinite weakest-link model: (a) the damage localization mechanism, (b) the weakest-link model, (c) the stability postulate.

1.3 Finite weakest-link model for strength statistics of quasi-brittle structures

Recent researches have focused on the structures made of quasi-brittle materials, such as concrete, composites, tough ceramics, rock, asphalt mixtures (at low temperatures), wood, etc [22, 23, 18, 67, 17]. The salient feature of quasi-brittle structures is that the size of the damage localization zone or fracture process zone is not negligibly small compared to the overall structural size, so that the total number of material elements in the weakest-link model must be finite. Therefore, the infinite weakest-link model is not applicable to quasi-brittle structures, and consistent deviation between the measured strength distributions of small and intermediate size specimens and the Weibull distribution has been observed (shown in Figure 1.4) [23, 26, 67, 71]. To this end, the finite weakest-link model was recently proposed, in which the structure is considered as a statistical chain of finite number of material elements. The material element of the finite weakest-link model is referred to as the representative volume element (RVE), which is defined as the smallest material element whose failure triggers the failure of the entire structure. The definition of RVE in the finite weakest-link model should be distinguished from the same terminology used in the conventional homogenization theory [61]. The structural strength is expressed in terms of the nominal stress σ_N, which is defined as follows:

$$\sigma_N = c_n P_{\max}/(bD) \tag{1.18}$$

$$\text{or} \quad \sigma_N = c_n M_{\max}/(bD^2) \tag{1.19}$$

where $P_{\max}, M_{\max}$ = maximum of the applied force or moment; D = characteristic size of the structure; b = width of the structure in the transverse direction; and c_n = constant, which can be conveniently chosen such that σ_N equals the maximum elastic

principal stress of a characteristic point in the structure. As shown in Figure 1.5 (a)-(c), for a beam subjected to three-point-bending, the nominal stress can be set equal to the maximum elastic principal stress at the middle of the bottom, i.e., $\sigma_N = 1.5\alpha P_{\max}/(bD)$, where $\alpha = L/D$; for a beam subjected to pure bending, the nominal stress can be set equal to the maximum elastic principal stress at the bottom, i.e., $\sigma_N = 6M_{\max}/(bD)$; for a beam subjected to uniaxial tension, the nominal stress can be set equal to maximum elastic principal stress at any point, i.e., $\sigma_N = P_{\max}/(bD)$.

As shown in Figure 1.6 (a)-(b), in the finite weakest-link model, the structure is divided into an assembly of a finite number of RVEs, in which the failure statistics of each RVE is also assumed to be statistically independent. For ith RVE, its strength and stress are regarded as two independent random variables, represented by f_{ti} and σ_i respectively. We can assume that the stress of each RVE, σ_i, is proportional to the nominal stress σ_N and use a spatial function to quantify it as follows:

$$\sigma_i = \sigma_N Z(\mathbf{x}_i) \tag{1.20}$$

where $\mathbf{x}_i$ is the spatial coordinate assigned to ith RVE, and Z is the dimensionless stress at point $\mathbf{x}_i$. At this junction, it should be pointed out that σ_i should be the effective stress that causes the material failure, which is usually not the maximum elastic principal stress at point $\mathbf{x}_i$. One convenient choice of σ_i is by treating it as the non-local stress, which can be regarded as the local average of the maximum elastic principal stress on a certain zone around point $\mathbf{x}_i$, and this zone is related to the damage localization zone or the fracture process zone [24, 17].

The failure criterion is that the RVE fails when its stress reaches its material strength, i.e. $\sigma_i = f_{ti}$, triggering the failure of the entire structure. As a result, the structural strength distribution, which equals the structural failure probability with

respect to the nominal stress σ_N, can be calculated as

$$F_{\sigma_N}(\sigma_N) = 1 - \prod_{i=1}^{m} \{1 - \Pr.[f_{ti} \leq \sigma_i = \sigma_N Z(\mathbf{x}_i)]\} = 1 - \prod_{i=1}^{m} \{1 - F_{f_t}[\sigma_N Z(\mathbf{x}_i)]\} \quad (1.21)$$

where m = equivalent number of RVEs in the structure, F_{f_t} = CDF of the RVE strength f_{ti}. It is noted that each f_{ti} is assumed to obey the same distribution.

In order to quantify the equivalent RVE number m, the RVE size, represented by l_0, is introduced. And Eq. (1.21) can be written as

$$F_{\sigma_N}(\sigma_N) = 1 - \prod_{i=1}^{c(D/l_0)^n} \{1 - F_{f_t}[\sigma_N Z(\mathbf{x}_i)]\} \quad (1.22)$$

where $m = c(D/l_0)^n$, n = dimensionality of the structure, c is a constant used to consider the influence of the structural shape. For uniaxial tensile specimens, since the stress at each point is identical, Eq. (1.22) can be further simplified as

$$F_{\sigma_N}(\sigma_N) = 1 - [1 - F_{f_t}(\sigma_N)]^{c(D/l_0)^n} \quad (1.23)$$

It is noted that Eq. (1.23) is in accordance with Eq. (1.4). As a result, we can expect that, for large-size structures, the strength distribution predicted by the finite weakest-link model is the Weibull distribution, which demonstrates that the finite weakest-link model is a generalization of the infinite weakest-link model.

In a series of recent studies [23, 18, 67], a functional form of the CDF of RVE strength was derived based on a multi-scale statistical model, which can be treated as a Gaussian distribution grafted with a Weibull distribution on the left tail. This type of distributions are usually referred to as the Gauss-Weibull grafted distribution:

$$F_{f_t}(x) = 1 - \exp\left[-(x/s_W)^{m_W}\right] \quad (x \leq \sigma_{gr}) \quad (1.24a)$$

$$F_{f_t}(x) = P_{gr} + \frac{r_f}{\sqrt{2\pi}\delta_G}\int_{\sigma_{gr}}^{x} e^{-(x-\mu_G)^2/2\delta_G^2}\mathrm{d}x \quad (x > \sigma_{gr}) \tag{1.24b}$$

where m_W, s_W = Weibull modulus and Weibull scale parameter of the Weibull tail, respectively; μ_G, δ_G = mean and standard deviation of the Gaussian bulk part; σ_{gr} = grafting point at which the Weibull tail terminates; $P_{gr} = F_{f_t}(\sigma_{gr})$ = grafting probability, which is usually on the order of 10^{-4} to 10^{-2}; and r_f = re-scaling parameter that ensures $F_{f_x}(+\infty) = 1$. Among the six parameters, only four are independent and the remaining two parameters can be determined by the integrity condition $F_{f_t}(\infty) = 1$ and the continuity condition $\mathrm{d}F_{f_t}(x)/\mathrm{d}\sigma|_{\sigma_{gr}^-} = \mathrm{d}F_{f_t}(x)/\mathrm{d}\sigma|_{\sigma_{gr}^+}$. The Gauss-Weibull grafted distribution of material strength was derived by using a multiscale stochastic model [18, 67, 17], in which the transition rate theory of random atom jumps and a hierachical probabilistic model are combined. It is shown that the strength of a nanoscale structure follows a power-law distribution [18, 67, 17]. As shown in Figure 1.6 (c), the failure statistics at the nano and macroscale are linked through a hierarchical model, which consists of both statistical chains and bundles. The hierarchical model predicts that the CDF of the strength of an RVE follows the aforementioned Gauss-Weibull grafted distribution. One essential point of the model is that it predicts a power-law tail of the material strength distribution, which stems from the mechanics of thermally activated random jumps of the nano-crack tip.

The finite weakest-link model is able to provide optimum fittings of the measured strength distribution of many different types of quasi-brittle structures [18, 67, 71, 17]. One salient feature of the finite weakest-link model is that it predicts a significant size effect on the structural strength distribution. Based on Eqs. (1.22), (1.24a) and (1.24b), it is evident that the distribution of the structural strength depends on the structure size. For small-size structures, the strength distribution is governed by the entire distribution of RVE strength, which should approach almost a Gaussian distribution according to Eqs. (1.24a) and (1.24b). At the large-size limit, the en-

tire structural strength distribution is primarily determined by the left tail of the distribution of RVE strength, which follows the Weibull distribution [97, 98, 59].

The size-dependence of the strength distribution leads to a size effect on the mean structural strength. By substituting Eq. (1.22) into Eq. (1.15), we obtain that

$$\bar{\sigma}_N(D) = \int_0^\infty \prod_{i=1}^{c(D/l_0)^n} \{1 - F_{f_t}[\sigma_N Z(\mathbf{x}_i)]\}\, \mathrm{d}x \tag{1.25}$$

Figure 1.7 depicts the size effect curve of the mean structural strength predicted by Eq. (1.25). It is seen that the entire size effect curve does not follow a power law due to the finiteness of the RVE number. As the structural size increases, the size effect behavior tends to approach the classical Weibull size effect (Eq. (1.17)), whose slope is equal to $-n/m_W$ [24, 15]. The entire size effect curve shown in Figure 1.7 is referred to as the statistical size effect curve for quasi-brittle structures [14, 15, 17], which can be fitted well by the following equation [68]:

$$\bar{\sigma}_N(L) = \mu_G \left[\frac{\eta_1 l_0}{L} + \left(\frac{\eta_2 l_0}{L} \right)^{r/q} \right]^{1/r} \tag{1.26}$$

where $\eta_1, \eta_2, r, q =$ constants.

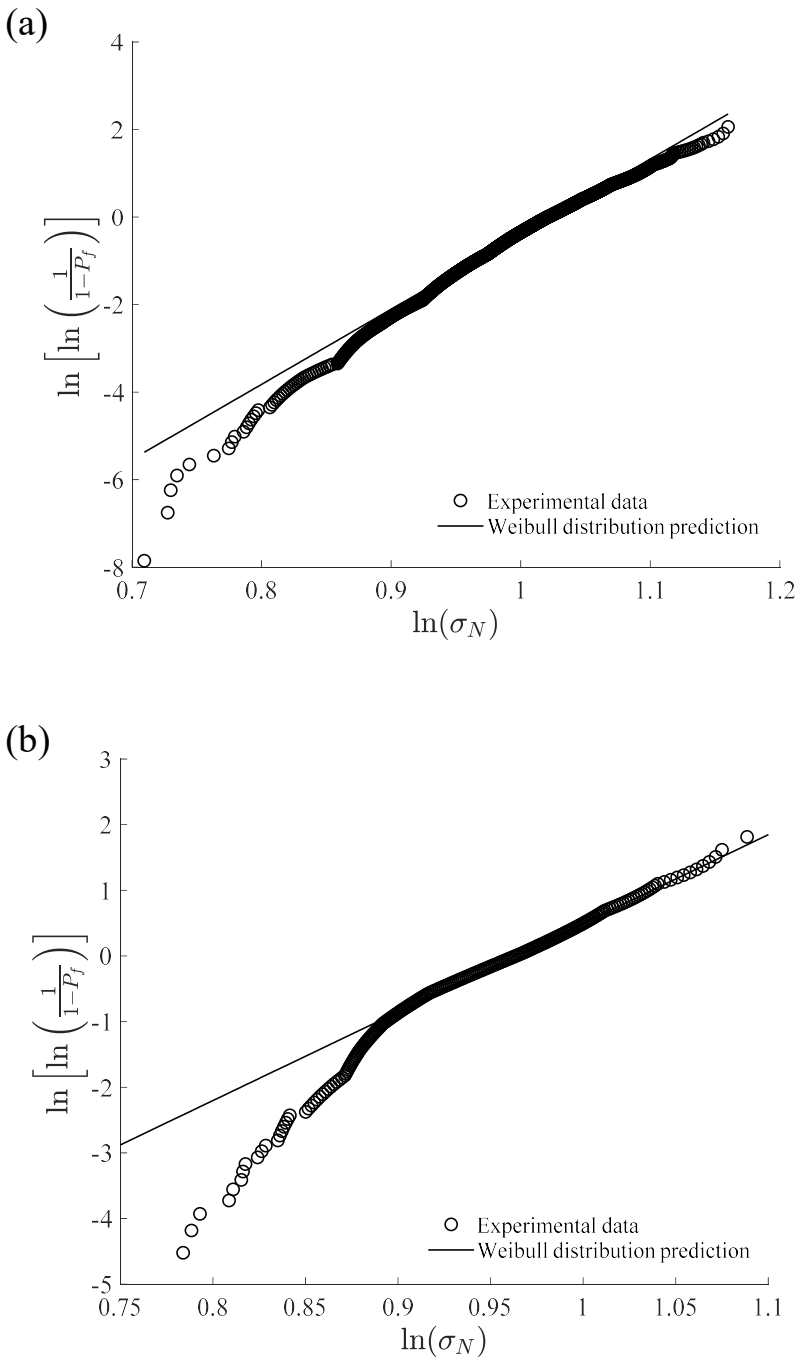

Figure 1.4: Optimum fittings for strength distributions of Poly-Si MEMS structures through the Weibull distribution: (a) gauge length = 20 μm, (b) gauge length = 70 μm.

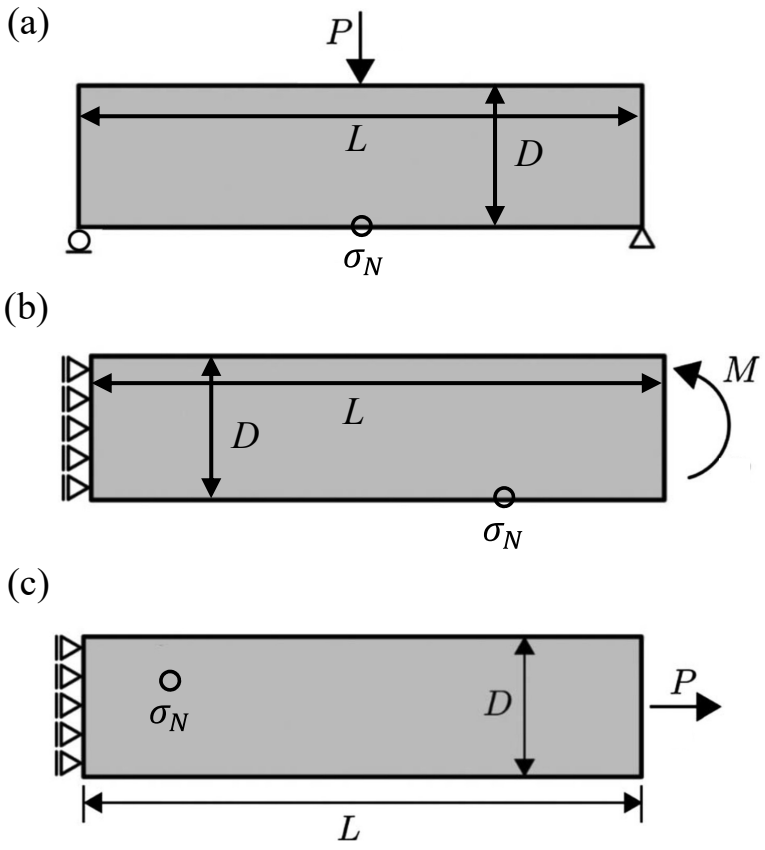

Figure 1.5: Nominal stress for different loading configurations: (a) three-point-bending, (b) pure bending, (c) uniaxial tension.

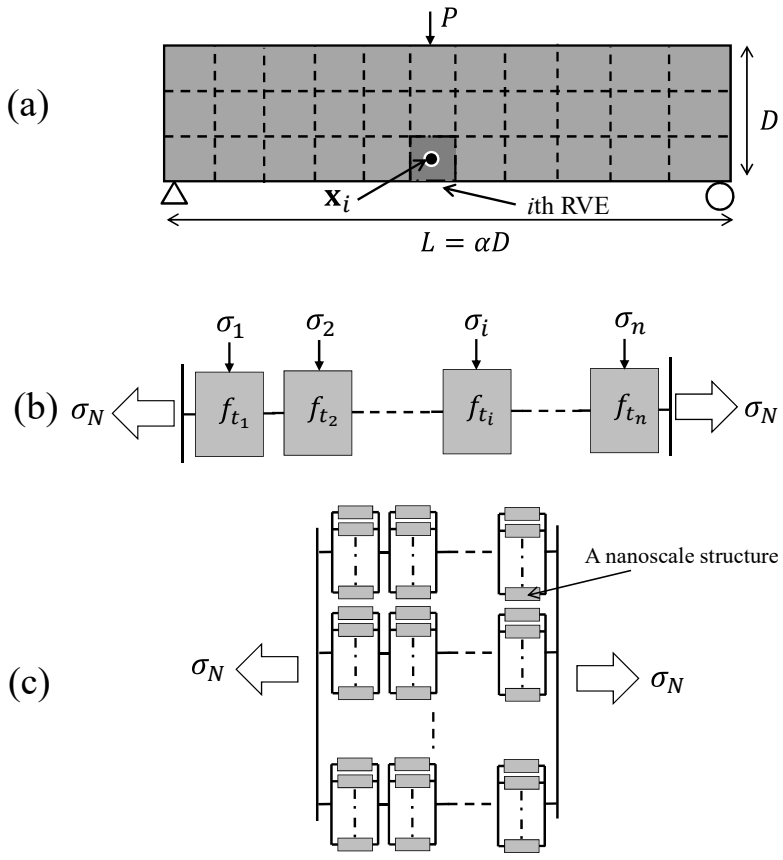

Figure 1.6: Formulation of the finite weakest-link model: (a) a typical quasi-brittle structure subjected to a load, (b) model formulation, (c) formulation of the RVE.

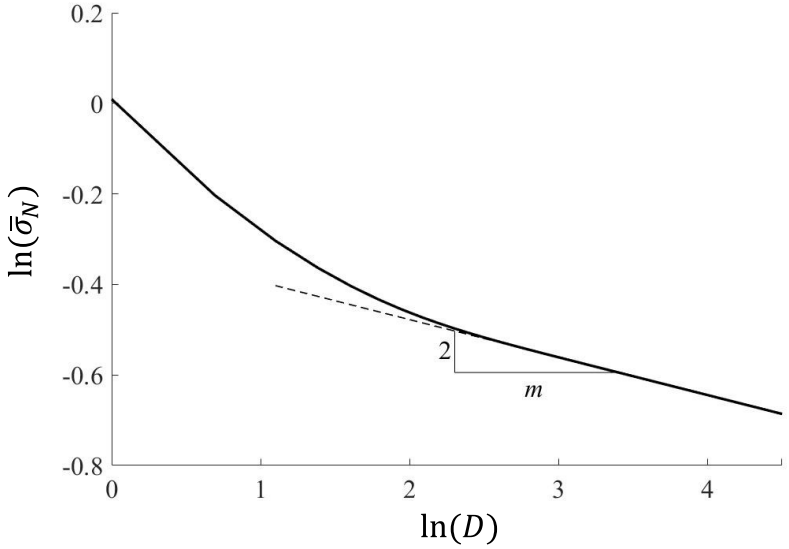

Figure 1.7: Size effect curve of the mean structural strength predicted by the finite weakest-link model.

1.4 Research motivation

Despite its successful application to structural strength statistics of many different types of brittle and quasi-brittle structures, the weakest-link model is essentially a simplified probabilistic model for the following reasons: 1) it cannot explicitly account for the spatially correlated features of the material strength and applied stress field; 2) the finite weakest-link model is a discrete model anchored by the concept of RVE, yet it is unclear how the RVE size is related to the material properties; 3) the origin of the power-law tail of structural strength distribution, which is a common phenomenon of many brittle and quasi-brittle structures, remains unclear.

To address the aforementioned problems, we developed two new probabilistic models for strength distributions of brittle and quasi-brittle structures [101, 102]. These models are designed to realistically incorporate the detailed statistical properties of both the applied stress and the material strength. Moreover, the relationship between RVE size and material properties is established through size effect analysis of the mean structural strength [73]. This thesis is organized in the following manner:

Chapter 2 presents a continuous probabilistic model based on the first-passage analysis of random fields. Here it is referred to as the first-passage model. The first-passage model is derived in a 1-dimensional setting and is applied to the structural strength statistics of poly-Si MEMS structures. MEMS is the integration of mechanical elements, sensors, actuators, and electronics on a common silicon substrate through the use of micro fabrication technology, whose size can vary from well below one micron to several millimeters. It is shown that the model is able to yield accurate predictions on strength distributions of MEMS structures of different sizes using the same model parameters [101].

Chapter 3 presents a renewal weakest-link model for the strength statistics of poly-Si MEMS structures. The model can be considered as a chain of material ele-

ments with varying sizes and reliabilities. The model takes into account the detailed statistical information of randomly distributed side-wall defects, which includes the defect geometry, spacing between defects, and the local random material strength. The large-size asymptotic behavior of the model is derived based on the stability postulate. Compared to the first-passage model, the renewal weakest-link model is much more efficient in terms of computational cost, while preserving some essential statistical features of randomly distributed side-wall defects [100].

In Chapter 4, the 1-dimensional first-passage model is generalized to higher dimensions. The generalized model is applied to investigate the origin of the power-law tail behavior of strength distribution of brittle and quasi-brittle structures. It is shown that the power-law behavior of the left tail of strength distribution of brittle and quasi-brittle structures stems from the left power-law tail of material strength distribution. The flaw statistics introduces additional randomness to the structural strength, but does not dictate the power-law form of its tail distribution [102].

Chapter 5 investigates the relationship between the RVE size of the weakest-link model and the material length scales through a size effect analysis on the mean structural strength. It is shown that the RVE size depends on both the Irwin characteristic length and the crack band width. It is demonstrated that the RVE size is not a material property, but a structural property [73].

Chapter 2

A First-Passage Model for the Failure Strength Distribution of Poly-Silicon MEMS Structures

2.1 Introduction

Microelectromechanical systems (MEMS) devices have been used in a variety of engineering applications such as medical technology, transportation systems, energy conversion and biochemical threat detection [78, 53, 99]. For devices that operate at high mechanical power densities or large deformation levels, an extremely low failure risk (e.g. a failure probability of 10^{-4}) is required [40, 79]. Experiments have shown that the strength of MEMS devices exhibits a considerable variability, which is believed to be caused by the randomness of the side-wall geometry induced by the fabrication process [30, 29, 84, 65]. It is suggested that, for stress analysis, the side-wall defects can be treated as V-shaped notches that are randomly distributed along the two side-walls [84].

The infinite weakest-link model has been widely used for strength distribution of MEMS structures, which predicts that the structural strength should obey the Weibull distribution [45, 30, 84, 50]. However, as shown in Figure 1.4, the Weibull

distribution deviates from the measured strength distribution of MEMS structures for small stress values [93, 45, 50, 65]. In order to improve the fitting of measured strength distribution, recent studies suggested to use the three-parameter Weibull distribution, which introduces a positive strength threshold to the infinite weakest-link model[30, 84]. Nevertheless, for the polycrystalline silicon (poly-Si) MEMS specimens tested in the laboratory, the basic assumption of the infinite weakest-link model, which requires the number of material elements appproaches infinity, is violated because the number of the side-wall defects is on the order of 10^2 to 10^3, which is too small to justify the extreme value theory [65, 101]. As a result, neither the Weibull distribution nor the three-parameter Weibull distribution can capture the measured strength distribution of poly-Si MEMS structures. Moreover, a series of recent studies showed that three-parameter Weibull distribution is not solid for the following three aspects: (1) the positive stress threshold, which is a key component of the three-parameter Weibull model, is theoretically unjustifiable since the transition rate theory suggests a zero strength threshold for material strength distrbutions [67]; (2) the model is not able to yield consistent model parameters for MEMS structures of different sizes [65]; (3) the model predicts an incorrect size effect on the mean structural strength at the large size limit [81, 46].

Recently, the finite weakest-link model was applied to the strength distribution of poly-Si MEMS structures [65]. In the model, the poly-Si MEMS structure is statististically modeled as a chain of representative volume elements (RVEs), where each RVE represents a segment containing a single V-notch at the middle (shown in Figure 2.1). The model incorporates the random geometry of side-wall grooves by allowing the opening angles and the depths of the V-notchs to be random variables. It is shown that, with a single set of model paramaters, the model is able to fit the measured strength distributions of MEMS structures of different sizes [65]. However, the finite weakest-link model involves three simplifications: (1) surface grooves are non-

interacting, (2) the total number of surface grooves for a given length of the side-wall is deterministic, (3) the material strength near the notch tip is statistically independent. Whereas the actual fabrication of MEMS specimens will inevitably introduce randomly spaced surface grooves, the total number of grooves for specimens of a given gauge length is a random variable [30, 29, 84]. The random spacing between surface grooves could lead to potential interactions between the two adjacent grooves. For closely spaced surface grooves, it is also necessary to consider the autocorrelated features of the random stress field and the random strength field, which cannot directly be handled by the weakest-link models [96]. As a result, a more general probabilistic model that can fully account for the spatially correlated statistical properties of both the random material strength and the random applied stress is needed.

This chapter presents a continuous probabilistic model for the strength statistics of MEMS structures based on the first-passage analysis of random fields [101]. The main feature of the model is that it accounts for the spatial interdependence of each point along the side-walls, which leads to a more physical description of the failure statistics of MEMS structures. This chapter is planned as follows: Section 2.2 presents the model formulation; Section 2.3 compares the model with the strength distributions of uniaxial tensile poly-Si MEMS specimens; Section 2.4 applies the model to poly-Si MEMS specimens under three-point-bending; Section 2.5 presents size effect analyses on both the structural strength distribution and the mean structural strength predicted by the model; and Section 2.6 discusses the relation between the present model and the conventional weakest-link statistical model.

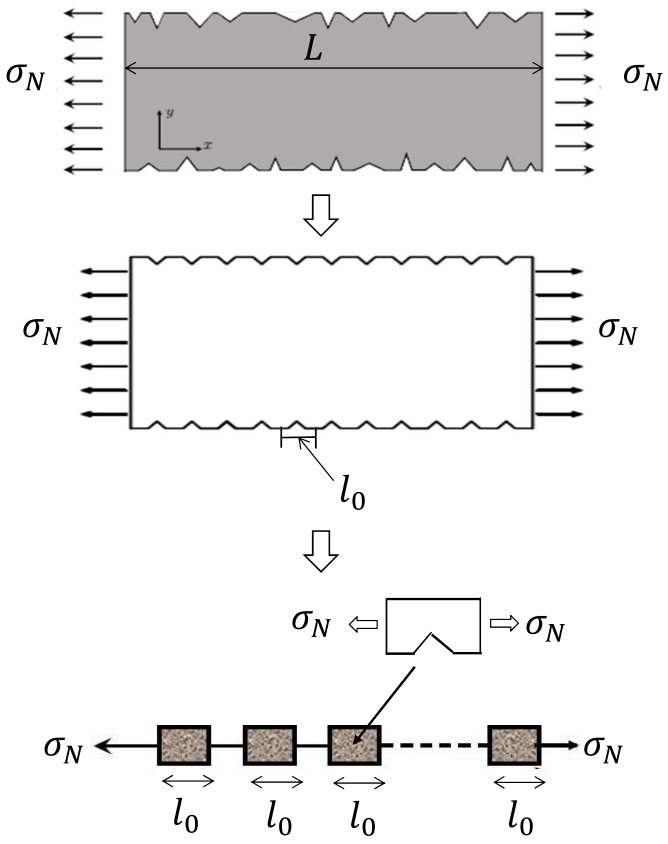

Figure 2.1: Illustration of the finite weakest-link model for the tensile strength statistics of poly-Si MEMS structures.

2.2 Model formulation

2.2.1 Basic model formulation for uniaxial tensile specimens

We first study uniaxial tensile MEMS specimens subjected to a far field stress σ_N, which is the most commonly used loading configuration for strength testing of MEMS structures. As shown in Figure 2.2 (a), the side-walls of the specimen contain randomly distributed surface grooves induced by the manufacturing process. Since the tensile specimen is of positive geometry (i.e. the stress intensity factor increases with the crack length) [23], it is reasonable to assume that the specimen reaches its peak load capacity once a marco-crack initiates and propagates from any point along the side-walls under controlled load. This means that the failure of any point along the side-walls will trigger the failure of the entire structure [23, 67]. Consequently, we may construct a 1-dimensional random field $\eta(x)$ to represent the failure statistics of any point along the side-wall. We consider that $\eta(x)$ measures the failure state of a point at coordinate x, where $\eta(x) < 0$ represents the failure. It is evident that the spatially correlated feature of the failure statistics of each point can be explicitly taken into consideration by the field $\eta(x)$. The simplest way to describe the failure state of a material point is:

$$\eta(x) = f_t(x) - \sigma(x) \tag{2.1}$$

where $f_t(x)$ = the random field of the material tensile strength; $\sigma(x)$ = the random field of the some stress measure to be defined.

For a given side-wall whose length is L, the CDF of the structural strength can be calculated as

$$F(\sigma_N, L) = 1 - \Pr.[\eta(x) > 0, \forall x] \tag{2.2}$$

As shown in Figure 2.2 (c), the probability represented by Eq. (2.2) is the probability that the random field $\eta(x)$ will down cross zero at least once.

Note that for a typical MEMS specimen (Figure 2.2 (a)), the distance between the opposite two side-walls is sufficiently large to ensure the failure statistics of each side-wall is independent. Therefore, the failure probability of the entire MEMS specimen can be written as

$$F_{\sigma_N}(\sigma_N, L) = 1 - [1 - F(\sigma_N, L)]^2 \tag{2.3}$$

A series of recently studies suggested that these surface grooves can be modeled as V-notches for the stress analysis [84, 85, 65]. To formulate the non-local stress field $\sigma(x)$ (shown in Figure 2.2 (a)- (b)), we first determine the maximum elastic tensile stress in the $y-$direction for any given coordinate x, and then compute the averaged stress of its neighborhood of within a length l_y, i.e.

$$\hat{\sigma}(x) = {l_y}^{-1} \int_{l_y} \sigma_{xx}(x, y) \mathrm{d}y \tag{2.4}$$

where $\sigma_{xx}(x, y)$ is the field of elastic stress in $x-$direction. By assigning l_y a value related to the size of the fracture process zone, Eq. (2.4) takes into account the damage localization mechanism of the corresponding fracture process zone. It is noted that this averaging process is necessary for formulating a strength-based failure criterion for a V-notch shaped defect since elastic stress at the notch tip is singular. To further account for the width of the fracture process zone, we introduce another non-local averaging for stress field $\sigma(x)$ in the $x-$direction:

$$\sigma(x) = \int_0^\infty \alpha(|x' - x|)\hat{\sigma}(x')\mathrm{d}x' \tag{2.5}$$

where $\alpha(r) = \left[1 - (r/\rho_0 l_x)^{2]}\right]^2$ ($\rho_0 \approx 0.82$), and $\sigma(x)$ is the stress field of Eq. (2.1).

Since the aforementioned stress analysis purely relies on linear elastic analysis, we can rewrite $\sigma(x)$ as

$$\sigma(x) = \sigma_N Z(x) \tag{2.6}$$

where $Z(x)$ = dimensionless stress field. It is evident that $Z(x)$ is a random field since it depends on the random geometry of the surface grooves. Meanwhile, the material tensile strength f_t is also subjected to a spatial variability.

It is noted that, for uniaxial tensile specimens, the randomness of the geometry of surface grooves does not have a spatial bias along the side-wall, and the material strength should not have a spatial bias either. Therefore, we consider both $Z(x)$ and $f_t(x)$ as stationary random fields. Consequently, the random field $\eta(x)$ (see Eq. (2.1)) is also a stationary random field. To compute the probability in Eq. (2.2), it is convenient to decompose these two random fields into their mean values and the corresponding random components:

$$f_t(x) = \mu_{f_t} + f_{t0}(x) \tag{2.7a}$$

$$Z(x) = \mu_z + Z_0(x) \tag{2.7b}$$

where μ_{f_t} and μ_Z are the mean values of $f_t(x)$ and $Z(x)$, respectively; $f_{t0}(x)$ and $Z_0(x)$ are the corresponding random components, whose mean values are zeros. As will be discussed in Section 2.4, the random field $f_t(x)$ can be simulated by using a prescribed marginal distribution and a prescribed correlation function, whereas the field $Z(x)$ can be obtained by stochastic finite element simulation. The stationarity

of $Z(x)$ can be examined by the following condition on the autovariance-ergodicity:

$$\Psi(\epsilon) = \lim_{l\to\infty} \frac{2}{l} \int_0^l \left(1 - \frac{\eta}{l}\right) \{\mathrm{E}\left[Z(x)Z(x+\epsilon)Z(x+\eta)Z(x+\epsilon+\eta)\right] - \\ -\mathrm{E}[Z(x)Z(x+\epsilon)]^2\}\mathrm{d}\eta = 0 \tag{2.8}$$

where $\mathrm{E}(\cdot)$ denotes the expectation operation. Note that, if we choose $\epsilon = 0$, Eq. (2.8) reduces to the condition for the ergodicity of the mean value.

Substituting Eqs. (2.7a) and (2.7b) into Eq. (2.2), the CDF of the tensile strength of the side-wall is obtained as

$$F(\sigma_N, L) = 1 - \Pr.\left[\eta_0(x) < \lambda,\ \forall x \in L\right] \tag{2.9}$$

where

$$\eta_0(x) = \sigma_N Z_0(x) - f_{t0}(x) \tag{2.10}$$

$$\lambda = \mu_{f_t} - \sigma_N \mu_Z \tag{2.11}$$

Following the foregoing analysis, it is obvious that $\eta_0(x)$ is a zero mean stationary field. Eq. (2.9) suggests that the failure probability of a sidewall equals the probability that the field $\eta_0(x)$ would exceed the up-crossing barrier λ at least once. This is a classical problem in probability, which is referred to as the first-passage probability (shown in Figure 2.2 (d)).

Since the random fields $Z_0(x)$ and $f_{t0}(x)$ are mutually independent, the marginal PDF of $\eta_0(x)$ can be calculated from the marginal PDFs of $Z_0(x)$ and $f_{t0}(x)$ through the following formula

$$f_{\eta_0}(\eta) = \int_{-\infty}^{+\infty} \sigma_N^{-1} f_{Z_0}(z/\sigma_N) f_{f_{t0}}(z-\eta)\mathrm{d}z \tag{2.12}$$

where $f_{Z_0}(x)$ and $f_{t0}(x)$ are the marginal PDFs of $Z_0(x)$ and $f_{t0}(x)$, respectively.

In order to compute the first-passage probability, we investigate the crossing rate μ_λ, which represents the mean number of crossings in a unit length. As a matter of course, we first investigate the number of up-crossings in the range $[0, 1]$. As shown in Figure 2.3 (a), the number of up-crossings is the number of up-crossing points x_c (marked by circles), where each x_c satisfies: (1) $\eta_0(x_c) = \lambda$, and (2) $\mathrm{d}\eta_0(x_c)/\mathrm{d}x > 0$. The total number of the up-crossing points is noted by n_c. Now we discretize the field by a spatial increment Δx (shown in Figure 2.3 (b)), where Δx is sufficiently small to ensure there exists no more than one up-crossing point in any grid, i.e., the probability of having a case shown Figure 2.3 (c) is negligible. The total number of sampled points is given by $m = 1/\Delta x$. Now we mark each grid with a index i, where $i = 0, 1, ..., m-1$. The grid containing an up-crossing point has the following traits:

$$\eta_0(i\Delta x) < \lambda \tag{2.13}$$

and

$$\eta_0\left[(i+1)\Delta x\right] > \lambda \tag{2.14}$$

If Δx is sufficiently small, with inequality (2.13), inequality (2.14) can be written as

$$\forall \dot{\eta_0}(i\Delta x) > 0, \eta_0\left[(i+1)\Delta x\right] \approx \eta_0(i\Delta x) + \dot{\eta_0}(i\Delta x)\Delta x > \lambda \tag{2.15}$$

where $\dot{\eta_0}(x) = \mathrm{d}\eta_0(x)/\mathrm{d}x$, which is the spatial derivative of the field $\eta_0(x)$. It is clear that inequality (2.15) is equivalent to the following inequality

$$\forall \dot{\eta_0}(i\Delta x) > 0, \eta_0(i\Delta x) > \lambda - \dot{\eta_0}(i\Delta x)\Delta x \tag{2.16}$$

Inequalities (2.13) and (2.16) are the conditions of an up-crossing point in the discrete formulation. Now we treat $\eta_0(i\Delta x)$ and $\dot{\eta}_0(i\Delta x)$ as two dependent random variables, and their joint PDF is $f_{\eta_0\dot{\eta}_0}(\eta,\dot{\eta})$. Therefore, the probability of sampling an up-crossing point is given by

$$P_n(\lambda,\Delta x)=\int_0^{\infty}\int_{\lambda-\dot{\eta}\Delta x}^{\lambda} f_{\eta_0\dot{\eta}_0}(\eta,\dot{\eta})\mathrm{d}\eta\mathrm{d}\dot{\eta} \tag{2.17}$$

Since the total number of points m equals $1/\Delta x$, the crossing rate, which equals the mean number of up-crossing points, is obtained as

$$\mu(\lambda,\Delta x)=E[n_c]=mP_n(\lambda,\Delta x)=\frac{1}{\Delta x}\int_0^{\infty}\int_{\lambda-\dot{\eta}\Delta x}^{\lambda} f_{\eta_0\dot{\eta}_0}(\eta,\dot{\eta})\mathrm{d}\eta\mathrm{d}\dot{\eta} \tag{2.18}$$

where $\mu(\lambda,\Delta x)$ is the crossing rate evaluated by using a grid line whose grid size is Δx. Eq.(2.18) represents the exact solution of the crossing rate for $\Delta x\to 0$, i.e.:

$$\mu_\lambda=\int_0^{\infty}\dot{\eta}f_{\eta_0\dot{\eta}_0}(\lambda,\dot{\eta})\mathrm{d}\dot{\eta} \tag{2.19}$$

It should be noted that Eq. (2.19) is the famous Rice's formula for crossing rate [86].

Now we consider a case where $\eta_0(x)$ crosses a sufficiently high barrier λ, where the length that $\eta_0(x)$ staying above λ can be treated as a point (shown in Figure 2.4 (a)-(b)). A well-known approximation for the first-passage probability is obtained by considering each crossing as an independent Poisson arrival, whose Poisson intensity is just the crossing rate μ_λ [36]. Hence, the first-passage probability is mapped to the probability of having at least one arrival of the corresponding Poisson process, i.e.:

$$F(\sigma_N,L)\approx 1-\exp\left[\mu_\lambda L\right] \tag{2.20}$$

Vanmarke modified the model represented by Eq. (2.20) and proposed the follow-

ing formula for the first-passage probability estimation [94, 95]:

$$F(\sigma_N, L) \approx 1 - F_{\eta_0}(\lambda) \exp\left[-\frac{\mu_\lambda}{F_{\eta_0}(\lambda)} L\right] \tag{2.21}$$

In Vanmarke's formulation, as shown in Figure 2.4 (c) - (d), we first sample a starting point that is not belong to the excursion set (the portion of $\eta_0(x)$ staying above λ), whose probability is $F_{\eta_0}(\lambda)$. Then we discard the excursion set and put the rest parts together to form a new process, which is separated by the up-crossing points (shown in Figure 2.4 (e)). The new formed process is assumed to be a Poisson process, whose Poisson intensity is $\frac{\mu_\lambda}{F_{\eta_0}(x)}$. It is noted that now the Poisson intensity is increased from μ_λ to $\frac{\mu_\lambda}{F_{\eta_0}(\lambda)}$. This is because the portion of $\eta_0(x)$ staying above λ is discarded, which results in the mean spacing between crossings decreases from $\frac{1}{\mu_\lambda}$ to $\frac{F_{\eta_0}(\lambda)}{\mu_\lambda}$. It should be also noted that first-passage probability computed from Eq. (2.21) approaches that of Eq. (2.20) as λ increases.

In a general case, $\eta_0(x)$ can be a non-Gaussian random field. Therefore, $\eta_0(x)$ and $\dot{\eta}_0(x)$ may not be statistically independent. The joint PDF $f_{\eta_0\dot{\eta}_0}$ is usually unavailable, which makes the crossing rate μ_λ difficult to calculate. To circumvent this delima, the non-Guassian translation method is adopted [56]. The original non-Gaussian field $\eta_0(x)$ is transformed into a corresponding standard Gaussian field $Y(x)$ by matching their CDFs and covariance functions through the following relations:

$$\Phi\left[Y(x)\right] = F_{\eta_0}[\eta_0(x)] \tag{2.22}$$

$$R_{\eta_0}(\Delta x) = \int_{-\infty}^{+\infty} \int_{-\infty}^{+\infty} F_{\eta_0}^{-1}\left[\Phi\left(y_1\right)\right] F_{\eta_0}^{-1}\left[\Phi\left(y_2\right)\right] \phi[y_1, y_2, R_Y(\Delta x)] \mathrm{d}y_1 \mathrm{d}y_2 \tag{2.23}$$

where $\Phi =$ standard Gaussian CDF; $\phi =$ standard bivariate Gaussian PDF; $F_{\eta_0}^{-1} =$ the inverse function of F_{η_0}; $R_{\eta_0}(\Delta x) = \mathrm{E}[\eta_0(x)\eta_0(x+\Delta x)]$, which is covariance function of $\eta_0(x)$; $R_Y(\Delta x) = \mathrm{E}[Y(x)Y(x+\Delta x)]$, which is covariance function of $Y(x)$. For

a standard Gaussian field, the field itself is statistically independent of the random field of its spatial derivative. Therefore, Eq. (2.19) can be approximately written as

$$\mu_\lambda \approx \phi(\lambda_Y) \int_0^\infty y' f_{\dot{Y}}(y') \mathrm{d}y' = \frac{\delta_{\dot{Y}}}{\sqrt{2\pi}} \phi(\lambda_Y) \tag{2.24}$$

where ϕ = standard Gaussian PDF; and $\delta_{\dot{Y}}$ = standard deviation of $\dot{Y}(x)$, $\dot{Y}(x) = \mathrm{d}Y(x)/\mathrm{d}x$. Based on Eq. (2.22), the equivalent barrier λ_Y of the translated standard Gaussian field is related to the original barrier λ by $\lambda_Y = \Phi^{-1}\left[F_{\eta_0}(\lambda)\right]$. The standard deviation $\delta_{\dot{Y}}$ can computed through the power spectrum density of $Y(x)$, i.e.:

$$\delta_{\dot{Y}} = \left[\int_{-\infty}^{\infty} \omega^2 S_Y(\omega) \mathrm{d}\omega\right]^{1/2} \tag{2.25}$$

where the power spectrum density $S_Y(\omega)$ can be expressed by

$$S_Y(\omega) = \lim_{l\to\infty} \mathrm{E}\left[\frac{1}{2\pi l}\left|\int_0^l Y(x) e^{-i\omega x} \mathrm{d}x\right|^2\right] \tag{2.26}$$

By using Eqs.(2.1)- (2.26), the tensile strength distribution of a poly-Si MEMS specimen can be obtained.

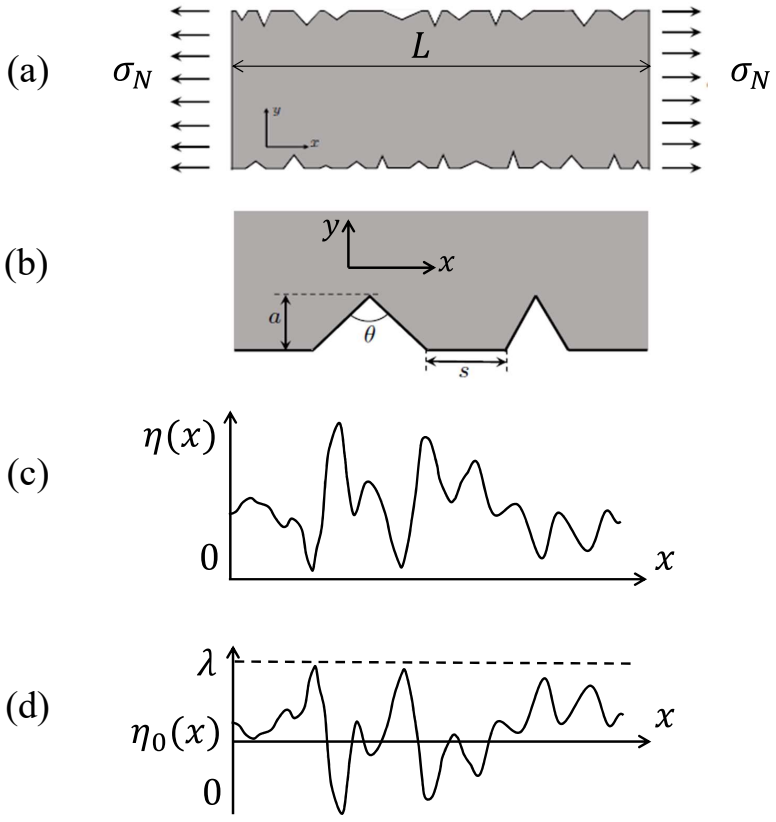

Figure 2.2: Illustration of the first-passage model: (a) schematic diagram of the poly-Si tensile specimen, (b) random geometry of the side-wall grooves modeled as V-notches, (c) first-passage analysis of the random field $\eta(x)$, (d) first-passage analysis of the zero mean stationary field $\eta_0(x)$.

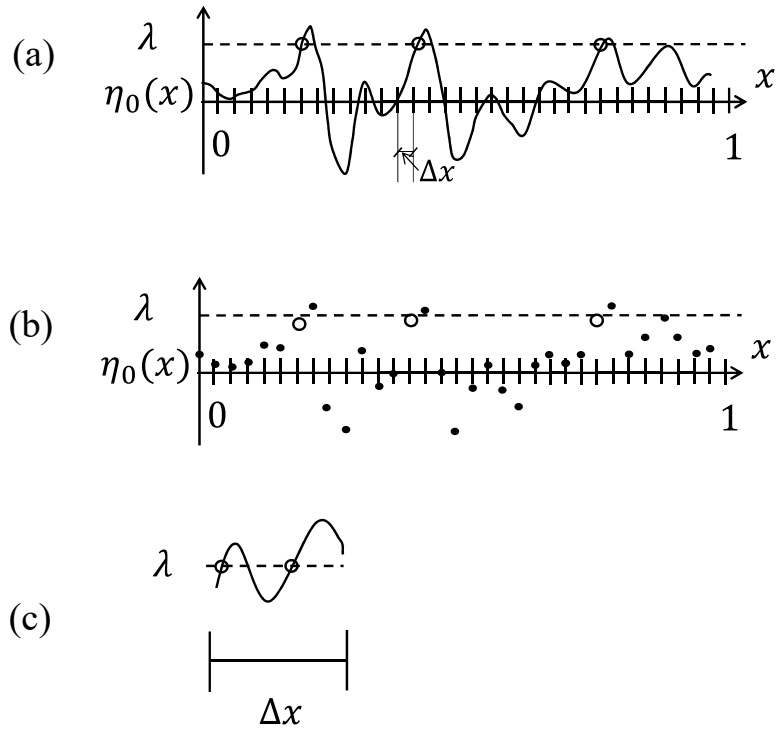

Figure 2.3: Illustration of the crossing rate: (a) a zero mean random field $\eta_0(x)$ with respect to an up-crossing barrier λ, (b) the discrete sampling of $\eta_0(x)$, (c) multiple crossings in a grid.

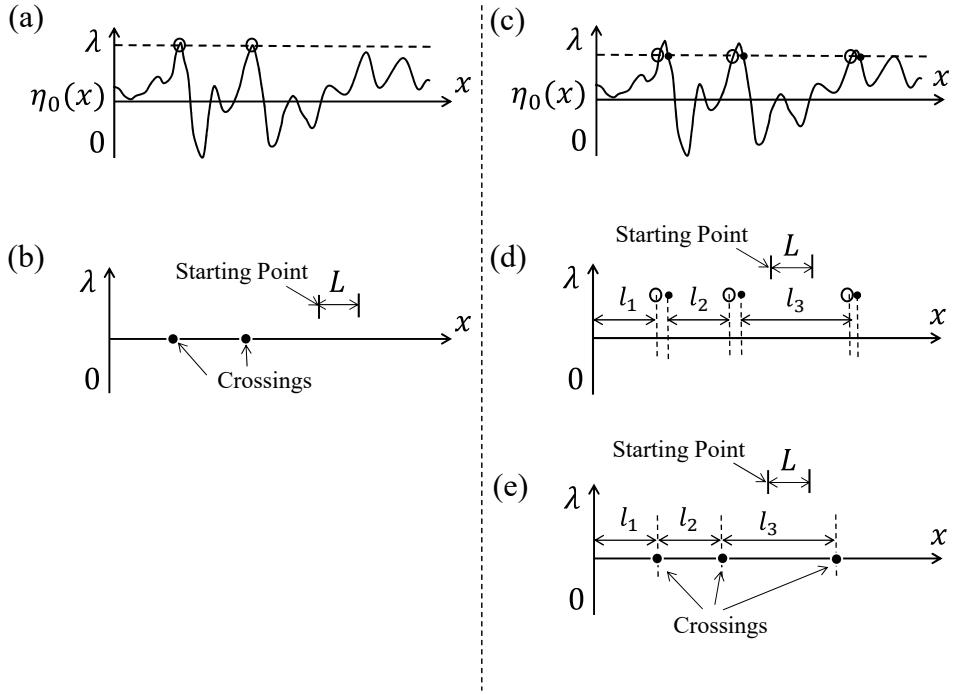

Figure 2.4: Illustration of first-passage analysis: (a) $\eta_0(x)$ up crosses a sufficiently high crossing barrier λ, (b) first-passage probability approximation via a Poisson process, (c) $\eta_0(x)$ up crosses a crossing barrier λ, (d) mapping of the crossing events, (e) the formulation of Vanmarcke's formula.

2.2.2 Extension to flexural specimens

The foregoing analysis is based on the assumption that the random field $\eta_0(x)$ is a stationary field, which is valid for the uniaxial tensile loading case. However, for other different loading configurations, such as three-point-bending specimens, the dimensionless stress field $Z(x)$ is non-stationary, making $\eta_0(x)$ to be a non-stationary random field. In order to account for flexural loading configurations, this section extends the model formulated in Section 2.2 to the non-stationary cases.

Consider the case that the non-local stress field $Z(x)$ is a non-stationary field while the strength field $f_t(x)$ remains a stationary field. Let $\sigma_N = P_{\max}/(bD)$ to be the structural strength of the specimen, where $P_{\max}$ = maximum load capacity, D = characteristic size of the specimen, b = width of the specimen in the transverse direction. Within the framework of linear elasticity, the non-local stress field can still be written as $\sigma(x) = \sigma_N Z(x)$. To apply the formulation of non-stationary random field, it is convenient to write the dimensionless stress field $Z(x)$ as the following form

$$Z(x) = \mu_Z(x)\,[1 + Z_0(x)] \tag{2.27}$$

where $\mu_Z(x)$ is the spatially varying mean of $Z(x)$, and $Z_0(x)$ is the corresponding random component that can be considered as a zero-mean non-stationary field. Similar to stationary case, the failure probability of the side-wall can be translated into the first-passage probability of a zero-mean non-stationary field $\eta_0(x)$ with respect to a spatially varying crossing barrier $\lambda(x)$ as:

$$\eta_0(x) = \sigma_N \mu_Z(x) Z_0(x) - f_{t0}(x) \tag{2.28a}$$

$$\lambda(x) = \mu_{f_t} - \sigma_N \mu_Z(x) \tag{2.28b}$$

In this case, Eq. (2.2) can be computed as

$$F(\sigma_N, L) \approx 1 - F_{\eta_0(0)}\left[\lambda(0)\right] \exp\left\{\int_0^L -\frac{\mu_\lambda(x)}{F_{\eta_0(x)}[\lambda(x)]}\mathrm{d}x\right\} \tag{2.29}$$

where $F_{\eta_0(x)}$ = marginal CDF of η_0 at coordinate x, $\mu_\lambda(x)$ = spatially varying crossing rate. Similar to Eq. (2.21), in the first-passage probability computation, Eq. (2.29) adopts a Poisson process grafted with a leading term $F_{\eta_0(0)}\left[\lambda(0)\right]$, where the Poisson intensity, $\frac{\mu_\lambda(x)}{F_{\eta_0(x)}[\lambda(x)]}$, is a spatially varying function.

By adopting the non-Gaussian translation method of non-stationary fields, the spatially varying crossing rate $\mu_\lambda(x)$ can also be estimated from the corresponding crossing rate of a family of stationary standard Gaussian fields, i.e.:

$$\mu_\lambda(x) = \int_0^\infty \dot{\eta} f_{\eta_0(x)\dot{\eta}_0(x)}[\lambda(x), \dot{\eta}]\mathrm{d}\dot{\eta} \approx \frac{\delta_{\dot{Y}}(x)}{\sqrt{2\pi}}\phi\left[\lambda_Y(x)\right] \tag{2.30}$$

where ϕ = standard Gaussian PDF, $f_{\eta_0(x)\dot{\eta}_0(x)}$ = joint PDF of $\eta_0(x)$ and $\dot{\eta}_0(x)$, which varies spatially; $\delta_{\dot{Y}}(x)$ = standard deviation of $\dot{Y}_x(x')$, in which $\dot{Y}_x(x') = \mathrm{d}Y_x(x')/\mathrm{d}x'$ and $Y_x(x')$ is a stationary field satisfying $Y_x(x) = \Phi^{-1}\left\{F_{\eta_0(x)}[\eta_0(x)]\right\}$; and $\lambda_Y(x) = \Phi^{-1}\left\{F_{\eta_0(x)}[\lambda(x)]\right\}$, which is the spatially varying crossing barrier of the translated standard Gaussian field $Y_x(x')$. The essense of the aforementioned method is to transform the non-stationary field into a family of stationary standard Gaussian field, where there is a unque stationary Guasian field $Y_x(x')$ at each coordinate x. The crossing rate $\mu_\lambda(x)$ at x can be approximated by crossing rate of $Y_x(x')$ with respect to $\lambda_Y(x)$. Since for each $Y_x(x')$, we can only determined its value at $x' = x$, this transformation procedure is a challenging task, which has attracted considerable attention over the past decade [37, 48, 62]. One viable method is formulated within the frame work of the evolutionary power spectral density [37].

The computational cost of Eq. (2.29) is expensive since it requires the evaluation of the spatially varying marginal CDF $F_{\eta_0(x)}$ as well as the spatially varying crossing

rate $\mu_\lambda(x)$. Therefore, it is desirable to introduce some approximation to simplify the analysis. The most straightforward simplification is to assume the dimensionless stress field $Z(x)$ as a uniformly modulated non-stationary field, in which the field $Z_0(x)$ in Eq. (2.27) can be treated as a stationary field. The stationarity of $Z_0(x)$ can be examined by the ergodicity check of $Z_0(x)$ using Eq. (2.8). In this case, the spatially varying marginal CDF of η_0 can be expressed as

$$F_{\eta_0(x)}(\eta) = \frac{1}{\sigma_N \mu_Z(x)} \int_{-\infty}^{\eta} \int_{-\infty}^{\infty} f_{Z_0}\left[\zeta/\sigma_N \mu_Z(x)\right] f_{f_{t0}}(\zeta - \eta') \mathrm{d}\zeta \mathrm{d}\eta' \tag{2.31}$$

It is obvious that Eq. (2.31) requires only the marginal CDF of the stationary field $Z_0(x)$. In order to compute the spatially varying crossing rate $\mu_\lambda(x)$, we can define a stationary field with respect to each different x, i.e.:

$$\eta_{0|x}(x') = \sigma_N \mu_Z(x) Z_0(x') - f_{t0}(x') \tag{2.32}$$

Similar to the method used in the stationary case, $\mu_\lambda(x)$ can be computed by the following formula:

$$\mu_\lambda(x) \approx \frac{\delta_{\dot{Y}_x}(x)}{\sqrt{2\pi}} \phi\left[\lambda_Y(x)\right] \tag{2.33}$$

where $\delta_{\dot{Y}_x}(x)$ is the standard deviation of the field $\dot{Y}_x(x') = \mathrm{d}Y_x(x')/\mathrm{d}x'$, and $Y_x(x') = \Phi^{-1}\left\{F_{\eta_0(x)}\left[\eta_{0|x}(x')\right]\right\}$; $\lambda_Y(x) = \Phi^{-1}\left\{F_{\eta_0(x)}\left[\lambda(x)\right]\right\}$, which is the translated spatially varying crossing barrier. These simplifications drastically reduce the computation effort for dealing with Eq. (2.30). As will be shown in Section 2.4, this approximation is reasonable for MEMS specimens under flexural loading configuration such as three-point-bending.

2.3 Experimental validation for the uniaxial tensile specimens

In this section, the present model is validated by the recent experimental results of the strength distributions of uniaxial tensile poly-Si specimens of two gauge lengths: $L = 20$ μm and $L = 70$ μm.[60, 85]. All the specimens have a nominal width of 2 μm, which is much grater than the typical depth of a surface groove. As a result, the failure statistics of the two side-walls can be regarded as indepenent. In the test, specimens of 20 μm gauge length were tested by a slack-chain tester, which allows simultaneous testing of a large number of specimens [85]. Specimens of 70 μm gauge length were tested by using an on-chip tester with a chevron thermal actuator. The details of these two experimental set-ups were described in [60, 85].

In order to use the present model to analyze these experiments, the statistical properties of the field $Z(x)$ is first extracted from the stochastic finite element simulation. The stochastic finite element simulation involves a finite element model of a uniaxial tensile specimen of a length of 1 mm under a unit far-field stress ($\sigma_N = 1$), in which one side-wall contains a series of randomly distributed surface grooves. In the present analysis, the poly- Si material is modeled as an isotropic elastic material with a Young modulus $E = 156$ GPa and a Poisson ratio $\mu = 0.22$, and the side-wall grooves are modeled as V-notches. Based on the reported measurements [85], the random side-wall geometry is characterized by the following three random variables: (1) the notch opening angle θ is assumed to obey a uniform distribution from 20° to 140°; (2) the notch depth a follows a Weibull type distribution with an upper bound of 62 nm; and (3) the spacing s of V-notches obeys a uniform distribution bounded between 50 nm and 750 nm, i.e.:

$$F_\theta(\theta) = \frac{\theta - 20}{120} \qquad (20 \leq \theta \leq 140) \tag{2.34}$$

$$F_a(a) = \exp\left[-\left(\frac{62-a}{28}\right)^{6.5}\right] \qquad (0 \le a \le 62) \tag{2.35}$$

$$F_s(s) = \frac{s-50}{700} \qquad (50 \le s \le 750) \tag{2.36}$$

where $F_\theta(\theta)$, $F_a(a)$ and $F_s(s)$ denote the CDFs of θ, a, and s, respectively. In principle, $F_a(a)$ allows negative values of a, which is physically inadmissible. However, it is noted that the probability of sampling the negative value of a is extremely small, i.e. $F_a(0) = 6.7 \times 10^{-77}$. The simulated elastic stress field is then used to compute the random field $Z(x)$ by using Eqs. (2.4) and (2.5). In the computation, l_x and l_y in Eqs. (2.4) and (2.5) were chosen to be 5 nm for both, which is approximately on the order of the fracture process zone size of poly-Si [103, 85, 65]. It should be pointed out that different choices of l_x and l_y would lead to different model parameters for optimum fitting of the experimental data. However, the general behavior of the present model would not be affected. As will be shown later, the current choice of l_x and l_y yields a reasonable value of the mean material strength.

We first examine the stationarity of the random field $Z(x)$ by checking its ergodicity through Eq. (2.8). Figure 2.5 (a) shows that the value of $\Psi(\epsilon)$ of Eq. (2.8) is approximately equal to zero, which demonstrates the stationarity of $Z(x)$. Based on the simulated random field of $Z(x)$, the marginal CDF and the correlation function of $Z(x)$ can be determined, shown in Figure 2.5 (b) and (c).

Compared to the dimensionless stress field $Z(x)$, the generation of the strength field $f_t(x)$ is relatively straightforward. The marginal CDF of $f_t(x)$ is considered to be the Gauss-Weibull grafted CDF described by Eqs. (1.24a) and (1.24b). The correlation function of $f_t(x)$ is considered to be a Gaussian function: $\rho_{f_t}(\Delta x) = \exp[-(\Delta x/l_a^2)]$, where l_a = a length constant. Therefore, the covariance function is $R_{f_t}(\Delta x) = \delta_{f_t}^2 \exp[-(\Delta x/l_a^2)]$, where δ_{f_t} is the standard deviation of $f_t(x)$. We choose $l_a = 20$ nm, which is on the order of the size of a typical crystal grain of

poly-Si structures. The generation of the random strength field $f_t(x)$ involves two steps: (1) generate the standard Gaussian process $Y(x)$ with a given correlation function $\rho_Y(\Delta x)$; and (2) translate the standard Gaussian field $Y(x)$ into the targeted field $f_t(x)$, i.e. $f_t(x) = F_{f_t}^{-1}\{\Phi[Y(x)]\}$. The correlation function of $Y(x)$ can be numerically determined from the covariance function $R_{f_t}(\Delta x)$ through

$$R_{f_t}(\Delta x) = \int_{-\infty}^{+\infty}\int_{-\infty}^{+\infty} F_{f_t}^{-1}\left[\Phi\left(y_1\right)\right] F_{f_t}^{-1}\left[\Phi\left(y_2\right)\right] \phi[y_1, y_2, \rho_y(\Delta x)]\mathrm{d}y_1\mathrm{d}y_2 \qquad (2.37)$$

where ϕ is the bivariate Gaussian PDF. From Figure 2.6, it is seen that the $\rho_{f_t}(\Delta x)$ and $\rho_y(\Delta x)$ are very close to each other, which implies that the Weibull tail of the original strength distribution has a minimal effect on the autocorrelated feature of the transformed Gaussian field.

After the random field $Z(x)$ and $f_t(x)$ are generated, the generalizations of the field $\eta_0(x)$ and the corresponding crossing barrier λ can be obtained by the use of Eqs. (2.10) and (2.11). By using Eqs. (2.22) to (2.26), the crossing rate μ_λ can be estimated. Finally, the structural strength distribution $F_{\sigma_N}(\sigma_N, L)$ is obtained by using Eqs. (2.3) and (2.21).

The aforementioned procedure is used to perform optimum fitting of the measured strength distributions of poly-Si tensile specimens with gauge lengths $L = 20\ \mu m$ and $L = 70\ \mu m$. Figure 2.7 shows that the model predictions on the structural strength distribution well match the experimental strength distributions of MEMS specimens of different sizes, and the corresponding fitted parameters for specimens of both gauge lengths are $\mu_G = 19$ GPa, $\delta_G = 2.85$ GPa, $P_{gr} = 0.095$, $m_W = 64$, $s_W = 15.6$ GPa, and $r_f = 1.05$. It should be pointed out that the calibrated mean strength is close to the theoretical strength of silicon predicted by ab initio simulations [39].

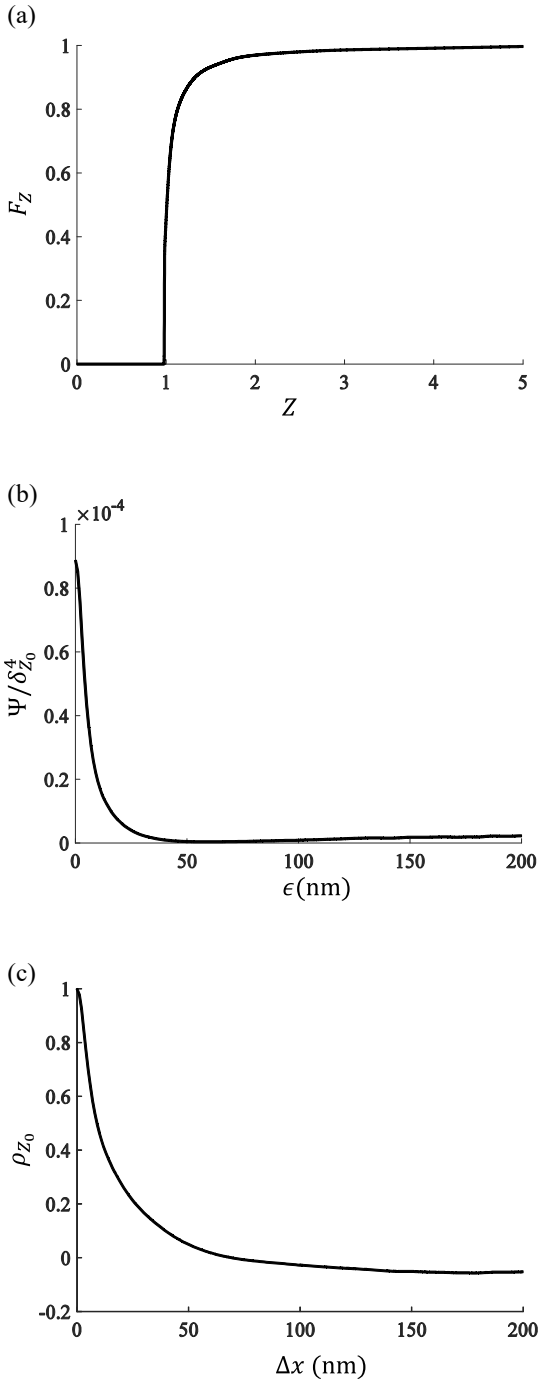

Figure 2.5: (a) marginal CDF of $Z(x)$, (b) ergodicity check of the zero-mean field $Z_0(x)$ (δ_{Z_0} = standard deviation of Z_0), (c) correlation function of $Z_0(x)$.

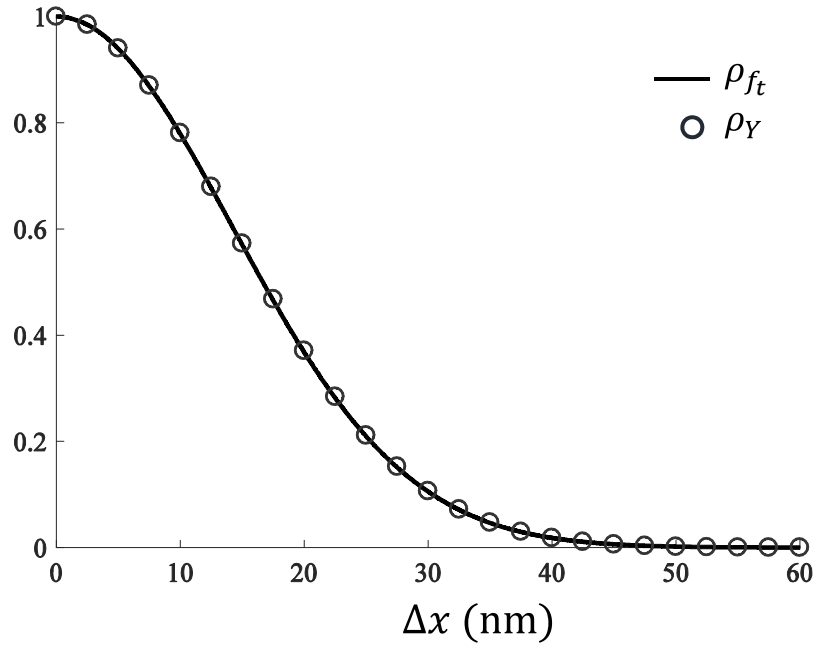

Figure 2.6: Comparison of the correlation functions of the random field $f_t(x)$ and its translated standard Gaussian field.

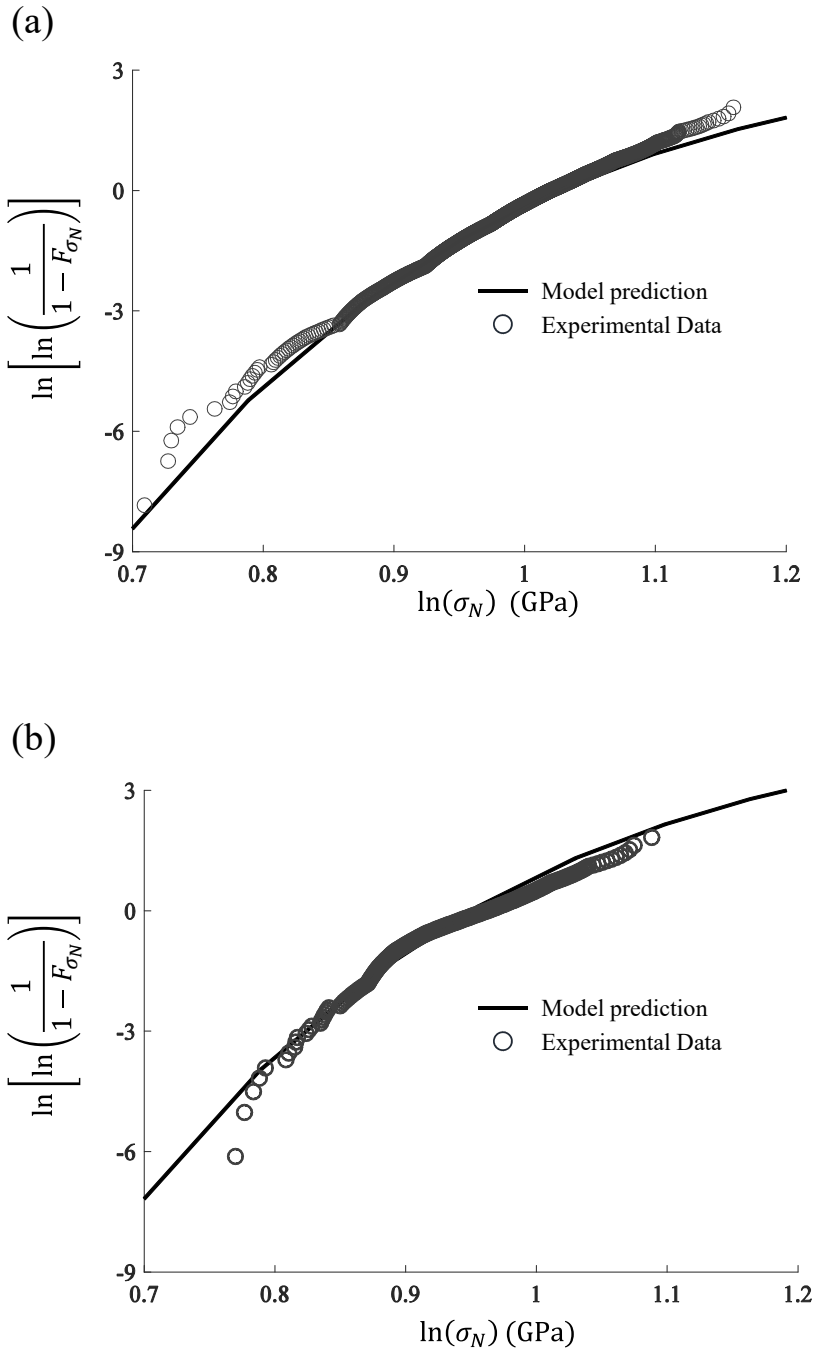

Figure 2.7: Optimum fittings of the measured strength histograms of poly-Si tensile specimens by the present model:(a) $L = 20$ μm, (b) $L = 70$ μm.

2.4 Analysis of strength distribution of flexural specimens

The model formulation for flexural loading configurations presented in Section 2.2 is applied to predict the strength distribution of poly-Si MEMS beams under three-point-bending. The calculation uses the calibrated model parameters presented in Section 2.3. Four different sizes of geometrically similar beams are studied, i.e. span-to-depth ratio $L/D = 4$ and $L = 10$, 20, 40, 80 μm. The structural strength of the beam is defined by $\sigma_N = P_{\max}/(bD)$.

To use the simplified formulation presented in Section 2.3, we first check whether the field $Z(x)$ can be approximated by a uniformly modulated field. For each beam size, a total of 200 stochastic finite element samples were generated in order to extract the statistical properties of $Z(x)$, where the side-wall geometry is also described by the aforementioned three random variables (Eqs. (2.34)-(2.36)). Firstly, the spatially varying mean $\mu_Z(x/L)$ (normalized by L) is obtained by averaging all the generated fields. The stationary random component $Z_0(x)$ is then obtained by Eq.(2.27). Figure 2.8 (a) shows the extracted spatially varying mean $\mu_Z(x/L)$ of these four sizes, and it is seen that they are very close to each other. Likewise, it is found that the corresponding zero-mean stationary components $Z_0(x)$ for these specimens could be described by a single random field. The stationarity of $Z_0(x)$ is examined by calculating its covariance function along the specimen length. As a demonstration, Figure 2.8 (b) shows that the covariance function of the simulated $Z_0(x)$ for which $L = 10$ μm. It is seen, for each distance gap Δx, the value of the spatially varying covariance function fluctuates around a constant value regardless of Δx. Furthermore, Figure 2.8 (c) shows the ergodicity check of $Z_0(x)$ by using Eq. (2.8). As a result, from Figure 2.8 (b) and (c), it is demonstrated that $Z_0(x)$ can be considered as a stationary field.

By using Eqs. (2.27) to (2.33), the strength distributions of these beams were

finally obtained. It should be noted that there is only one side-wall would fail in the present case, so that the strength distribution F_{σ_N} is just the $F(\sigma_N, L)$ in Eq. (2.29). As shown in Figure 2.9, it is seen that, similar to the case of uniaxial tensile specimens, there exists a size effect on the strength CDF, in which all the simulated strength CDFs contain a power-law tail with the same Weibull modulus. The portion this power-law tail increases as specimen size increases, and eventually it is expected that the entire strength CDF would follow the Weibull distribution. So far, the experimental data on strength distribution of poly-Si MEMS beams under three-point-bending is not available. Therefore, in order to validate the present model for this loading case, we compare the strength distribution of specimens of $L = 10$ μm predicted by the present model with the corresponding Monte Carlo simulations. Figure 2.10 shows that the model prediction agrees well with the simulation result.

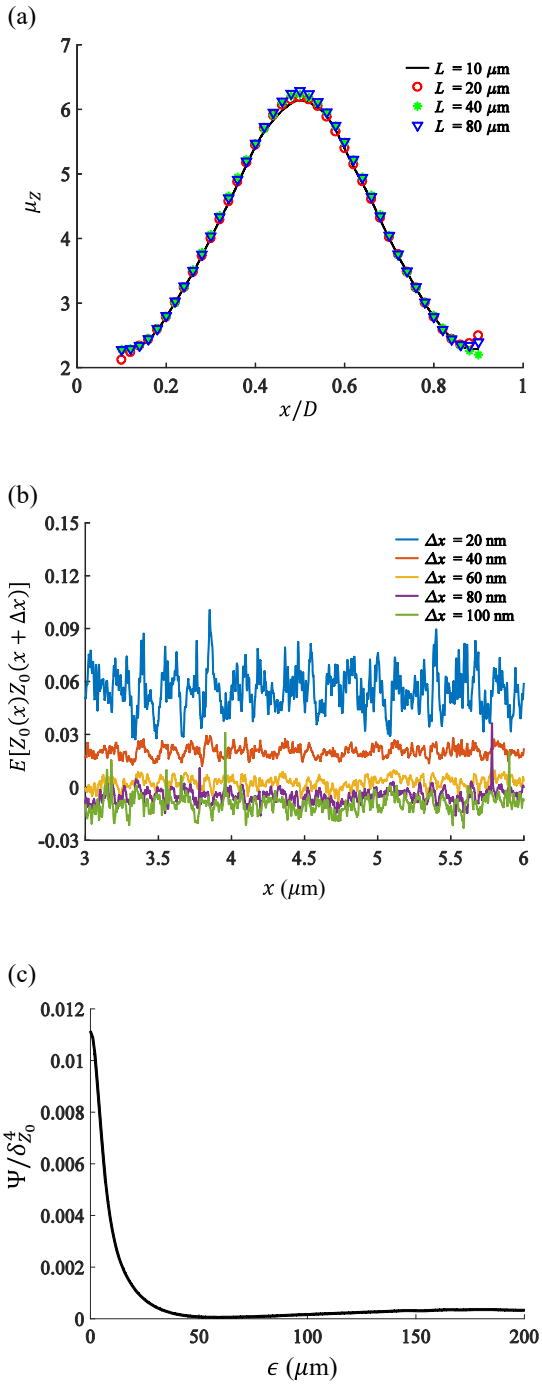

Figure 2.8: Statistical properties of the uniformly modulated random field $Z(x)$ for the random stress field of the three-point-bending beams: (a) spatially varying mean of $Z(x)$ for different specimen sizes, (b) covariance function of the zero-mean stationary field $Z_0(x)$ for specimen size $L = 10$ μm, (c) ergodicity check of $Z_0(x)$ for specimen size $L = 10$ μm (δ_{Z_0} = standard deviation of $Z_0(x)$).

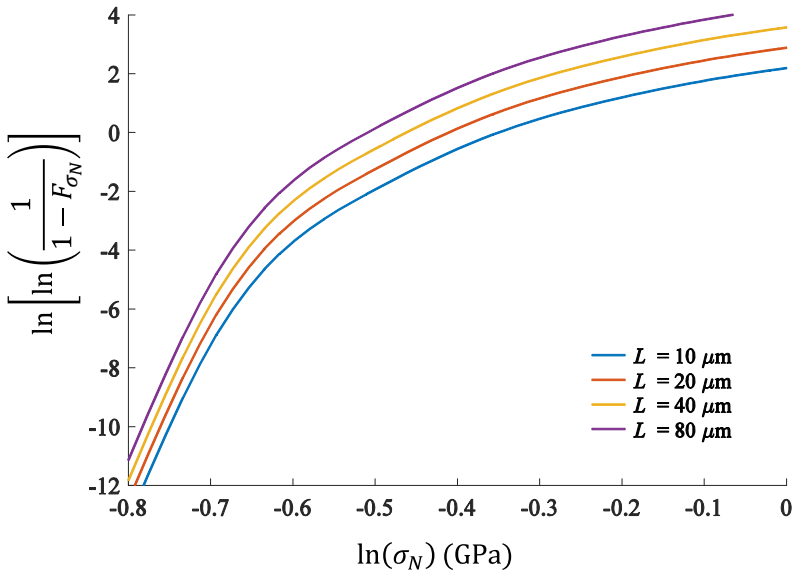

Figure 2.9: Predicted strength distributions of geometrically similar poly-Si beams of four different sizes.

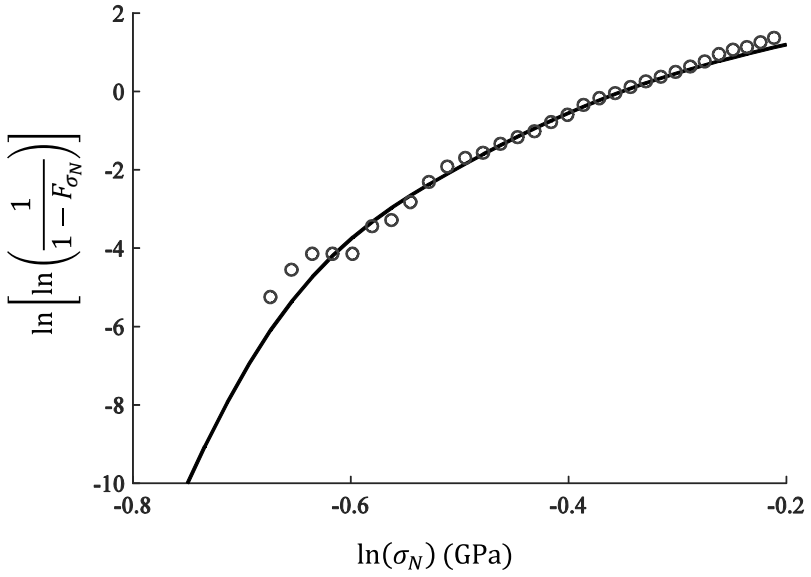

Figure 2.10: Comparison of the strength distributions of the beams of $L = 10$ μm predicted by the present model and by the Monte Carlo simulations.

2.5 Size effect analysis

Based on the foregoing analysis, it is evident that the structural strength distribution always exhibit a strong size effect. The understanding of the scaling law of structural strength statistics is crucial for reliability-based design of engineering structures. In this section, we discuss the asymptotic behaviors of the strength distribution as well as the mean structural strength by using the aforementioned uniaxial tensile specimen as an example. It should be pointed out that similar approaches can also be apply to study the size effect of cases of other loading configurations.

2.5.1 Size effect on the structural strength distribution

Figure 2.11 plots the calculated strength CDFs of uniaxial tensile poly-Si specimens of different lengths L in the Weibull scale. It is seen that, when L is small, the left tail of the distribution follows a Weibull CDF (which is menifested by a straight line on the Weibull scale) and its bulk part deviates from the Weibull CDF significantly. For a large L, the entire strength CDF approaches the Weibull CDF. Based on the extreme value theory, the strength distribution of the entire specimen is governed by its left tail as the specimen size becomes large[49, 59, 95, 34]. Therefore, it is crucial to explore the left tail behavior of the structural strength distribution.

We first analyze the asymptotic behavior of the $F_{\eta_0}(\lambda)$ for small stresses. Note that $F_{\eta_0}(\lambda) = 1 - \Pr.(\sigma_N Z \geq f_t) = \Pr.(\sigma_N \leq f_t/Z)$. Instead of using Eq. (2.12), it is easier to use the ratio of f_t and Z to compute this failure probability:

$$F_{\eta_0}(\lambda) = \Pr.(\sigma_N \leq f_t/Z) = 1 - \int_0^\infty F_{f_t}(\eta\sigma_N) f_Z(\eta) \mathrm{d}\eta \tag{2.38}$$

From Eq. (1.24a), it is obvious that the left-tail of $F_{f_t}(\sigma)$ is a power law. Since the random variable Z is essentially bounded ($Z \in [1, z_{max}]$), for a small value of σ_N (i.e.

$\sigma_N \leq x_{gr}/z_{max}$), Eq. (2.38) can be rewritten as

$$F_{\eta_0}(\lambda) = 1 - \left(\frac{\sigma_N}{s_1}\right)^m \tag{2.39}$$

where $s_1 = s_0[\int_0^\infty \eta^m f_z(\eta)\mathrm{d}\eta]^{-1/m}$. Therefore, $F_{\eta_0}(\lambda)$ must have a power-law tail with respect to σ_N.

Since a small applied stress implies a high crossing barrier λ and therefore a low crossing rate μ_λ, based on Eqs. (2.21), (2.24) and (2.39), the strength CDF of the entire specimen for small stresses can be rewritten as

$$F_{\sigma_N}(\sigma_N) \approx \left(\frac{\sigma_N}{s_1}\right)^m + \frac{\delta_{\dot{Y}}}{\sqrt{2\pi}}\phi\left[\lambda_Y(\sigma_N)\right] L \tag{2.40}$$

As discussed in Section 2.2, since the crossing rate μ_λ is calculated from the translated standard Gaussian field $Y(x)$ (Eq. (2.22)). It is easy to show that

$$\phi\left[\lambda_Y(\sigma_N)\right] = \frac{1}{\sqrt{2\pi}} \exp\left\{-\frac{1}{2}\left\{\Phi^{-1}\left[1-(\sigma_N/s_0)^m\right]\right\}^2\right\} \tag{2.41}$$

The computation of $\delta_{\dot{Y}}$ involves the evaluation of the power spectrum density of $Y(x)$, and an analytical form of $\delta_{\dot{Y}}$ as a function of σ_N is not possible. Instead, we evaluate the dependence of $\delta_{\dot{Y}}\phi\left[\lambda_Y(\sigma_N)\right]$ on σ_N numerically. As shown in Figure 2.12. it is found that this dependence follows a power-law, where the power-law exponent is close to m_W, i.e. $\delta_{\dot{Y}}\phi\left[\lambda_Y(\sigma_N)\right] \propto \sigma_N^m$. Together with Eq. (2.40), we conclude that

$$F_{\sigma_N}(\sigma_N) \propto \sigma_N^m \qquad (\sigma_N \to 0) \tag{2.42}$$

Expression (2.42) implies that the MEMS structures always exhibit a power-law behavior for the left tall of the strength distributions, regardless of the size of the structures. It should be pointed out that, in the foregoing analysis, we did not im-

pose any restriction on the marginal distribution of the stress field, which suggests the power-law tail of structural strength distribution stems from the left power-law tail of the marginal distribution of the strength field. The stress field can influence the magnitude of the parameters of this power-law tail, but it does not dictate the power-law functional form of the left tail of structural strength distribution, which will be discussed in detail in Chapter 4.

For large-size specimens, there are a vast number of potential failure locations, in which the failure statistics of adjacent locations are correlated. However, we can group these failure locations in a way that the failure statistics of each group becomes independent. The length of a group of failure locations is L_0. Based on the foregoing analysis, it is clear that the CDF of the strength of each group would have a power-law tail. At the large size limit (i.e. $L \to \infty$), the total number of groups approaches infinity. According to the extreme value theory [49, 59], since the CDF of the strength of each group is a power-law function, the strength distribution of the entire specimen must follow the Weibull distribution, i.e.:

$$F(\sigma_N, L) = 1 - \exp[-(\sigma_N/s_w)^m] \tag{2.43}$$

where $s_w = s_{w0}(L_0/L)^{1/m}$ = Weibull scaling parameter, and s_{0w} = constant.

On the other hand, at the small-size limit (i.e. $L \to 0$), the strength distribution of the specimen will be governed by the marginal of η_0, i.e. $F(\sigma_N, L) \approx 1 - F_{\eta_0}(\lambda)$. Figure 2.13 plots $F(\sigma_N, L)$ at $L \to 0$ on a Gaussian distribution paper. It can be seen that the distribution follows a straight line when the probability is greater than 0.1, which implies the bulk part of the distribution is a Gaussian distribution. However, the transitional regime from the Weibull tail to the bulk Gaussian part is pretty wide, whose functional form remains unclear.

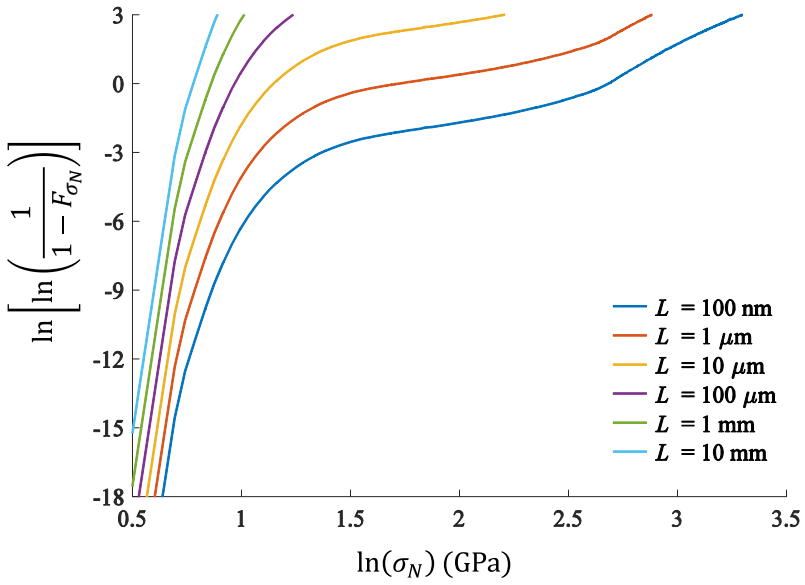

Figure 2.11: Size effect on the strength distribution of poly-Si MEMS specimens under uniaxial tension.

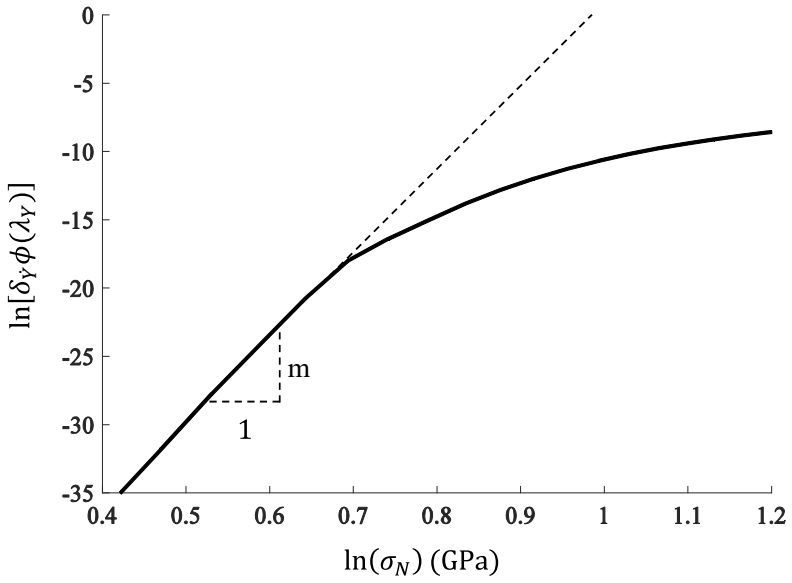

Figure 2.12: Numerically simulated relation between $\ln[\delta_{\dot{Y}}\phi(\lambda_Y)]$ and σ_N.

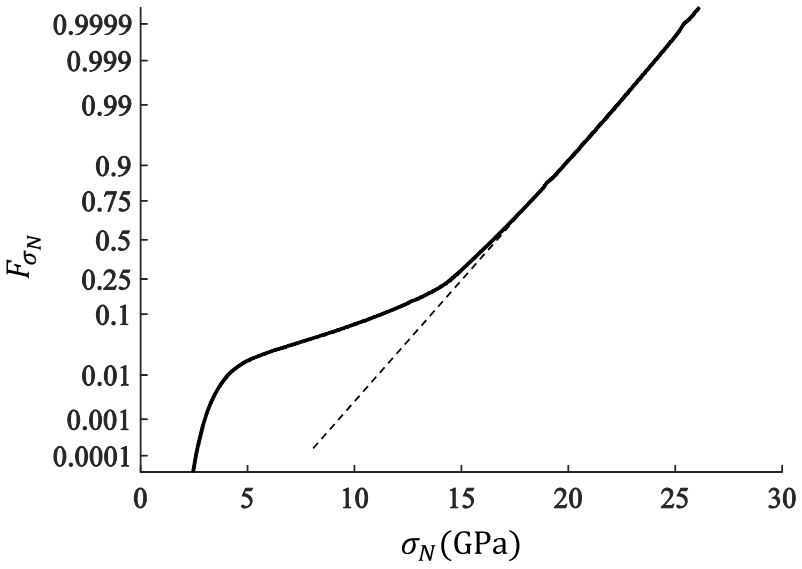

Figure 2.13: Probability distribution of $F_{\sigma_N}(\sigma_N)(L \to 0)$ plotted in the Gaussian distribution paper.

2.5.2 Size effect on the mean structural strength

The size-dependence of structural strength distribution directly yields the size effect on the mean structural strength. Similar to the foregoing analysis, we use the uniaxial tensile specimens as an example to illustrate the size effect on the mean structural strength. Meanwhile, similar analyses can be applied to other loading configurations.

The mean structural strength, represented by $\bar{\sigma}_N$, was calculated from Eq. (1.15), which is a function of the structural size L (shown in Figure 2.14). Note that the small size limit(i.e. $L \to 0$) in Figure 2.14 is merely a mathematical abstraction because it lose its physical meaningful if the length is smaller the size a side-wall groove, which is around 70 nm. Nevertheless, the plot of the entire size effect curve of structural strength provides a comprehensive understanding of the behavior of this model. As it can be seen in Figure 2.14, the size effect curve of the mean structural strength approaches a horizontal small-size asymptote. Such an asymptote stems from the correlated feature of the random field $\eta_0(x)$. The mean autocorrelation length of $\eta_0(x)$ for the small-size limit can be calculated as

$$L_a = \mathrm{E}\left[L_{\eta_0}(\sigma_N)\right] = \int_0^\infty L_{\eta_0}(\sigma_N) f(\sigma_N, L) \mathrm{d}\sigma_N \tag{2.44}$$

where $L_{\eta_0}(\sigma_N)$ = defined autocorrelation length of $\eta_0(x)$ for a given value of σ_N, and $f(\sigma_N, L) = \mathrm{d}F(\sigma_N, L)/\mathrm{d}\sigma_N$. For specimens of lengths smaller than a characteristic size of $L_p = C_1 L_a$ (C_1 = constant), the failure statistics of the each individual point becomes correlated, and therefore the mean structural strength would approach a constant value, which is signified by this horizontal asymptote. L_p represents an intrinsic characteristic length scale of the random field that governs the material failure statistics. As will be discussed in Section 2.6, this length scale L_p provides a link between the present model and the conventional weakest-link model. Furthermore, the present model also predicts the first order derivative of the size effect curve of the

mean structural strength at the small size limit, i.e.:

$$\bar{\sigma}_N \approx \int_0^\infty F_{\eta_0}(\lambda)\left[1-\frac{\mu_\lambda}{F_{\eta_0}(\lambda)}L\right]\mathrm{d}\sigma_N = \sigma_0 - C_2 L \quad (L\to 0) \tag{2.45}$$

where $\sigma_0 = \int_0^\infty F_{\eta_0}(\lambda)\mathrm{d}\sigma_N$ = mean strength at $L=0$, and C_2 = constant. It is noted that this linear decay from the small-size strength limit is in consistence with the prediction of the cohesive crack model [15].

Since the strength distribution would approach to the Weibull distribution at the large-size limit (Eq. (2.43)), the corresponding mean structural strength can be calculated by the Weibull mean, i.e.:

$$\bar{\sigma}_N = s_{0w}\Gamma\left(1+\frac{1}{m}\right)\left(\frac{L_p}{L}\right)^{1/m} \tag{2.46}$$

where $\Gamma(x)$ = the Eulerian gamma function. Consider that the power-law tail of a specimen of length L_p reaches a probability of P_{t0}. The size of the specimen, whose strength distribution would follow the Weibull CDF up to a probability of P_{fw} for which the Weibull size asymptote is approached, should be at least on the order of $L_w = L_p \ln(1-P_{fw})/P_{t0}$.

At the intermediate size range, there may exist another power-law asymptote if L_p and L_w are far apart. Such an asymptote is sometimes referred to as the intermediate asymptote [11], which could be described by $\bar{\sigma}_N \propto L^{-1/r}$ ($L_p \ll L \ll L_w$). This power-law exponent is governed by the statistical properties of the random field $\eta_0(x)$.

To asymptotically match the aforementioned three asymptotes, the following approximate equation is proposed to describe the size effect curve of the mean structural strength for the entire size range[13, 14]:

$$\bar{\sigma}_N = \sigma_0\left[\left(\frac{L_p}{L+L_1}\right)^u + \left(\frac{L_2}{L+L_1}\right)^{r/m}\right]^{1/r} \tag{2.47}$$

where L_p, L_1, L_2, u, r = constants. Note that Eq. (2.47) consists of three power-law asymptotic behaviors: (1) at the small size limit, $\bar{\sigma}_N \to \sigma_0$, (2) at the intermediate size range, $\bar{\sigma}_N \propto L^{-1/q}$ ($q = r/u$), and (3) at the large size limit, $\bar{\sigma}_N \propto L^{-1/m}$. Figure 2.14 shows that Eq. (2.47) agrees well with the simulated size effect curve of the mean structural strength of the MEMS specimens under uniaxial tension.

It should be pointed out that, in the existing literature of quasi-brittle fracture, the size effect of this kind was usually regarded as energetic-statistical in nature [14, 15, 23]. The conventional weakest-link model is unable to yield the horizontal small-size asymptote since the specimen size cannot be smaller than the size of the material element in the model. The horizontal small-size asymptote needs to be separately derived from the cohesive crack model, which is a deterministic approach. This asymptotic behavior is then superimposed onto the statistical size effect predicted by the weakest-link model, which leads to an energetic-statistical scaling law [14, 15]. In contrast to the aforementioned viewpoint, this study shows that the entire size effect curve of the mean structural strength can be described by a purely probabilistic description via the present model.

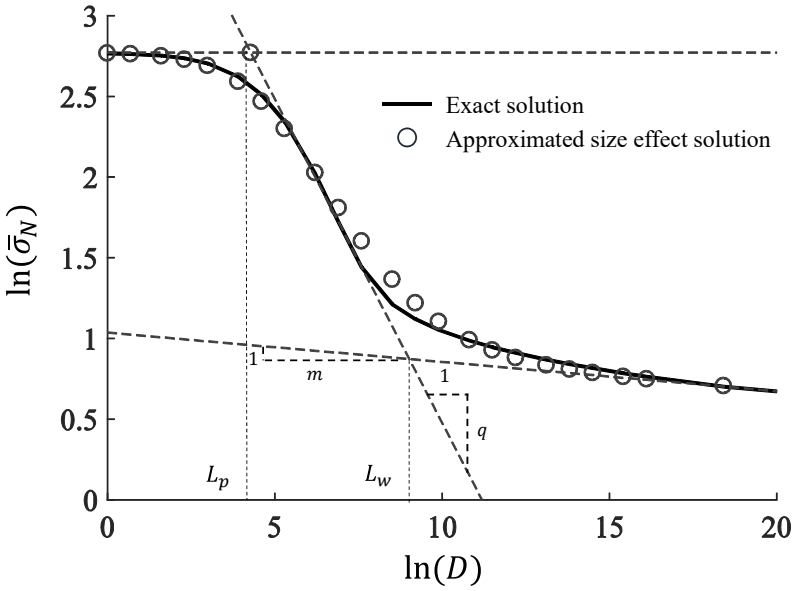

Figure 2.14: Size effect curve of the mean structural strength of uniaxial tensile poly-Si MEMS specimens.

2.6 Relation with the conventional weakest-link model

Since the conventional weakest-link model is the most widely used model for the strength statistics of brittle and quasi-brittle structures, it is worthwhile to compare the present model with the conventional weakest-link model. As discussed in Sections 1.2 and 1.3, the conventional weakest-link models is essentially a discrete model, which is a statistical chain of material elements. By contrast, the present model is anchored by a continuous description, which contains a length scale that describes the spatially autocorrelated features of the failure statistics of the correlated material points.

Consider a side-wall of a uniaxial tensile specimen. The essence of Eq. (2.21) is a pre-factor representing the reliability of the starting point, plus a Poisson process. Meanwhile, the Poisson process is the analytic prolongation of the weakest-link model. Hence, Eq. (2.21) can be rewritten as Eq. (2.48). The model represented by Eq. (2.48) can be statistically equivalent to a chain shown in Figure 2.15 (a), in which the first element represents the reliability of the starting point, and each of the rest element represents the reliability of a domain whose size is L_0. On the other hand, in the spirit of the finite weakest-link model, the overall strength distribution of one side-wall can be re-written as (2.49), i.e.:

$$\begin{aligned} F(\sigma_N, L) &= 1 - F_{\eta_0}(\lambda)\left[\exp\left(-\frac{\mu_\lambda L_0}{F_{\eta_0}(\lambda)}\right)\right]^{\frac{L}{L_0}} && (2.48) \\ &= 1 - \left[1 - F_1(\sigma_N)\right]^n && (2.49) \end{aligned}$$

where $n = L/L_0$, and

$$F_1(\sigma_N) = 1 - \{F_{\eta_0}(\lambda)\}^{1/n} \exp\left[-\frac{\mu_\lambda L_0}{F_{\eta_0}(\lambda)}\right] \tag{2.50}$$

Based on Eqs. (2.48) and (2.49), it is clear that the present model can be translated to a weakest-link model. Despite that Eq. (2.49) does not pose any restriction on

length L_0, from a physical viewpoint, L_0 should be larger than the length scale L_p extracted from the characteristic autocorrelation length of the random field $\eta_0(x)$. It should be pointed out that $F_1(\sigma_N)$ in Eq. (2.50) is not exactly equal to the failure probability of specimen of length L_0, which can be written as

$$F_{L_0}(\sigma_N) = 1 - F_{\eta_0}(\lambda) \exp\left[-\frac{\mu_\lambda L_0}{F_{\eta_0}(\lambda)}\right] \tag{2.51}$$

The difference between Eq. (2.50) and (2.51) lies in the prefactor of the exponential term, which accounts the probability of crossing over of the starting point [94, 95]. To make the model match the weakest-link model, as shown in Figure 2.15 (b), we can distribute the reliability of the starting point evenly into n elements.

Based on the aforementioned discussion, it is clear that the present model is a natural generalization of the conventional weakest-link model by incorporating the spatially correlated statistical information of each point. By contrast, the conventional weakest-link model assigns one probability distribution function to each element, without considering the statistically correlated features inside the material element. Furthermore, the present analysis also indicates that the material element size of the finite weakest-link model is related to the autocorrelation length of the random field that governs the material failure.

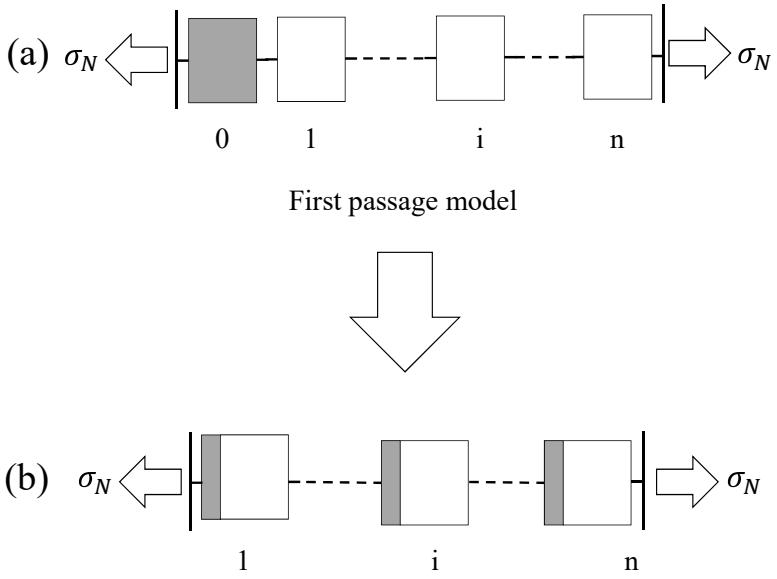

Figure 2.15: Relation between the first-passage model and the finite weakest-link model of structural strength statistics.

2.7 Conclusions

In this chapter, a first-passage based model is developed for the strength statistics of poly-Si MEMS structures, which is able to realistically incorporate the detailed statistical information of random applied stress and the random material strength. Depending on the specimen geometry and loading configuration, the failure statistics can be modeled by either a stationary or a non-stationary random field, and the overall structural failure risk can be evaluated by a first-passage analysis. The model is verified by optimum fitting of the measured strength distributions of poly-Si MEMS specimens of two gauge lengths as well as Monte Carlo simulations.

It is shown that the present model naturally involves an essential length scale, which is related to the autocorrelation length of the random field governing the material failure. The functional behavior of the strength distribution is strongly dependent on the ratio of specimen size to this length scale. For small-size specimens, the strength CDF is highly non-Weibullian except for its left tail. For large-size specimens, the strength distribution follows the classical Weibull distribution, which is consistent with the extreme value theory.

It is noted that the distribution of the structural strength always contains a power-law tail regardless of the overall structural size. This power-law tail behavior of structural strength distribution stems from the left power-law tail of the distribution of material strength. The random stress field will influence the parameters of this power-law tail. However, the power-law form of the strength distribution is not affected by the distribution of the applied stress.

The size-dependence of structural strength distribution further leads to a strong size effect on the mean structural strength. Due to the consideration of the autocorrelated features of the non-local stress field and the strength field, the model is able to yield a horizontal small-size asymptote of the size effect curve of the mean structural

strength. At the large-size limit, the model predicts the classical Weibull size effect. This result indicates that the entire size effect on the mean structural strength of this kind can be explained from a purely statistical viewpoint.

It is demonstrated that the present model can be translated into the finite weakest-link model. Compared to the finite weakest-link model, the present model contains much richer information of the statistics of each point. Meanwhile, the model also indicates that the RVE size of the conventional weakest-link model is directly related to the autocorrelation length of random field that governs the material failure.

Chapter 3

A Renewal Weakest-Link Model for the Strength Distribution of Poly-Silicon MEMS Structures

3.1 Introduction

In Chapter 2, we discussed a first-passage model for strength distribution of poly-Si MEMS structures [101]. The model explicitly includes the autocorrelated random fields of the applied stress and the material strength. The failure probability of the structure is calculated as the first-passage probability of the random field governing the material failure with respect to a crossing barrier. Though the first-passage model provides a physical representation of the failure strength statistics of poly-Si MEMS structures, the computational cost is much higher than that of the conventional weakest-link model. Meanwhile, some detailed statistical information, such as the covariance functions of the random strength field and the random stress field, may not be easily obtained. On the other hand, the finite weakest-link model is easy to compute but involves some simplifications. The main simplification is that it assumes that the spacing of V-notches is a constant.

For practical engineering purposes, an ideal model should have a reasonable bal-

ance between accuracy and simplicity. In this chapter, we present a probabilistic model by combining the finite weakest-link model with the renewal theory. The model removes the limitation on material element size of the weakest-link model in order to better capture the random geometry of the side-walls, meanwhile it preserves a desirable computational efficiency. The new model is referred to as the renewal weakest-link model.

This chapter is organized in the following manner: Section 3.2 present the formulation of the renewal weakest-link model; Section 3.3 studies the behavior in terms of structural strength distribution of present model at large size limit; In Section 3.4, the proposed model is validated through the comparison with the experimentally measured strength distributions of uniaxial tensile poly-Si MEMS specimens; Section 3.5 proposed a simplified calculation approach, which considerably decreases the computational cost while preserves a reasonable accuracy .

3.2 Model formulation

Here we limit our attention to uniaxial tensile specimens under controlled load test. Similar to Section 2, the randomly distributed side-wall grooves are modeled as some V-notches with random depths, random opening angles and random spacings.

Consider a tensile MEMS specimen of length L subjected to remote stress σ_N (shown in Figure 3.1 (a)). As shown in Figure 3.1 (b)-(c), the side-wall of the specimen can be divided into a group of segments, where each segment contains exactly one V-notch in the middle, and the segment length, the depth and the opening angle of the V-notch are three random variables. Let N be the total number of V-notches along one side-wall, and l_i to be the length of ith segment. Obviously, since l_i is a random variable, for a given side-wall of length L, the V-notch number N is also a random variable. By further assuming the failure statistics of each segment is statistically

independent, the survival probability, or reliability, of the side-wall subject to the remote stress σ_N can be calculated as

$$R_s(\sigma_N, L) = \prod_{i=1}^{N} R_e(\sigma_N, l_i) \tag{3.1}$$

where R_e is the reliability function of the segments. The reliability function $R_e(\sigma_N, l_i)$ measures the survival probability of a segment with a given length l_i under the nominal stress σ_N, which is a deterministic function of σ_N and l_i. It should be pointed out that R_s is random since each l_i is random.

In order to analytically calculate of Eq. (3.1), the following formulation based on the renewal theory is applied (shown in Figure 3.1 (d)). The present formulation considers the side-wall consists of $N + 1$ segments, in which the first N segments contain V-notches and the last segment does not. The last segment without a V-notch is referred to as the vacancy by the study of this chapter. Based on the foregoing discussion, it is considered that only segments with V-notches would contribute to the failure statistics of the specimen. The total length of $N + 1$ segments would be larger than the actual side-wall length L. However, this is unimportant since what matters for the failure statistics of the specimen is the first N number of segments with V-notches, whose total length is less than L. If the side-wall of length L consists of exactly n number of V-notches, we must have

$$\sum_{i=1}^{n} l_i \leq L \quad \text{and} \quad \sum_{i=1}^{n+1} l_i > L \tag{3.2}$$

At this point, it should be clarified that N denotes the total V-notch number for a given side-wall, which is a random variable. While n is a deterministic number representing the given side-wall contains exactly n V-notches, which represents the case that the random variable N is equal to the deterministic number n.

First of all, we study the distribution of N for a given side-wall of length L, represented by $P_N(n, L)$, which is probability that a side-wall of length L contains exactly $n+1$ segments and the $n+1$th segment is a vacancy. Such a probability can be computed by adopting the renewal process as shown in Figure 3.2 (a). A renewal process is a counting process that counts the total number of random events happened in a given domain, while the occurrence of each random events is independent and the spacing between any consecutive two events obeys the same distribution. As a result, in the renewal process constructed in Figure 3.2 (a), the ith random event is just the ending point of ith segment. The recordset $N(L)$, which counts the total number of events that happened in the domain $[0, L]$, is the renewal process that we need, which is also a 1-dimensional discrete random field. As shown in Figure 3.2 (a), the probability that $N(L) = n$ equals the probability that the ending point of the renewal process $N(L)$ is located between nth event and $n+1$th event, which can be further interpreted as the probability that $\Pr.[\sum_{i=0}^{n} l_i < L \cap \sum_{i=0}^{n+1} l_i > L]$. Finally, the distribution of $N(L)$ is obtained as the following equation, i.e.:

$$
\begin{aligned}
P_N(n, L) =& \Pr.[N(L) = n] \\
&= \Pr.[\sum_{i=0}^{n} l_i < L \cap \sum_{i=0}^{n+1} l_i > L] \\
&= \Pr.[\forall l_{n+1}, \sum_{i=0}^{n} l_i < L] - \Pr.[\sum_{i=0}^{n+1} l_i < L] \\
&= F_{L_n}(L) - F_{L_{n+1}}(L) \\
&= \int_0^L \int_0^{L-l_1} \cdots \int_0^{L-l_1-l_2\cdots-l_{n-1}} \prod_{i=1}^{n} f_l(l_i) \left[1 - F_l(L - l_1 - l_2 \cdots - l_n)\right] \cdot \\
&\cdot \mathrm{d}l_n \mathrm{d}l_{n-1} \cdots \mathrm{d}l_1
\end{aligned}
\tag{3.3}
$$

where f_l and F_l are the PDF and the CDF of the segment length, F_{L_i} is the CDF of $L_i = \sum_{j=0}^{i} l_j$. Eq. (3.3) is the distribution of a renewal process [6]. It should be pointed out that all the segment lengths (including the vacancy) are assumed to obey the same distribution. Besides, since P_N is the distribution of N, $\sum_{n=0}^{\infty} P_N(n, L) = 1$.

Now let us study the probability of having such a side-wall of length L, in which the total number of V-notches is exactly n, and it is able to survive the nominal stress σ_N. Such a probability is represented by $R_s(\sigma_N, L, n)$. We can further assign each segment of the aforementioned renewal process a reliability function, and this new model formulation is called the renewal weakest-link model (shown in Figure 3.2 (b)). In the renewal weakest-link model, the probability of selecting a reliable segment with a given length l_i is $f_l(l_i)R_e(\sigma_N, l_i)\mathrm{d}l_i$. Hence, $R_s(\sigma_N, L, n)$ can be explained as the probability of selecting n number of reliable segments under the condition that $\sum_{i=1}^{n} l_i \leq L$, and a vacancy satisfying $l_{n+1} > L - \sum_{i=1}^{n} l_i$ at the same time, i.e.:

$$R_s(\sigma_N, L, n) = \int_0^L \int_0^{L-l_1} \cdots \int_0^{L-l_1-l_2\cdots-l_{n-1}} \left[\prod_{i=1}^{n} f_l(l_i)R_e(\sigma_N, l_i)\right] \cdot \\ \cdot \left[1 - F_l(L - l_1 - l_2 \cdots - l_n)\right] \mathrm{d}l_n \mathrm{d}l_{n-1} \cdots \mathrm{d}l_1 \tag{3.4}$$

In Eq. (3.4), the probability of selecting the first reliable segment is given by $\int_0^L f_l(l_1)R_e(\sigma_N, l_1)\mathrm{d}l_1$. The length of the second segment must satisfy $0 \leq l_2 \leq L - l_1$, and therefore the probability of selecting second reliable segment is given by $\int_0^{L-l_1} f_l(l_2)R_e(\sigma_N, l_2)\mathrm{d}l_2$. Following the same analysis, the probability of selecting ith reliable segment is given by $\int_0^{L-l_1\cdots-l_{i-1}} f_l(l_i)R_e(\sigma_N, l_i)\mathrm{d}l_i$, $1 \leq i \leq n$. The aforementioned consideration only enforces the condition $\sum_{i=1}^{n} l_i \leq L$. To further satisfy $l_{n+1} > L - \sum_{i=1}^{n} l_i$, the probability of selecting such a vacancy is equal to $[1 - F_l(L - l_1 - l_2 \cdots - l_n)]$.

In order to decrease the computational effort, the multiple integral in Eq. (3.4)

can be calculated by the following recursive expressions:

$$R_s(\sigma_N, x, n) = \int_0^x S_e(\sigma_N, l) R_s(\sigma_N, x-l, n-1) \mathrm{d}l \tag{3.5}$$

$$\text{and} \quad R_s(\sigma_N, L, 1) = \int_0^x S_e(\sigma_N, l) F_c(x-l) \mathrm{d}l \tag{3.6}$$

where

$$S_e(\sigma_N, l) = f_l(l) R_e(\sigma_N, l) \tag{3.7}$$

On the other hand, a reliable side-wall consists of all the combinations of reliable side-walls with different total V-notch number n. Beside, the events of a side-wall of having different total V-notch number n are mutually exclusive. As a result, the reliability of the entire side-wall of a given length L is obtained as

$$R(\sigma_N, L) = \sum_{n=0}^{\infty} R_s(\sigma_N, L, n) \tag{3.8}$$

Since the tensile specimen contains two side-walls whose failure statistics can be regarded as independent, the reliability of the entire specimen is computed by

$$R_{\sigma_N}(\sigma_N, L) = R(\sigma_N, L)^2 \tag{3.9}$$

Finally, the strength distribution of the tensile specimen is obtained by

$$F_{\sigma_N}(\sigma_N, L) = 1 - R_{\sigma_N}(\sigma_N, L) \tag{3.10}$$

The next step is to determine the reliability function $R_e(\sigma_N, l)$ as a function of both σ_N and l. In the present model, the reliability function $R_e(\sigma_N, l)$ is calculated based

on the statistical information of the random geometry of V-notches as well as a non-local stress based failure criterion. Consider a segment containing a V-notch under the tensile stress σ_N (Figure 3.1 (c)). The fracture of V-notches has been extensively studied, in which both stress-based failure criteria and energy-based failure criteria have been proposed [33, 89, 42, 74, 54, 72]. Since the focus of this chapter is limited to uniaxial tensile specimens, for which the failure mode is primarily mode I fracture [12], a simple non-local stress failure criterion is adopted. It is considered that the crack starts to propagate from the V-notch tip once the non-local stress σ at the notch tip reaches the corresponding material tensile strength, i.e.

$$\sigma = r_c^{-1} \int_0^{r_c} \sigma_{xx}(y) \mathrm{d}y = f_t \tag{3.11}$$

where r_c is an averaging length scale, σ_{xx} = tensile stress in $x-$direction, and f_t = material tensile strength. It should be pointed out that the choice of the non-local stress in the present failure criterion considers a finite fracture process zone formed around the notch tip, whose size is proportional to r_c. On the other hand, since the non-local stress is calculated from elastic analysis, we may rewrite the Eq. (3.11) as

$$\sigma_N Z(a, \theta, l) = f_t \tag{3.12}$$

where Z is the dimensionless stress, which depends on the notch depth a, notch angle θ, and segment length l.

By assuming the dimensionless stress Z is independent from the material strength f_t, the reliability function of the segments can be written as

$$R_e(\sigma_N, l) = \Pr(f_t/z \geq \sigma_N) = 1 - \int_0^{\infty} F_{f_t}(x\sigma_N) f_{Zl}(x, l)/f_l(l) \mathrm{d}x \tag{3.13}$$

where $F_{f_t}(x)$ is the CDF of material strength f_t, $f_{Zl}(x, l)$ is the joint PDF of dimen-

sionless stress Z and segment length l.

Based on Eqs. (3.12) and (3.13), $S_e(\sigma_N, l)$ in Eq. (3.7) becomes

$$S_e(\sigma_N, l) = f_l(l) - \int_0^\infty F_{f_t}(x\sigma_N) f_{Zl}(x, l)\mathrm{d}x \tag{3.14}$$

The material tensile strength f_t is considered to follow the Gauss-Weibull grafted distribution represented by Eqs. (1.24a)- (1.24b) [18, 67, 17].

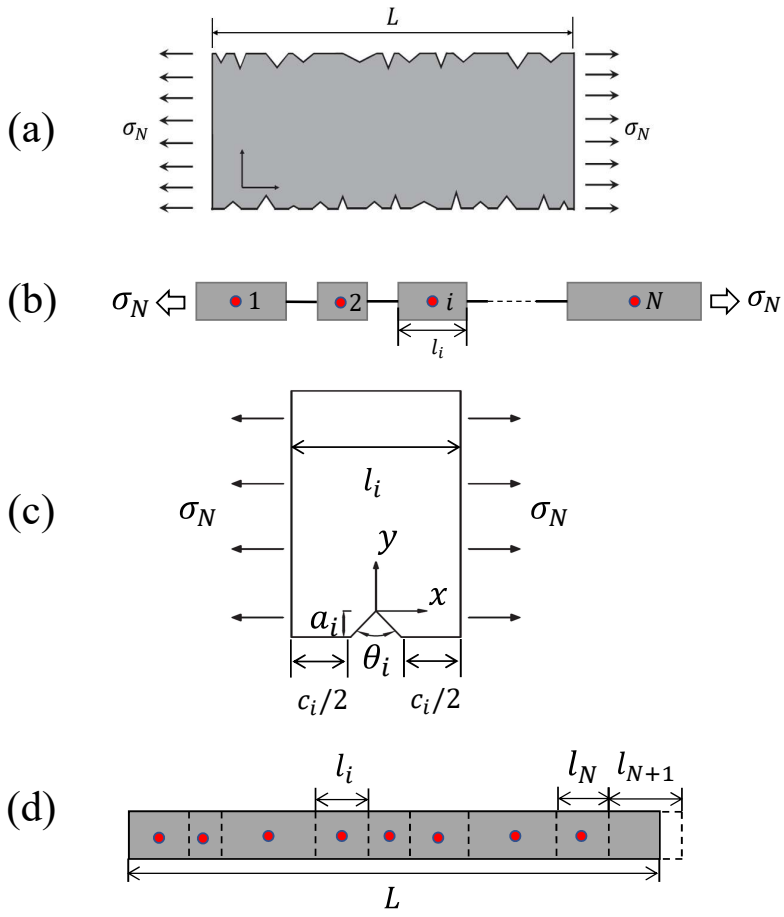

Figure 3.1: Illustration of the renewal weakest-link model: (a) schematic diagram of the ploy-Si MEMS tensile specimen, (b) schematic diagram of the renewal weakest-link model, (c) schematic diagram of the material segment, (d) formulation of renewal weakest-link model based on the renewal process.

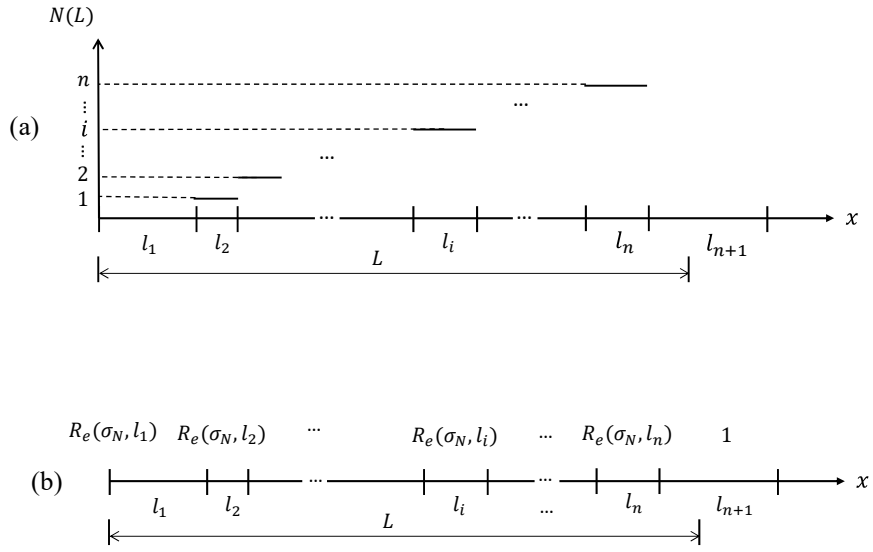

Figure 3.2: (a) a renewal process, (b) the renewal weakest-link model.

3.3 Large-size asymptotic behavior

This section investigates the behavior of the present model at the large-size limit (i.e. $L \to \infty$) through the stability postulate[49]. Consider a side-wall whose length is L and $L \to \infty$. We can divide the side-wall into p number segments of equal length L_p, where p is a finite number. Since $L \to \infty$, $L_p = L/p$ also approaches to infinity. Because the failure statistics of each V-notch is independent and one V-notch cannot be assigned to multiple segments, the failure statistics of each of the p segments is also independent. Furthermore, it is obvious that the failure of any of the p segments will trigger the failure of the entire side-wall. As a result, we obtain that

$$1 - P_f(\sigma_N) = [1 - P_{fp}(\sigma_N)]^p \tag{3.15}$$

where P_f is the failure probability of the entire side-wall, and P_{fp} is failure probability of a segment.

Since both the specimen length and segment length approach to infinity, the failure probability of the specimen and the segment must be of the same type of functions and differ only by a linear transformation, i.e. $P_{fp}(\sigma_N) = P_f(\frac{\sigma_N - b}{a})$, where $a, b =$ parameters depending on p. Substituting this expression into Eq. (3.15) yields

$$1 - P_f(\sigma_N) = \left[1 - P_f\left(\frac{\sigma_N - b}{a}\right)\right]^p \tag{3.16}$$

Eq. (3.16) is a functional equation representing the stability postulate. According to the extreme value theory [49, 63, 95], $P_f(\sigma_N)$ must be one of the three extreme value CDFs, whose choice is determined by its left-tail (domain of attraction).

In order to investigate the tail behavior of $P_f(\sigma_N)$, let us first determine the CDF of the total length of m segments, i.e. $F_L(L, m) = \Pr\left(\sum_{i=1}^{m} l_i \leq L\right)$. For the large-size limit, it is clear that m will be a large number. From the central limit theorem [41],

$F_L(L,m)$ would approach a Gaussian CDF:

$$F_L(L,m) \approx \Phi\left(\frac{L-m\mu_l}{\sqrt{m}\delta_l}\right) \tag{3.17}$$

where $\Phi(x)$ = standard Gaussian CDF, μ_l = the mean of l_i, and δ_l = standard deviation of l_i. From Eqs. (3.3) and (3.17), the probability that a side-wall of length L contains exact n number of V-notches can be approximated by the following formula

$$\begin{aligned} P_N(n,L) &= F_L(L,n) - F_L(L,n+1) && (3.18)\\ &\approx \Phi\left(\frac{L-n\mu_l}{\sqrt{n}\delta_l}\right) - \Phi\left[\frac{L-(n+1)\mu_l}{\sqrt{(n+1)}\delta_l}\right] && (3.19)\end{aligned}$$

Based on the central limit theory of renewal processes [35, 64], Eq. (3.18) can be further approximated by the following Gaussian PDF

$$P_N(n,L) \approx \frac{1}{\sqrt{2\pi L/\mu_l}\delta_l/\mu_l}\exp\left[-\frac{(n-L/\mu_l)^2}{2\delta_l^2 L/\mu_l^3}\right] \tag{3.20}$$

From Eq. (3.20), it is obvious that, as L increases, the mean value of N approaches L/μ_l, and the standard deviation of N approaches $\omega_l\sqrt{L/\mu_l}$ (ω_l = coefficient of variation (CoV) of l_i). Therefore, the CoV of n decay with $L^{-1/2}$ for a large L.

Since the dimensionless stress is usually bounded ($Z \in [1, z_m]$), at small stress values, Eq. (3.13) can be expressed by

$$R_e(\sigma_N, l) = 1 - \left[\frac{1}{f_l(l)}\int_0^{z_m} x^{m_W} f_{Zl}(x,l)\mathrm{d}x\right]\left(\frac{\sigma_N}{s_0}\right)^{m_W} \tag{3.21}$$

Substituting Eq. (3.21) into Eq. (3.4) yields

$$R_s(\sigma_N, L_p, n) = \int_0^{L_p} \int_0^{L_p - l_1} \cdots \int_0^{L_p - l_1 - l_2 \cdots - l_{n-1}} \left\{ \prod_{i=1}^{n} f_l(l_i) \left[1 - \psi(l_i)(\sigma_N / s_0)^{m_W} \right] \right\} \cdot \\ \cdot F_c(L_p - l_1 - l_2 \cdots - l_n) \mathrm{d}l_n \mathrm{d}l_{n-1} \cdots \mathrm{d}l_1 \tag{3.22}$$

where $\psi(l) = \int_0^{z_m} x^{m_W} f_{Zl}(x, l) \mathrm{d}x / f_l(l)$.

By expanding the term $\prod_{i=1}^{n} f_l(l_i) \left[1 - \psi(l_i)(\sigma_N / s_0)^{m_W} \right]$ and retaining the leading terms up to the order $\sigma_N^{m_W}$, it is obtained that

$$\prod_{i=1}^{n} f_l(l_i) \left[1 - \psi(l_i)(\sigma_N / s_0)^{m_W} \right] \approx \prod_{i=1}^{n} f_l(l_i) - \left(\prod_{i=1}^{n} f_l(l_i) \right) \left(\sum_{i=1}^{n} \psi(l_i) \right) (\sigma_N / s_0)^{m_W} \tag{3.23}$$

where $\sigma_N \to 0$.

Therefore, Eq. (3.22) can be rewritten as

$$R_s(\sigma_N, L, n) = P_N(n, L) - C(n, L) \left(\frac{\sigma_N}{s_0} \right)^{m_W} \tag{3.24}$$

where:

$$P_N(n, L) = \int_0^{L} \int_0^{L - l_1} \cdots \int_0^{L - l_1 - l_2 \cdots - l_{n-1}} \prod_{i=1}^{n} f_l(l_i) \cdot \tag{3.25}$$

$$\cdot F_c(L - l_1 - l_2 \cdots - l_n) \mathrm{d}l_n \mathrm{d}l_{n-1} \cdots \mathrm{d}l_1 \tag{3.26}$$

$$C(n, L) = \int_0^{L} \int_0^{L - l_1} \cdots \int_0^{L - l_1 - l_2 \cdots - l_{n-1}} \left(\prod_{i=1}^{n} f_l(l_i) \right) \left(\sum_{i=1}^{n} \psi(l_i) \right) \cdot \tag{3.27}$$

$$\cdot F_c(L - l_1 - l_2 \cdots - l_n) \mathrm{d}l_n \mathrm{d}l_{n-1} \cdots \mathrm{d}l_1 \tag{3.28}$$

Noting that $\sum_{n=1}^{\infty} P_N(n, L) = 1$, the reliability of the side-wall (Eq. (3.8)) becomes

$$R(\sigma_N, L) = 1 - \sum_{n=1}^{\infty} C(n, L) \left(\frac{\sigma_N}{s_0} \right)^{m_W} \qquad (\text{as } \sigma_N \to 0) \tag{3.29}$$

$$\text{or:} \quad P_f(\sigma_N, L) \approx C \left(\frac{\sigma_N}{s_0} \right)^{m_W} \qquad (\text{as } \sigma_N \to 0) \tag{3.30}$$

where $C = \sum_{n=1}^{\infty} C(n, L)$.

Eq. (3.30) indicates that the strength distribution of a side-wall has a power-law left tail. Based on the extreme value theory, P_f must obey the Weibull distribution:

$$P_f(\sigma_N) = 1 - \exp\left[-(\sigma_N / s_1)^{m_W}\right] \tag{3.31}$$

where s_1 = the Weibull scale parameter.

Since the specimen consists of two side-walls, the strength distribution of the entire specimen can be calculated by

$$F_{\sigma_N}(\sigma_N, L) = 1 - \left[1 - P_f(\sigma_N)\right]^2 \tag{3.32}$$

Substituting Eq.(3.31) into Eq.(3.32) yields

$$F_{\sigma_N}(\sigma_N, L) = 1 - \exp\left[-(\sigma_N / s_0)^m\right] \tag{3.33}$$

where $s_0 = (1/2)^{1/m} s_1$.

At this point, it is demonstrated that, at the large-size limit, the strength distribution of the entire specimen follows the Weibull distribution.

3.4 Comparison with experimental data

In this section, the renewal weakest-link model is validated through the comparison with the measured strength distributions of uniaxial tensile poly-Si MEMS specimens. We examined the model through two sets of experimental data. The first set consists of experimental strength distributions of poly-Si tensile specimens of two gauge lengths (L = 20 and 70 μm), which is the same data used in Section2.3 [60, 85]. The second data set consists of experimental strength distributions of poly-Si tensile specimens of gauge lengths of 7 and 70 μm, which were tested by the on-chip tester [88]. It should be pointed out that, for both data sets, the specimens were produced by Sandia's SUMMiT V poly-Si microfabrication process [92], which therefore can be assumed to share the similar statistical properties of the side-wall geometry.

The first step to used the present model is to determine the dimensionless stress Z as a deterministic function of segment length l, notch depth a, and notch angle θ through a series of finite element simulations. Since the specimen width is significantly grater than the notch depth and the spacing of the adjacent V-notches is usually considerably larger than the size of the fracture process zone, it is reasonable to assume that all the V-notches are noninteracting for calculating the elastic stress field of the near-tip region. In the finite element simulations, we consider a segment of uniaxial tensile specimen containing a V-notch at the middle of the side-wall under a unit far-field stress ($\sigma_N = 1$) (as shown in Figure 3.1 (c)). The material is modeled as an isotropic elastic material with a Young modulus E = 156 GPa and a Poisson ratio $\mu = 0.22$ [84]. The averaging zone size r_c (Eq. (3.11)) is set to be 5 nm, which is on the order of the fracture process zone size of poly-Si [103, 84, 65].

The next step is to obtain the statistical information about the segment length l and the dimensionless stress Z that required by the model. The random geometry of the side-wall can be characterized by three random variables (Figure 3.1 (c)): (1)

the notch angle θ, (2) the notch depth a, and (3) the notch spacing c. Following the study of Chapter 2, we consider the following PDFs for the distribution of θ, a and c:

$$f_\theta(\theta) = \frac{1}{120} \qquad (20^\circ < \theta < 140^\circ) \tag{3.34}$$

$$f_a(a) = 0.232 \left(\frac{62-a}{28}\right)^{5.5} \exp\left[-\left(\frac{62-a}{28}\right)^{6.5}\right] \qquad (0 \le a \le 62 \text{ nm}) \tag{3.35}$$

$$f_c(c) = \frac{1}{600} \qquad (100 \text{ nm} \le c \le 700 \text{ nm}) \tag{3.36}$$

where f_θ, f_a and f_c are the PDFs of θ, a, and c, respectively.

Based on the geometry of the V-notches (shown in Figure 3.1 (c)), the segment length can be calculated as $l = c + 2a\tan(\theta/2)$. The PDF of l can be analytically calculated as

$$f_l(l) = \int_0^l \int_0^\infty f_c(l-x) \frac{4}{4y+y^3} f_\theta\left(2\tan^{-1}(y/2)\right) f_a(x/y) \mathrm{d}y \mathrm{d}x \tag{3.37}$$

Figure 3.3 shows the comparison between the PDF of segment length based on Eq. (3.37) and the corresponding result from Monte Carlo simulation, which agree well with each other.

The analytical formula for the joint PDF of dimensionless stress and segment length seems inaccessible, therefore we resort to the Monte Carlo simulations. A total of 10^7 groups of a, θ and c are sampled from the distribution functions described by Eq. (3.34), (3.35), and (3.36). For each group of a, θ and c, the corresponding values of Z and l are computed by interpolating the dimensionless stress $Z(a, \theta, l)$ obtained by finite element simulation and the relation that $l = c + 2a\tan(\theta/2)$ respectively. Then a new group of Z and l can be obtained, which is used to numerically calculate the joint PDF $f_{Zl}(z, l)$ (shown in Figure 3.4).

The last step is to calibrate the model parameters of the strength distribution

F_{f_t} by fitting the present model to the experimenal strength distribution of poly-Si MEMS specimens. According to Eqs. (1.24a) and (1.24b), there are six parameters, while only four of them are independent parameters. The four independent parameters chosen for the fitting are the Weibull modulus m_W, the Weibull scale parameter s_W, the Gaussian mean value μ_G and the Gaussian standard deviation δ_G for the calibration. Figure 3.5 and Figure 3.6 show the optimum fitting results of the measured strength distributions of poly-Si MEMS specimens. The corresponding fitted parameters for the material strength distribution are listed as follows: set 1: $\mu_G = 16.5$ GPa, $\delta_G = 0.99$ GPa, $m_W = 64$, $s_W = 15.4$ GPa; set 2: $\mu_G = 17.2$ GPa, $\delta_G = 1.03$ GPa, $m_W = 64$, $s_W = 16.1$ GPa. It is noted that the calibrated mean strength of silicon, μ_G, is quite close to the theoretical strength of silicon predicted by ab initio simulations [39]. From Figure 3.5 and Figure 3.6, it is seen that the present model can match the measured strength distributions of specimens of two different gauge lengths, using the same group of model parameters. At this point, it should be pointed out that, as shown in Figure 1.4, the measured strength distributions of poly-Si MEMS structures cannot be captured by a the classical Weibull model, which always predicts strength distribution is a straight line on the Weibull plot. However, the measured strength distributions exhibit an obvious curved behavior on the Weibull plot. And such a curve can be well captured by the present model.

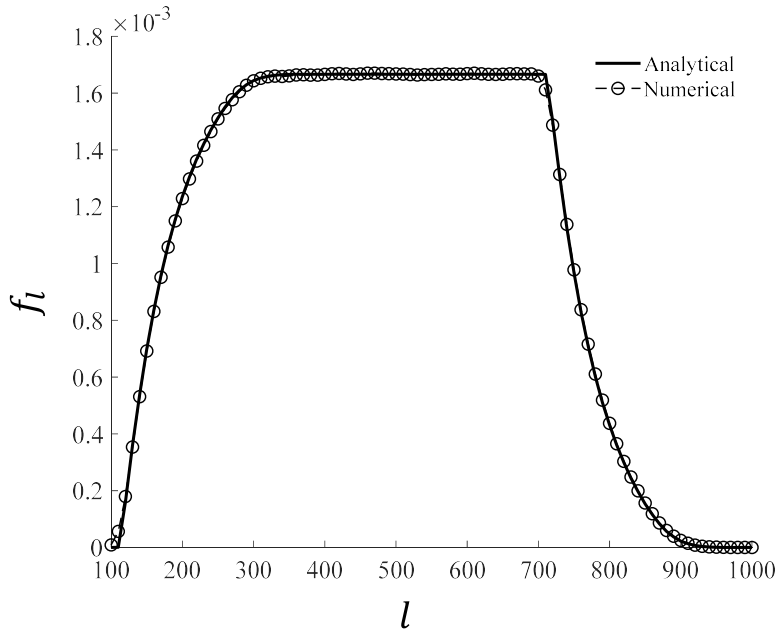

Figure 3.3: Calculated PDF of the segment length for specimens.

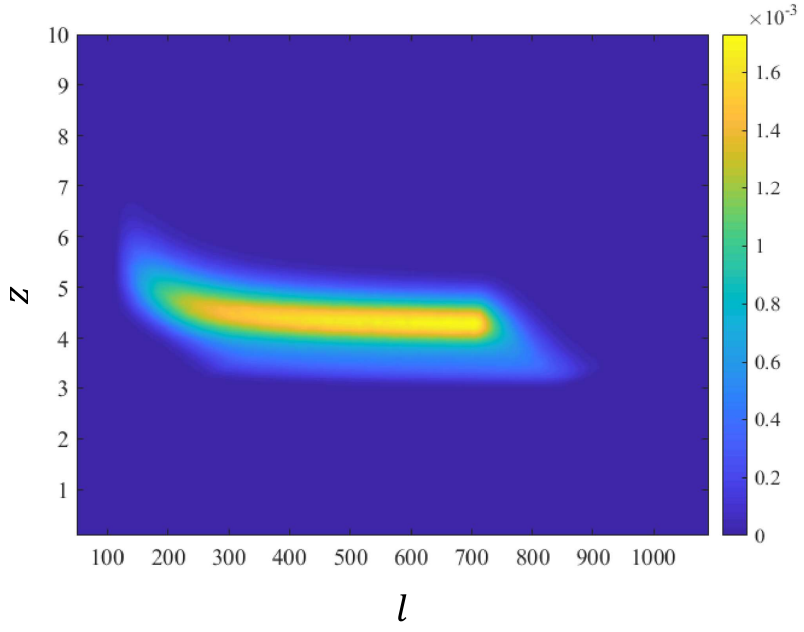

Figure 3.4: Joint PDF $f_{Zl}(z, l)$ of the dimensionless stress and the segment length.

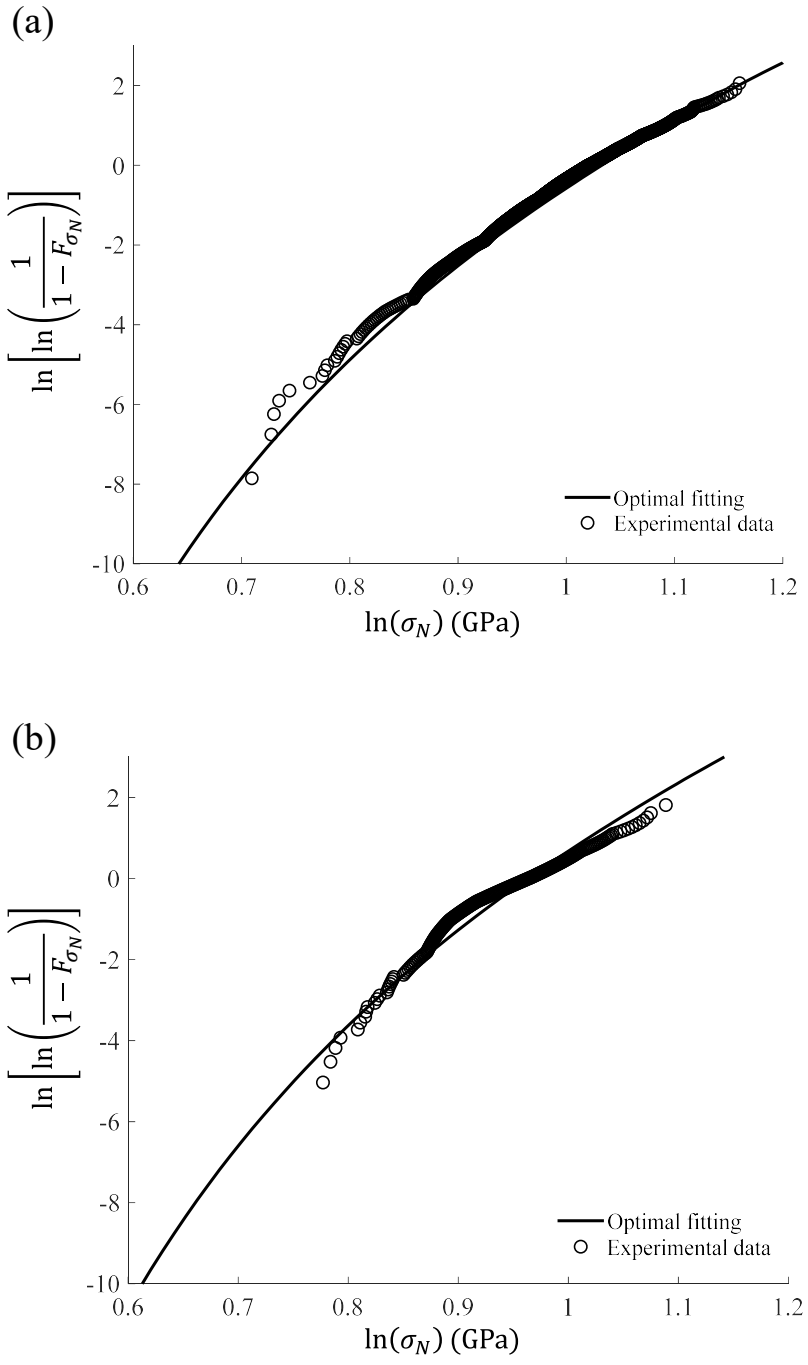

Figure 3.5: Optimum fittings of the measured strength histograms (data set 1) by the present model:(a) $L = 20$ μm, (b) $L = 70$ μm.

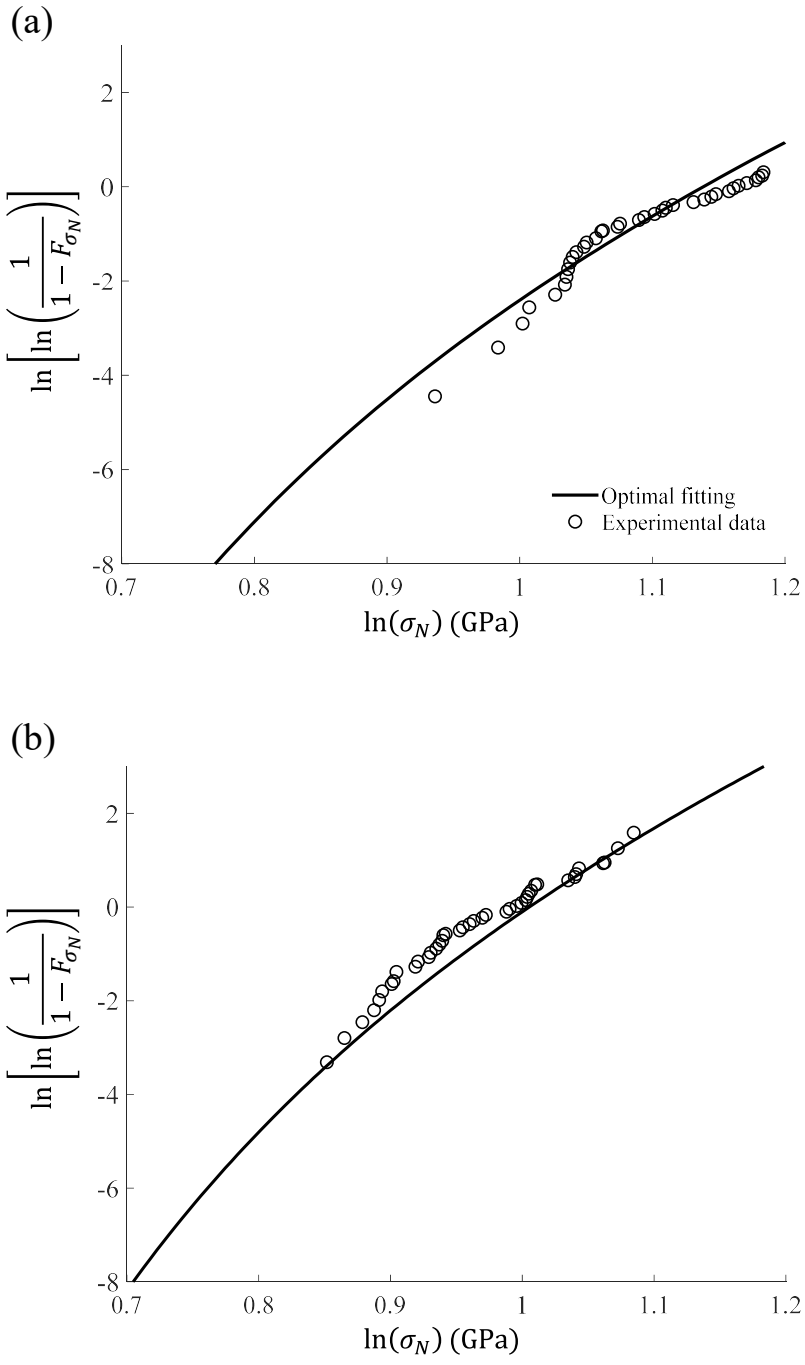

Figure 3.6: Optimum fittings of the measured strength histograms (data set 2) by the present model:(a) $L = 7$ μm, (b) $L = 70$ μm.

3.5 Simplified calculation approach

A majority of computational cost of the present model is spent on the evaluation of Eq. (3.4), which is handled by the recursive equations (Eqs. (3.5) - (3.7)). However, for a long specimen, the recursive computation method is tedious and also expensive. Therefore, it would be desirable to develop a simplified calculation method.

One way to avoid evaluating the multiple integration of Eq. (3.4) is to approximate the reliability function of each segment by a function that is independent of segment length. One reasonable choice is the expectation of the segment reliability, i.e.:

$$\bar{R}_e(\sigma_N) = \int_0^\infty R_e(\sigma_N, l) f_l(l) \mathrm{d}l \tag{3.38}$$

$$= 1 - \int_0^\infty F_{f_t}(x\sigma_N) f_z(x) \mathrm{d}x \tag{3.39}$$

where $f_z(x) = \int_0^\infty f_{Zl}(x, l)\mathrm{d}x$ = marginal PDF of the dimensionless stress. The error cause by this approximation can be evaluated by

$$\Delta_1(\sigma_N) = \int_0^\infty f_l(l) \frac{|R_e(\sigma_N, l) - \bar{R}_e(\sigma_N)|}{R_e(\sigma_N, l)} \mathrm{d}l \tag{3.40}$$

As will be shown later, $\Delta_1(\sigma_N)$ is negligibly small for the specimens considered here.

Based on Eq. (3.38), the reliability of a single side-wall can be expressed by

$$R(\sigma_N, L) \approx \sum_{n=1}^{\infty} P_N(n, L) \left[\bar{R}_e(\sigma_N)\right]^n \tag{3.41}$$

where $P_N(n, L)$ can be computed by Eq. (3.3), which is probability that the side-wall contains exactly n V-notches. By taking the logarithm of Eq. (3.41), we obtain that

$$\ln R(\sigma_N, L) = \ln \{\mathrm{E}_n[Y(\sigma_N, n)]\} \tag{3.42}$$

where $Y(\sigma_N, n) = \left[\bar{R}_e(\sigma_N)\right]^n$, and $\mathrm{E}_n[\cdot]$ = expectation operator with respect to n. The logarithm of the expectation of $Y(\sigma_N, n)$ can be further approximated by $\ln\{\mathrm{E}_k[Y(\sigma_N, n)]\} \approx \mathrm{E}_n\{\ln Y(\sigma_N, n)]\} + \frac{1}{2}\omega_Y^2(\sigma_N, L)$, where $\omega_Y(\sigma_N, L)$ = CoV of $Y(\sigma_N, n)$. It will be shown later that, for MEMS specimens considered in this chapter, we may drop the term $\frac{1}{2}\omega_Y^2(\sigma_N, L)$ and consider

$$\ln\{\mathrm{E}_n[Y(\sigma_N, n)]\} \approx \mathrm{E}_n\{\ln Y(\sigma_N, n)]\} \tag{3.43}$$

The relative error of the approximation in Eq. (3.43) can be calculated as

$$\Delta_2(\sigma_N, L) = \left|1 - \frac{\mathrm{E}_n\{\ln Y(\sigma_N, n)\}}{\ln\{\mathrm{E}_n[Y(\sigma_N, n)]\}}\right| \tag{3.44}$$

By using Eq. (3.43), Eq. (3.42) can be rewritten as

$$\begin{aligned} \ln R(\sigma_N, L) &\approx \mathrm{E}_n\{\ln Y(\sigma_N, n)]\} && (3.45)\\ &= \sum_{n=1}^{\infty} P_N(n, L) n \bar{R}_e(\sigma_N) = \mu_N(L)\bar{R}_e(\sigma_N) && (3.46) \end{aligned}$$

where $\mu_N(L)$ = mean of N for a given side-wall length L. Eq. (3.46) suggests that the overall reliability of the specimen can be approximately calculated as

$$R_{\sigma_N}(\sigma_N, L) = \left[\bar{R}_e(\sigma_N)\right]^{2\mu_N(L)} \tag{3.47}$$

Eq. (3.47) can be considered as an equivalent weakest-link model, which uses the expectations of the segment number and the segment reliability.

Figure 3.7 plots the probability distributions of the number of V-notches for different specimen sizes with comparison to Eq. (3.20). It is observed that as the specimen length increases, the distribution of N approaches Eq. (3.20), which justifies the analysis of the large-size asymptotic behavior in Section 3.3. In fact, Eq. (3.20) could

provide a reasonable approximation of the distribution of N even for intermediate specimen size $L > 20$ μm. It is also found that, for all specimen lengths, $\mu_N(L)$ can be reasonably approximated as $\mu_N(L) = L/\mu_l$, which suggests the RVE size of the finite weakest-link model is just the mean segment length of the present model.

As a demonstration, this simplified calculation method is applied to recalculate the strength distribution of poly-Si MEMS specimens with its parameters calibrated by data set 1. Here we consider four different specimens sizes $L = 1.5,\ 20,\ 200,\ 2000$ μm. Figure 3.8 shows that the strength distributions of these MEMS specimens calculated by the full model (Eq. (3.4) (3.8) and (3.9)) and the simplified model (Eq. (3.47)). It is found that these two models agree with each other very well for specimens of $L = 20,\ 200,\ 2000$ μm, which covers the typical size range of MEMS specimens. For the smallest specimen, two models deviate from each other at the high stress regime ($\sigma_N \geq 3.7$ GPa). To explain this phenomenon, we examine the two main approximations introduced in the simplified method (i.e. Eqs. (3.41) and Eq. (3.43)). Figure 3.9 shows the expectation of the relative error, $\Delta_1(\sigma_N)$. It is seen that the expected relative error increases with the nominal stress σ_N, which grows beyond 1% as $\sigma_N > 4.2$ GPa. Meanwhile, the relative error $\Delta_2(\sigma_N, L)$ due to Eq. (3.43) for different specimen lengths is plotted in Figure 3.10. It is seen that the relative error $\Delta_2(\sigma_N, L)$ is below 10^{-3} for specimens of $L = 20,\ 200,\ 2000$ μm. For specimen of $L = 1.5$ μm, the error is larger than 1% when $\sigma_N > 4$ GPa.

As a result, the errors induced by the two approximations represented by Eqs. (3.41) and (3.43) are negligibly small for a typical MEMS structure. This indicates that the proposed simplified method can be applied to most MEMS specimens. Compared to Eqs. (3.4), (3.8) and (3.9), the simplified model (Eq. (3.47)) is far more efficient in term of computational cost. This makes the computation of the present renewal weakest-link model similar to the conventional weakest-link model [65].

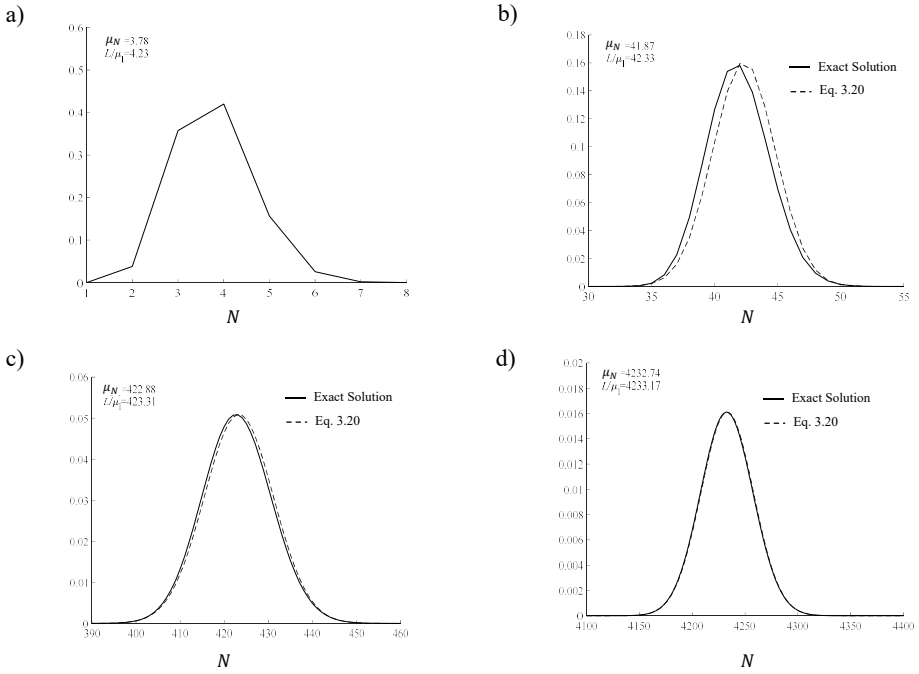

Figure 3.7: Distributions of the number of V-notches for different specimen lengths: (a)$L = 1.5$ μm, (b)$L = 20$ μm, (c)$L = 200$ μm, (d)$L = 2$ mm.

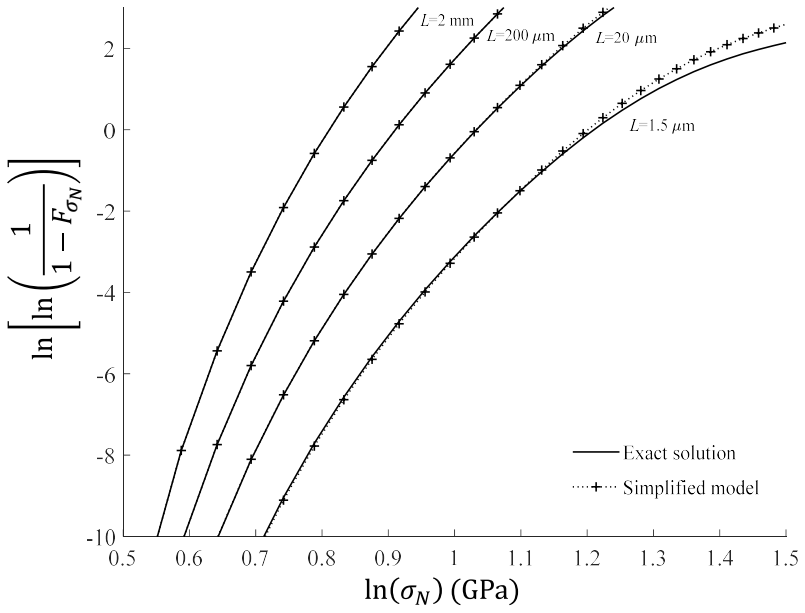

Figure 3.8: Comparison of the strength distributions of MEMS specimens predicted by the renewal weakest-link model and the simplified model.

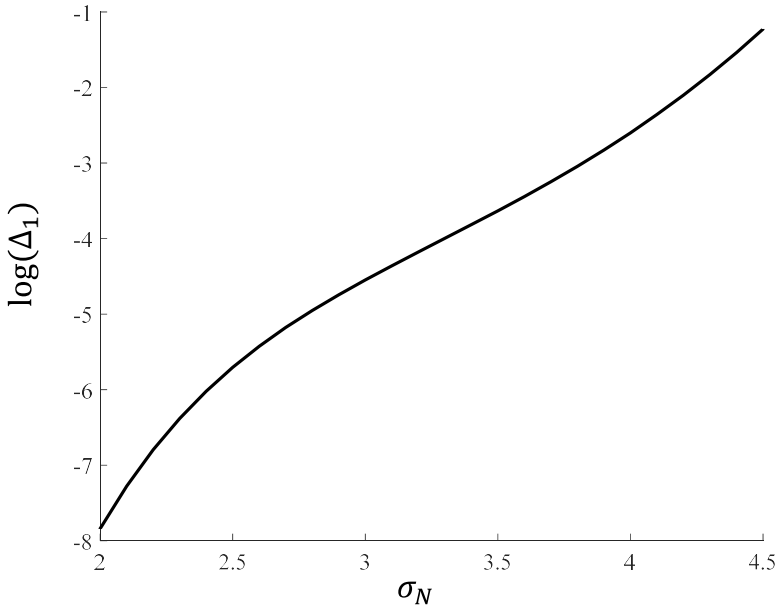

Figure 3.9: Plot of relative error Δ_1.

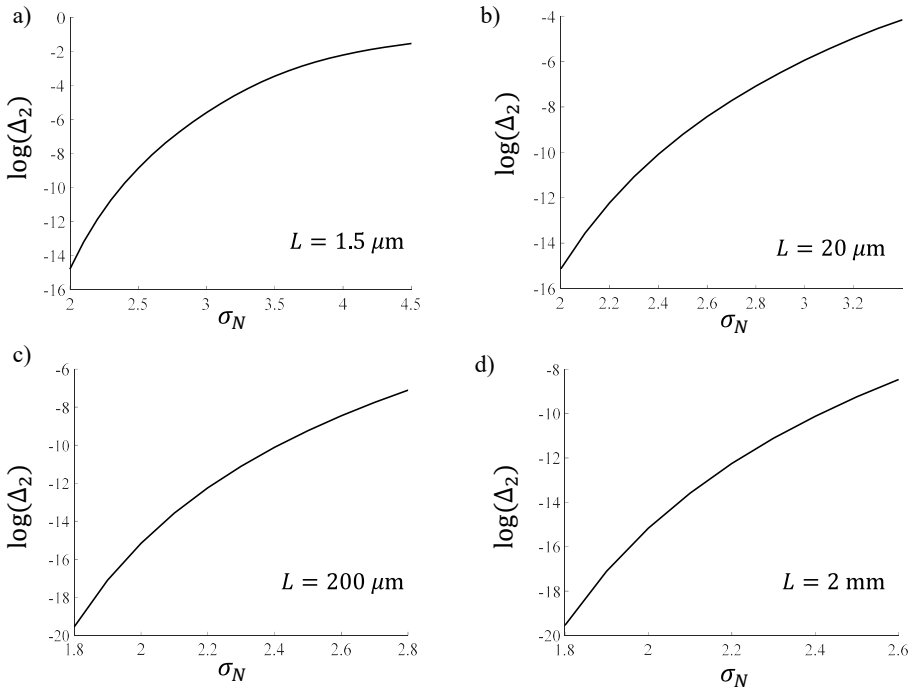

Figure 3.10: Plot of relative error Δ_2.

3.6 Conclusions

In this chapter, a renewal weakest-link model is developed for strength statistics of uniaxial tensile poly-Si MEMS specimens. The model explicitly takes into account the random spacing of the side-wall grooves. The model prediction of the structural strength distribution agrees well with the measured strength distribution of poly-Si MEMS specimens of different lengths.

It is shown that, the present model predicts a Weibullian strength distribution at the large-size limit, which is in consistence with the extreme value theory.

We demonstrate that present model can be approximated by an equivalent weakest-link model, which only relies on the average number of surface grooves and the expected reliability function of each groove. This simplification provides an efficient method for determining the strength distribution of MEMS specimens.

Chapter 4

A Generalized First-Passage Model and Its Application to Power-Law Tail Behavior of Structural Strength Distribution

4.1 Introduction

As discussed in Chapter 1, one challenging problem in structural strength statistics is the determination the functional form of the probabilistic model. For brittle structures and large-size quasi-brittle structures, their strength distribution can be well described by the Weibull distribution. This implies that the left tail of the structural strength distribution must follow a power-law function. For small and intermediate size quasi-brittle structures, the structural strength distribution can be captured by the finite weakest-link model using the Gauss-Weibull grafted distribution as the distribution of the material strength. In this case, the left tail of the strength distribution is also a power-law function (Section 1.4). Hence, we may conclude that the power-law tail behavior is common for strength distribution of brittle and quasi-brittle structures. However, the origin of this power-law tail behavior remains unclear.

Freudenthal was the first one who attempted to explain the power-law tail behavior

based on an assumed distribution for the random flaw sizes and linear elastic fracture mechanics (LEFM) [52]. His hypothesis was based on the following assumptions: (1) the largest flaw size follows the Fréchet distribution and local material strength (i.e. fracture toughness) is deterministic; (2) the strength of the material element is governed by the largest flaw in the element through LEFM; and (3) the flaws inside the material element are non-interacting. It is evident that, Freudenthal's analysis of the power-law tail behavior of structural strength distribution rests on an assumed flaw distribution, which does not give a complete justification of the power-law tail distribution. Furthermore, the assumption of a deterministic material strength is not realistic [81, 67]. Nevertheless, Freudenthal's pioneering work shed light on the necessity of incorporating both probabilistic methods and fracture mechanics to study the failure statistics of structures.

On the other hand, a series of recent studies conducted by Bazănt and his co-workers suggested that the power-law tail of structural strength distribution stems from the left power-law tail of material strength distribution [81, 67], which is the Gauss-Weibull grafted distribution (Eqs. (1.24a) and (1.24b)). The Gauss-Weibull grafted distribution was derived from the transition rate theory of nanoscale fracture combined with a hierarchical statistical model [18, 67, 17], whose left tail is a power-law function. By assuming the applied stress to be deterministic, it is obtained that left tail of the strength distribution of the material element will be a power-law function. Compared to the aforementioned Freudenthal's analysis, this model considers the randomness of material strength, while the randomness of the applied stress field was not explicitly included.

However, for many quasi-brittle materials, such as concrete, ceramics, and rock, the randomly distributed flaw sizes and the spatial variability of local material strength coexist. Therefore, it is logical to combine the analyses of flaw statistics as well as the random material strength for studying the tail behavior of the strength distribution.

In Chapter 2, the first-passage model is proposed for the strength statistics of ploy-Si MEMS structures, which takes into account the randomness and the autocorrelation of both the material strength field and the applied stress field. In Section 2.5, it is demonstrated that the power-law tail behavior of structural strength distribution stems from the left power-law tail of material strength distribution. The distribution of applied stress field, which is influenced by the randomly distributed flaws, will not change the functional form of the left tail of structural strength distribution. However, the model is limited to 1-dimensional description, which is clearly not sufficient for most engineering structures.

In order to describe the strength distribution of ordinary brittle and quasi-brittle structures, we generalize the first-passage model to n-dimensional space. The generalized model is applied to study to power-law tail behavior of strength distribution of brittle and quasi-brittle structures. This chapter is planed as follows: Section 4.2 presents the model formulation of the n-dimensional first-passage model; Section 4.3 demonstrates the first-passage analysis in higher dimensional cases; Section 4.4 presents the model predictions of structural strength distribution and the corresponding numerical verifications; Section 4.5 discusses the original of the power-law tail of structural strength distribution.

4.2 Model formulation

Similar to the formulation of 1-dimensional first-passage model proposed in Chapter 2, we assign a random variable to each point to measure its failure state. The failure state of every point in the domain forms a random field, represented by $\eta(\mathbf{x})$, where $\mathbf{x}$ is a Cartesian coordinate vector of an $n-$dimensional space. Similar to Eq. (2.1), the random field, $\eta(\mathbf{x})$, can be further written as the different between the material

strength field $f_t(\mathbf{x})$ and the non-local stress field $\sigma(\mathbf{x})$, i.e:

$$\eta(\mathbf{x}) = f_t(\mathbf{x}) - \sigma(\mathbf{x}) \tag{4.1}$$

The non-local stress field $\sigma(\mathbf{x})$ is expressed as a local averaging of the maximum elastic principal stress field, i.e.:

$$\sigma(\mathbf{x}) = \frac{1}{V_\alpha} \int_V \alpha(|\mathbf{x} - \mathbf{x}'|) \langle \sigma_e(\mathbf{x}) \rangle \mathrm{d}V(\mathbf{x}') \tag{4.2}$$

where $\sigma_e(\mathbf{x})$ = the maximum elastic principal stress field, $\alpha(|\mathbf{x} - \mathbf{x}_0|)$ = non-local averaging function, $V_\alpha = \int_V \alpha(|\mathbf{x} - \mathbf{x}_0|)\mathrm{d}V(\mathbf{x})$, and $\langle x \rangle = \max(x, 0)$. It should be noted that, the damage localization mechanism, which is the most common failure mechanism for brittle and quasi-brittle structures, is taken into account by choosing suitable V_α and α [21, 16]. The nominal stress σ_N is defined as $\sigma_N = P/(bD)$ (P = applied load, D = characteristic size of the structure, and b = width of the structure in the transverse direction). Since the non-local tensile stress is calculated from the elastic stress field, we can write that

$$\sigma(\mathbf{x}) = \sigma_N Z(\mathbf{x}) \tag{4.3}$$

where $Z(\mathbf{x})$ = dimensionless stress field.

We consider that the failure of any material point would trigger the failure of the entire structure under controlled load. Therefore, the structural strength CDF, which equals the failure probability of the structure subjected to a nominal stress σ_N, can be expressed by:

$$F_{\sigma_N}(\sigma_N, \Omega) = 1 - Pr\left[\eta(\mathbf{x}) = f_t(\mathbf{x}) - \sigma_N Z(\mathbf{x}) > 0,\ \forall \mathbf{x} \in \Omega\right] \tag{4.4}$$

where Ω denotes the domain of the structure.

Since the focus of the present study is on the tail behavior of the strength distribution, it is not unduly restrictive to consider a uniaxial tensile specimen. In this case, it is reasonable to consider the strength field and the dimensionless stress field, i.e. $f_t(\mathbf{x})$ and $Z(\mathbf{x})$, as two isotropic stationary fields. Therefore, they can be decomposed into the mean values and the corresponding random components, i.e.:

$$f_t(\mathbf{x}) = \mu_{f_t} + f_{t0}(\mathbf{x}) \tag{4.5a}$$

$$Z(\mathbf{x}) = \mu_z + Z_0(\mathbf{x}) \tag{4.5b}$$

where μ_{f_t} and μ_Z are the mean values of the random fields $f_t(\mathbf{x})$ and $Z(\mathbf{x})$, respectively; and $f_{t0}(\mathbf{x})$ and $Z_0(\mathbf{x})$ are the corresponding zero mean random components.

By substituting Eqs. (4.5a) and (4.5b) into Eq. (4.4), the CDF of structural strength can be written as

$$F_{\sigma_N}(\sigma_N, \Omega) = 1 - Pr\left[\eta_0(\mathbf{x}) < \lambda(\sigma_N),\ \forall \mathbf{x} \in \Omega\right] \tag{4.6}$$

where

$$\eta_0(\mathbf{x}) = \sigma_N Z_0(\mathbf{x}) - f_{t0}(\mathbf{x}); \quad \lambda(\sigma_N) = \mu_{f_t} - \sigma_N \mu_z \tag{4.7}$$

Obviously, Eq. (4.6) is the first-passage probability of the $n-$dimensional zero mean random field $\eta_0(\mathbf{x})$ with respect to the up-crossing barrier $\lambda(\sigma_N)$, whose calculation method is presented in Section 4.3.

4.3 First-passage analysis in higher dimensions

Let $\eta_0(\mathbf{x})$ be an $n-$dimensional zero mean isotopic stationary random field that defined on a domain Ω. When the barrier is sufficiently high, it is reasonable to consider that the individual crossing events are statistically independent. Therefore, the crossing events can be modeled by a Poisson process, whose Poisson intensity is related to the corresponding crossing rate. In this way, the probability that the field $\eta_0(\mathbf{x})$ will up cross a high barrier λ at least once can be represented by[94, 95]

$$F(\lambda) \approx 1 - F_{\eta_0}(\lambda) \exp\left[-\frac{\mu_{\eta_0}(\lambda)}{F_{\eta_0}(\lambda)} V_\Omega\right] \tag{4.8}$$

where F_{η_0} is the marginal CDF of the random field $\eta_0(\mathbf{x})$; $V_\Omega = \int_\Omega \mathrm{d}x_1 \cdots \mathrm{d}x_n$, which is the size of domain Ω; and $\mu_{\eta_0}(\lambda)$ is the crossing rate of $\eta_0(\mathbf{x})$ with respect to the crossing barrier λ.

For a non-Gaussian random field $\eta_0(x)$, since $\eta_0(x)$ is not independent from the fields of its spatial derivatives, its crossing rate is difficult to evaluate. To circumvent this dilemma, we first translated the non-Gaussian field $\eta_0(\mathbf{x})$ into a standard Gaussian field $Y(\mathbf{x})$ [56, 57]. The translated standard Gaussian field $Y(\mathbf{x})$ is related to the original field $\eta_0(\mathbf{x})$ by matching their marginal CDFs and covariance functions, i.e.:

$$\eta_0(\mathbf{x}) = \Phi^{-1}\left\{F_{\eta_0}[\eta_0(\mathbf{x})]\right\} \tag{4.9}$$

$$R_{\eta_0}(|\Delta\mathbf{x}|) = \int_{-\infty}^{+\infty}\int_{-\infty}^{+\infty} F_{\eta_0}^{-1}\left[\Phi(y_1)\right] F_{\eta_0}^{-1}\left[\Phi(y_2)\right] \phi\left[y_1, y_2, R_Y(|\Delta\mathbf{x}|)\right] \mathrm{d}y_1 \mathrm{d}y_2 \tag{4.10}$$

where $\Phi(x)$ = standard Gaussian CDF; ϕ = bivariate Gaussian PDF; $R_{\eta_0}(|\Delta\mathbf{x}|)$ and $R_Y(|\Delta\mathbf{x}|)$ are the covariance functions of the random fields $\eta_0(\mathbf{x})$ and $Y(\mathbf{x})$, respectively; and $|\Delta\mathbf{x}|$ = distance between any two points. According to Eq. (4.9),

the original crossing barrier λ is also translated to a new crossing barrier λ_Y, i.e.:

$$\lambda_Y = \Phi^{-1}\left[F_{\eta_0}(\lambda)\right] \tag{4.11}$$

The crossing rate for an $n-$dimensional stationary field, which is the mean number of crossings per unit domain, has been extensively investigated for decades [94, 95, 3, 5]. In order to compute the crossing rate, the first step is to define the number of crossings. If we define the parts of the field that stay above the crossing barrier as the excursion set, then the number of crossings is just the number of connected components of the excursion set. Based on this interpretation, the crossing rate can be related to the differential topology characteristic of the excursion set [3, 5]. If the crossing barrier is sufficiently high, it is reasonable to assume the shapes of the connected components of the excursion set are always solid. Hence, the number of connected components of the excursion set becomes the Euler characteristic of the excursion set, which also equals the number of crossings. And the Euler characteristic of the excursion set can be quantified by the number of some characteristic points.

Here we use a 2-dimensional isotropic stationary Gaussian fields as an example to demonstrate this concept. Given a 2-dimensional isotropic stationary Gaussian fields $Y(x_1, x_2)$ and an up-crossing barrier λ_Y. One realization of the excursion set $A = \{x_1, x_2 : Y(x_1, x_2) > \lambda_Y\}$ is shown in Figure 4.1 (a). It is obvious that the number of crossings is 2, which is just the number of connected components (shaded areas) of the excursion set A. If the crossing barrier λ_Y is sufficiently high, we can assume the connected components of the excursion set A are always solid (the probability of having a connected components shown in Figure 4.1 (b) is negligible). The Euler characteristic of any shaped solid connected component is always 1, which is a topological invariant. Besides, Euler characteristic is also additive, i.e., the Euler characteristic of n connected components is just the summation of the Euler characteristic of each

one. As a result, the number of crossings becomes the Euler characteristic of the excursion set A, denoted by $EC(A)$. According to the definition of crossing rate, the crossing rate $\mu(\lambda_Y)$ can be obtain taking a expectation on $EC(A)$, i.e.:

$$\mu(\lambda_Y) = \mathrm{E}\left[EC(A)\right] \tag{4.12}$$

On the other hand, the Euler characteristic $EC(A)$ can be expressed as the a function of the numbers of some characteristic points. Now we define two types of characteristic points. The Tpye I points are denoted by $Y_I(x_1, x_2)$, satisfying: (1) $Y_I(x_1, x_2) = \lambda$; (2) $\partial Y_I(x_1, x_2)/\partial x_1 = 0$; (3) $\partial Y_I(x_1, x_2)/\partial x_2 > 0$; (4) $\partial^2 Y_I(x_1, x_2)/\partial x_1^2 < 0$. The Tpye II points are denoted by $Y_{II}(x_1, x_2)$, satisfying: (1)-(3) for the Tpye I points; (4) $\partial^2 Y_I(x_1, x_2)/\partial x_1^2 > 0$. In this case, the Euler characteristic $EC(A)$ can be written as the number of Type I points minus the number of Type II points, i.e.:

$$EC(A) = N(Y_I) - N(Y_{II}) \tag{4.13}$$

where $N(\cdot)$ represents the operation of getting the total number. For instance, in the configuration given by Figure 4.1 (a), as shown in Figure 4.1 (c), the Tpye I points are marked by '+' whose total number is 3; and the Tpye II points are marked by '-', whose total number 1. As a result, $EC(A) = 2$, which equals the number of crossings.

Similar to the derivation of 1-dimensional crossing rate presented in Section 2.2, by placing a 2-dimensional mesh on the unit domain and decreasing the grid size to infinitesimal, we can obtain that

$$\mathrm{E}[N(Y_I)] = -\int_0^{+\infty}\int_{-\infty}^{0} y_2 y_{11} f_{YY_1Y_2Y_{11}}(\lambda, 0, y_2, y_{11})\mathrm{d}y_{11}\mathrm{d}y_2 \tag{4.14}$$

and

$$\mathrm{E}[N(Y_{II})] = \int_0^{+\infty} \int_0^{+\infty} y_2 y_{11} f_{YY_1Y_2Y_{11}}(\lambda, 0, y_2, y_{11}) \mathrm{d}y_{11} \mathrm{d}y_2 \tag{4.15}$$

where $Y_1 = \partial Y/\partial x_1$, $Y_2 = \partial Y/\partial x_2$, $Y_{11} = \partial^2 Y/\partial x_1^2$, and $f_{YY_1Y_2Y_{11}}$ = joint PDF of Y, Y_1, Y_2 and Y_{11}. Hence, the crossing rate is obtained as

$$\mu(\lambda_Y) = \mathrm{E}[N(Y_I)] - \mathrm{E}[N(Y_{II})] = -\int_0^{+\infty} \int_{-\infty}^{+\infty} y_2 y_{11} f_{YY_1Y_2Y_{11}}(\lambda, 0, y_2, y_{11}) \mathrm{d}y_{11} \mathrm{d}y_2 \tag{4.16}$$

For an isotropic stationary Gaussian field, in the four random fields: Y, Y_1, Y_2 and Y_{11}, only Y and Y_{11} are dependent. As a result, we can write $f_{YY_1Y_2Y_{11}}(y, y_1, y_2, y_{11}) = f_{YY_{11}}(y, y_{11}) f_{Y_1}(y_1) f_{Y_2}(y_2)$, where $f_{YY_{11}}$ is the joint PDF of Y and Y_{11}, which is a bivariate Gaussian PDF; f_{Y_1} and f_{Y_2} are the marginal PDFs of Y_1 and Y_2, which are the same Gaussian PDF. Finally, the crossing rate of a 2-dimensional isotropic stationary Gaussian field is obtained as

$$\mu(\lambda_Y) = (2\pi)^{-3/2} \sqrt{\lambda_{02}\lambda_{20}} \delta_Y^{-3} \lambda \exp(-\frac{\lambda^2}{2\delta_Y^2}) \tag{4.17}$$

where δ_Y is the standard deviation of $Y(x_1, x_2)$, and λ_{ij} is the ijth spectral moment defined by

$$\lambda_{ij} = \mathrm{E}\left[\frac{\partial^i Y(x_1, x_2)}{\partial x_1^i} \frac{\partial^j Y(x_1, x_2)}{\partial x_2^j}\right] = \int_{-\infty}^{+\infty} \int_{-\infty}^{+\infty} \omega_1^i \omega_2^j S(\omega_1, \omega_2) \mathrm{d}\omega_1 \mathrm{d}\omega_2 \tag{4.18}$$

and $S(\omega_1, \omega_2)$ is power spectral density. A detailed derivation of the crossing rate of 2-dimensional Gaussian fields was provided by Alder[4, 3]. It should be pointed out that the probability of having a connected component of the excursion set protruding the boundary (shown in Figure 4.1 (d)) is neglected.

Similar to the 2-dimensional case, by treating the number of crossings as the Euler characteristic of the excursion set, the crossing rate of an $n-$dimensional Gaussian field with repective to an up-crossing barrier λ_Y can be computed by the following formula proposed by Alder [3, 5]

$$\mu_{\eta_0}(\lambda) \approx \frac{\exp(-\lambda_Y^2/2)(\det \Lambda)^{1/2}}{(2\pi)^{(n+1)/2}} H_{n-1}(\lambda_Y) \tag{4.19}$$

where Λ = the covariance matrix of the spatial gradient of the random field $Y(\mathbf{x})$, and $H_k(x)$ = the kth Hermite polynomial, which can be written as

$$H_k(x) = k! \sum_{j=0}^{k} \frac{(-1)^j x^{(k-2j)}}{j!(k-2j)!2^j} \tag{4.20}$$

In Eq. (4.19), the covariance matrix Λ can be calculated directly from the power spectral density function of $Y(\mathbf{x})$:

$$\Lambda_{ij} = \int_0^{+\infty} \cdots \int_0^{+\infty} \omega_i \omega_j G_Y(|\omega|) \mathrm{d}\omega_1 \cdots \mathrm{d}\omega_n \tag{4.21}$$

where $|\omega| = \sqrt{\omega_1^2 + \cdots + \omega_n^2}$, and $G_Y(|\omega|)$ is the one sided power spectral density function of $Y(\mathbf{x})$. For an $n-$dimensional isotropic stationary Gaussian field, $G_Y(|\omega|)$ and $R_Y(|\Delta\mathbf{x}|)$ can be further related as [2, 87, 1]:

$$G_Y(|\omega|) = \int_0^{\infty} |\omega| J_v(\eta|\omega|) R_Y(\eta) \left(\frac{2\eta}{\pi|\omega|}\right)^{n/2} \mathrm{d}\eta \tag{4.22}$$

where

$$J_v(x) = \frac{2(x/2)^{n/2-1}}{\sqrt{\pi}\Gamma(n-1)} \int_0^{\pi} \cos(x\cos\theta)(\sin\theta)^{n-2} \mathrm{d}\theta, \tag{4.23}$$

which is the Bessel function of the first kind of order $n/2-1$, and $\Gamma(x)$ = the Euler

gamma function.

With the aforementioned approach, the structural strength distribution $F_{\sigma_N}(\sigma_N, \Omega)$ in Eq. (4.6) can be calculated by

$$F_{\sigma_N}(\sigma_N, \Omega) = 1 - F_{\eta_0}\left[\lambda(\sigma_N)\right] \exp\left[-\frac{\mu_{\eta_0}(\sigma_N)}{F_{\eta_0}\left[\lambda(\sigma_N)\right]} V_\Omega\right] \tag{4.24}$$

where F_{η_0} = marginal CDF of the random field η_0. Since the random fields $Z_0(\mathbf{x})$ and $f_{t0}(\mathbf{x})$ are mutually independent, F_{η_0} can be calculated by the following equation

$$F_{\eta_0}(y) = \int_{-\infty}^{y} \int_{-\infty}^{\eta} \sigma_N^{-1} f_{Z_0}(z/\sigma_N) f_{f_{t0}}(z-\eta) \mathrm{d}z \mathrm{d}\eta \tag{4.25}$$

where $f_{Z_0}(u)$ and $f_{f_{t0}}(u)$ are the marginal PDFs of the random fields Z_0 and f_{t0}, respectively. Furthermore, the covariance function of $\eta_0(\mathbf{x})$ can be expressed as

$$R_{\eta_0}(\Delta\mathbf{x}) = \sigma_N^2 R_{Z_0}(\Delta\mathbf{x}) + R_{f_{t0}}(\Delta\mathbf{x}) \tag{4.26}$$

where $R_{Z_0}(\Delta\mathbf{x})$ and $R_{f_{t0}}(\Delta\mathbf{x})$ are the covariance functions of $Z_0(\mathbf{x})$ and $f_{t0}(\mathbf{x})$, respectively.

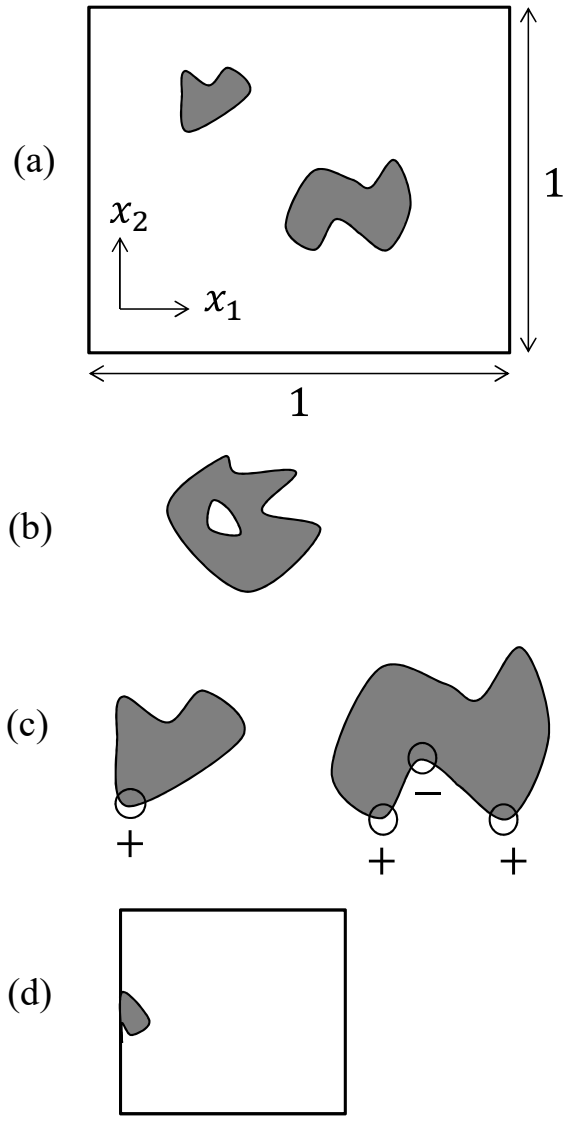

Figure 4.1: Illustration of 2-dimensional crossings: (a) an excursion set in a unit domain, (b) a connected component of the excursion set whose Euler characteristic is not one, (c) characteristic points of the excursion set, (d) a connected component of the excursion set protruding the boundary.

4.4 Model prediction and numerical verification

4.4.1 Description of analyses

In this section, the proposed model is applied to calculate the tensile strength distribution of structures in 1-dimensional, 2-dimensional and 3-dimensional settings. 2-dimensional analysis is sufficient for many practical engineering structures, where the damage can be considered to fully occupy the structure in the transverse direction (Figure 4.2 (b)). In some cases, the 2-dimensional analysis can be further simplified to a 1-dimensional analysis if the failure always initiates along a particular surface, and therefore the failure statistics can be practically calculated along a line (Figure 4.2 (a)). For instance, the failure statistics of poly-Si MEMS structures studied in Chapter 2 can be described by a 1-dimensional model [65, 101]. 3-dimensional analysis is applicable to structures of comparable dimensions in all three directions, and the volume of fracture process zone or the damage localization zone is much smaller than structural size of any of dimensions(Figure 4.2 (c)).

The model should be verified before studying the power-law tail distribution of structural strength. The validation of the present model is performed by comparing the model prediction on the structural strength distribution and the corresponding result from Monte Carlo simulations. As a result, the generalization of the strength field $f_t(\mathbf{x})$ and the dimensionless stress field $Z(\mathbf{x})$ should be obtained by Monte Carlo simulations. The Monte Carlo generalization of an $n-$dimensional random field is realized by incorporating both the $n-$dimensional spectral representation method and non-Gaussian translation method [90, 57], which ensures that the simulated fields have the prescribed marginal distribution and covariance function. Use the generalization of a non-Gaussian field $\eta_0(\mathbf{x})$ as a example. In this method, the covariance function of the corresponding standard Gaussian field, represented by R_Y, should be computed through Eq.(4.10). By using R_Y, the standard Gaussian field $Y(\mathbf{x})$ can

be generated through the $n-$dimensional spectral representation method [90]. Finally, the generalization of $\eta_0(\mathbf{x})$ can be obtained by back translating $Y(\mathbf{x})$ through Eq.(4.9).

In the generalization of the strength field $f_t(\mathbf{x})$, its marginal CDF F_{f_t} is considered to be the Gauss-Weibull grafted distribution described by Eq. (1.24a) and (1.24b). The covariance function of $f_t(\mathbf{x})$ is assumed to be the following Gaussian function

$$R_{f_t}(|\Delta\mathbf{x}|) = \delta_{f_t}^2 \exp(-|\Delta\mathbf{x}|^2/l_{f_t}^2) \tag{4.27}$$

where l_{f_t} is a length constant, and δ_{f_t} is the standard deviation of $f_t(\mathbf{x})$.

In the generalization of the dimensionless stress field $Z(\mathbf{x})$, in principle, the randomly distributed flaws should be taken into consideration. However, since the focus of this chapter is to investigate the origin of the power-law tail of structural strength distribution, while the detailed probability distribution of flaw size is not of particular importance because its influence will be manifested by the statistical properties of the random stress field. Clearly, the left tail of the structural strength distribution is governed by the left tail of the material strength distribution and the right tail of the stress distribution. From a series of recent studies on probabilistic fracture, the left tail behavior of the material strength distribution can be described by the aforementioned Gauss-Weibull grafted distribution, which contains a left power-law tail [81, 67]. However, the probability distribution of the stress field remains unclear, which does not necessarily contains a right power-tail. In order to investigate the influence of the tail behaviors of $f_t(\mathbf{x})$ and $Z(\mathbf{x})$ on the structural strength statistics, we consider two types of probability distribution functions of the dimensionless stress field $Z(\mathbf{x})$, i.e., a Weibull-type distribution and a Gaussian distribution:

$$F_{ZW}(z) = \exp\left\{-[(z_{max} - z)/s_z]^{m_z}\right\} \qquad (z \leq z_0) \tag{4.28}$$

$$F_{ZG}(z) = \frac{1}{\sqrt{2\pi}\delta_z} \int_{-\infty}^{z} e^{-(z'-\mu_z)^2/\delta_z^2} \mathrm{d}z' \tag{4.29}$$

where z_{max} = maximum value of z. For the right tail, the CDF of the Weibull-type distribution decays as $(z_0 - z)^m$, while the CDF of Gaussian distribution has a exponential decay. Similar to the strength field, for both cases of different distribution functions, the covariance function of $Z(\mathbf{x})$ is considered as a Gaussian function, i.e.:

$$R_Z(|\Delta\mathbf{x}|) = \delta_z \exp(|\Delta\mathbf{x}|^2/l_z^2) \tag{4.30}$$

where δ_z = standard deviation of $Z(\mathbf{x})$, and l_z = a length constant. In the subsequent discussion, we denote the dimensionless stress fields with distribution functions F_{ZW} and F_{ZG} as $Z_W(\mathbf{x})$ and $Z_G(\mathbf{x})$, respectively.

In the present analysis, the following parameters are used to describe the marginal CDFs of $f_t(\mathbf{x})$ and $Z(\mathbf{x})$: $m_W = 24$, $s_W = 15$ MPa, $\mu_G = 20$ MPa, $\delta_G = 4$ MPa, $l_{f_t} = 10$ μm, $z_{max} = 7$, $m_z = 5.2$, $s_z = 12$, $\mu_z = 2$, $\delta_z = 0.4$, and $l_z = 50$ μm. After the strength field $f_t(\mathbf{x})$ and the dimensionless stress field $Z(\mathbf{x})$ are generated through the aforementioned simulation method, the random field $\eta_0(\mathbf{x})$ and the structural strength distribution F_{σ_N} can be numerically computed through Eqs. (4.5a)- (4.7). These numerical results of structural strength distribution is further compared to the corresponding analytical model predictions, from which the present model can be verified. For 1-dimensional and 2-dimensional cases, direct stochastic simulations are performed to verify the proposed analytical model. For the direct Monte Carlo simulations, we first generate the strength field $f_t(\mathbf{x})$ and the dimensionless stress field ($Z_W(\mathbf{x})$ or $Z_G(\mathbf{x})$) by the combination of spectral representation method and non-Gaussian translation method. For 3-dimensional cases, since the Monte Carlo simulation is computational expensive, we only calculate the model predictions.

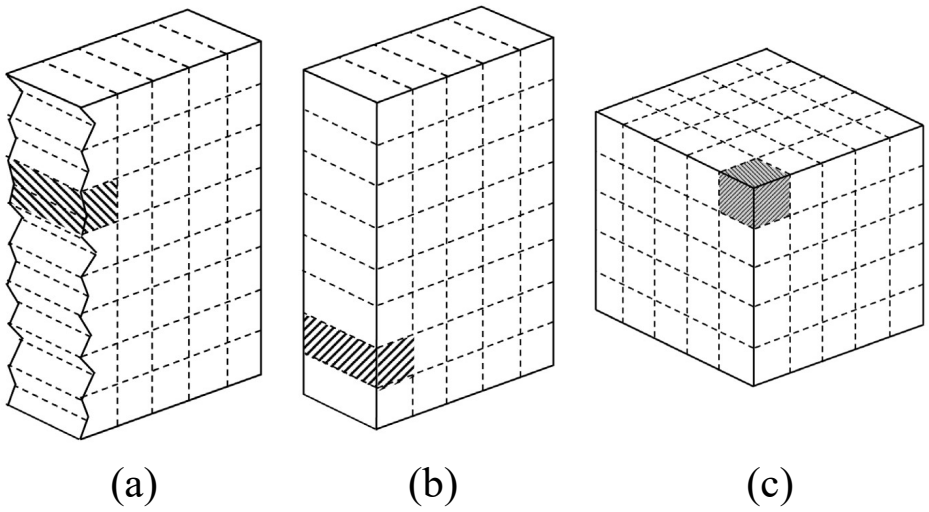

Figure 4.2: Different model representations of failure statistics of the structure: (a) 1-dimensional analysis, (b) 2-dimensional analysis, and (c) 3-dimensional analysis.

4.4.2 Results of 1-dimensional analysis

The aforementioned analysis is applied to a 1-dimensional case, where the structural size is 10^5 μm. Figure 4.3 (a) and Figure 4.4 (a) show typical realizations of the random fields $\eta_0(\mathbf{x})$ with respect to $Z_W(\mathbf{x})$ and $Z_G(\mathbf{x})$, respectively, in which $\sigma_N = 3$ MPa. Based on the generated random fields, the marginal CDF and the covariance function of the random field $\eta_0(\mathbf{x})$ were obtained numerically and compared with those predicted by Eqs. (4.24) and (4.25). From Figure 4.3 (b)-(c) and Figure 4.3 (b)-(c), it is seen that the numerical marginal CDFs and the covariance functions well match the corresponding analytical solutions, which verifies the proposed method for generating the random fields is valid.

In order to determine the CDF of structural strength, all together 1000 realizations of $\eta_0(\mathbf{x})$ are generated for each given value of σ_N, and the corresponding structural strength distribution is computed. The plot of simulated CDF of structural strength in Weibull scale is shown as circles in Figure 4.5. On the other hand, the strength distribution is also calculated analytically by using the present first-passage analysis (Eq. (4.24)), which is plotted as solid lines in Figure 4.5. It is seen that, for both types of stress fields, the model predictions well match the corresponding simulation results. It is noted that the CDF of the structural strength always exhibit a power-law tail for both cases of different distributions of the dimensionless stress field, which is manifested as a straight line on the Weibull scale. Moreover, it shows that the exponent of the power-law tail is bounded between 23 and 24 for both stress fields (about 23.5 for both cases), which is slightly lower than the Weibull modulus of the material strength CDF F_{f_t}. This result implies that distribution of the stress field does not alter the power-law nature of the tail distribution of structural strength.

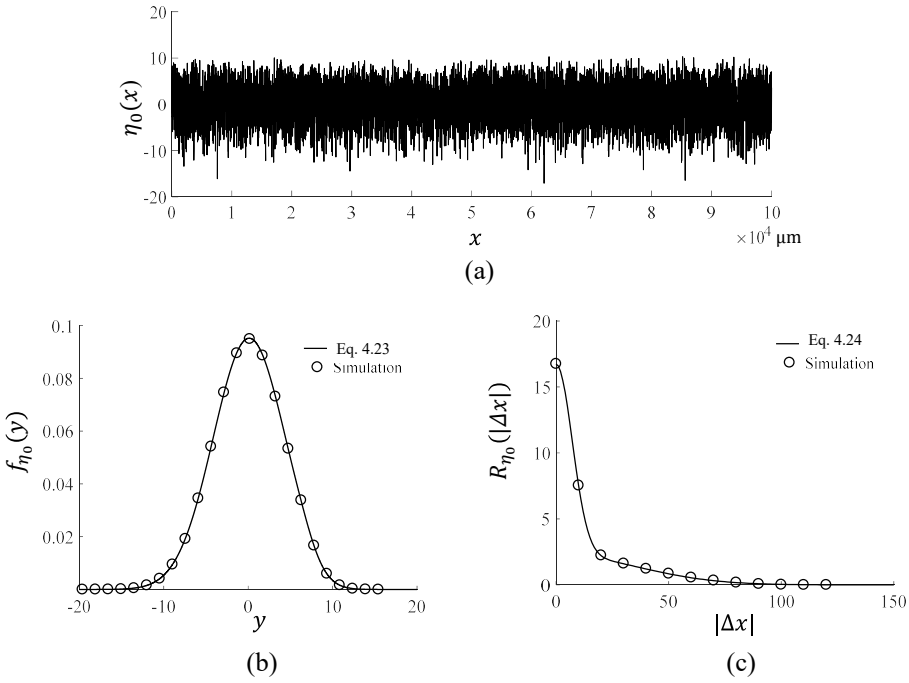

Figure 4.3: Numerical simulations of the random field $\eta_0(x)$ in 1-dimensional with a Weibull type stress field $Z_W(x)$: (a) a typical realization of $\eta_0(x)$, (b) calculated marginal CDF, and (c) calculated covariance function.

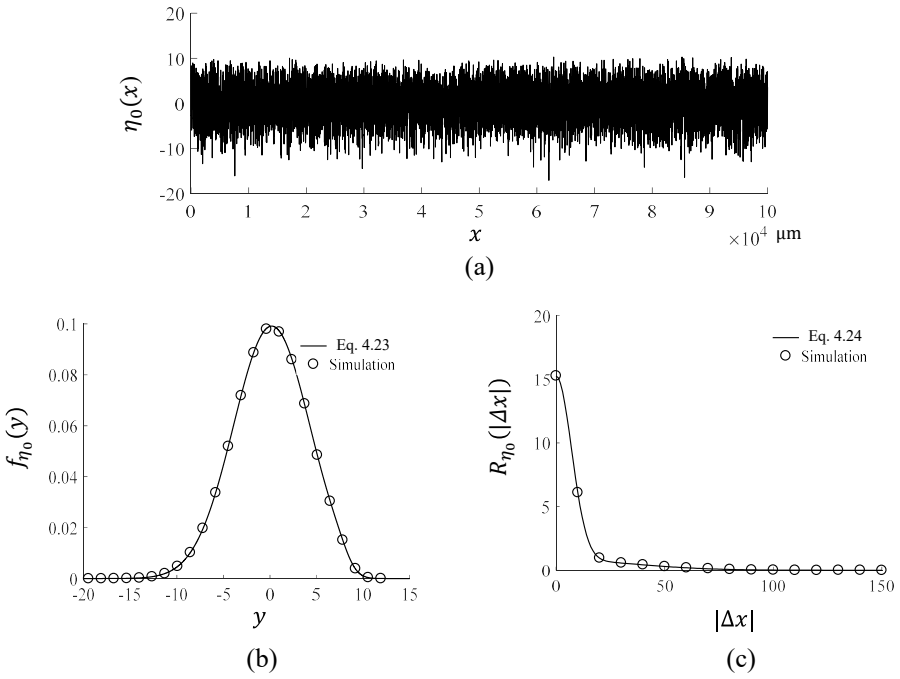

Figure 4.4: Numerical simulations of the random field $\eta_0(x)$ in 1-dimensional with a Weibull type stress field $Z_G(x)$: (a) a typical realization of $\eta_0(x)$, (b) calculated marginal CDF, and (c) calculated covariance function.

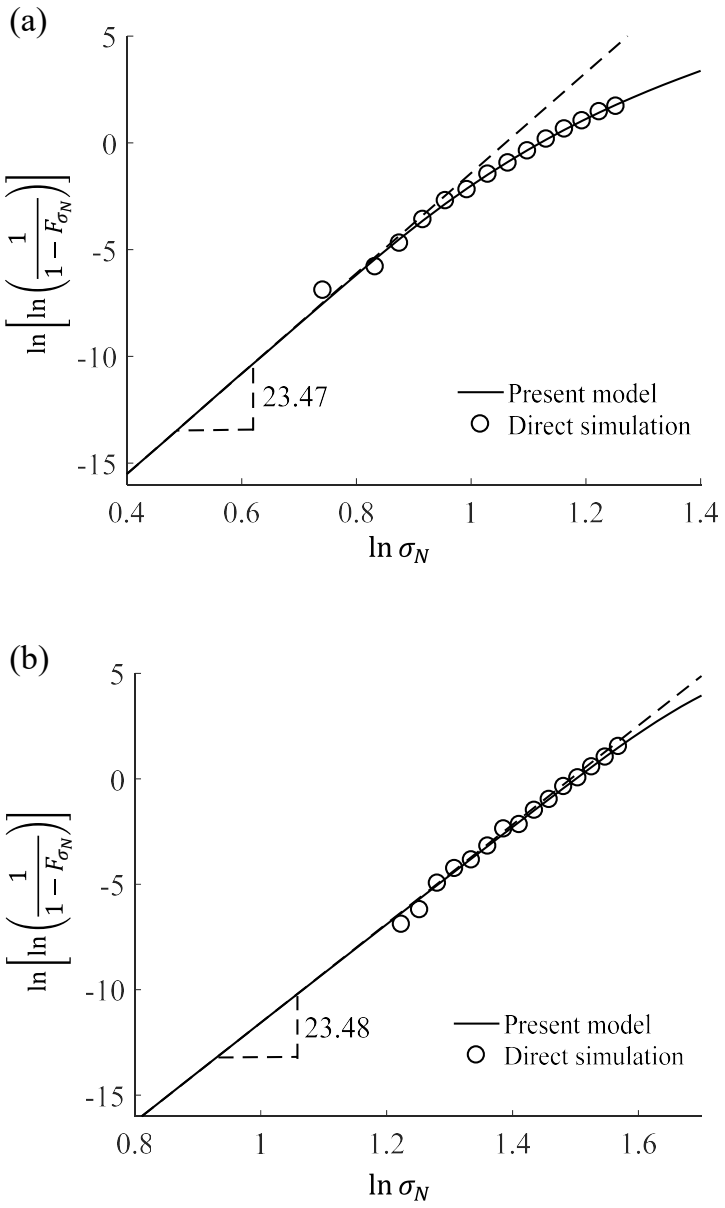

Figure 4.5: Comparison between the predicted and the numerically simulated CDFs of structural strength in 1-dimensional: (a) with a Weibull type stress field $Z_W(x)$, and (b) with a Gaussian stress field $Z_G(x)$.

4.4.3 Results of 2-dimensional and 3-dimensional analyses

Similar analysis of the 1-dimensional case is applied to the 2-dimensional and 3-dimensional cases. In the 2-dimensional analysis, we considers a square structure domain of a size of 2000×2000 μm^2. While the 3-dimensional analysis considers a cubic structure domain of a size of $1000 \times 1000 \times 1000$ μm^3. The analytical result of the 2-dimensional analysis is verified through the comparison with the Monte Carlo simulation. However, for 3-dimensional case, since the Monte Carlo simulation is computational expensive, we only show the analytical model prediction.

Figure 4.6 presents a typical realization of the 2-dimensional strength field $f_t(\mathbf{x})$ and stress fields ($Z_W(\mathbf{x})$ and $Z_G(\mathbf{x})$). The realization of the random field $\eta_0(\mathbf{x})$ is then computed through Eq. (4.7). Figure 4.7 shows a typical realization of $\eta_0(\mathbf{x})$ for $\sigma_N = 3$ MPa, as well as the marginal CDF and the covariance function in three directions. It is seen that, for all the three directions, the calculated marginal CDF and covariance function are identical, which demonstrates the isotropy of $\eta(\mathbf{x})$. Moreover, they all agree well with the analytical solutions by Eqs. (4.25) and (4.26).

Figure 4.8 shows the comparison of the strength CDFs of the 2-dimensional case plotted in Weibull scale that predicted by the proposed model and the corresponding Monte Carlo simulation results. It is clear that the predictions of the analytical model agrees well with the Monte Carlo simulation results. In this case, we observe that, for both random stress fields, the left tail of the structural strength distribution is also a power-law function, whose exponent is bounded between 22 to 23, (about 22.5 and 22.1 for stress fields $Z_W(\mathbf{x})$ and $Z_G(\mathbf{x})$, respectively). These calculated exponents are slightly lower than those of the 1-dimensional analysis. To further examine the power-law tail distribution of structural strength, we calculate the strength distribution of the 3-dimensional case by using the analytical model, which is shown in Figure 4.9. In the 3-dimensional case, the left tail of the strength distribution still preserves the power-law behavior regardless of the type of random stress field. Nevertheless, the

power-law exponent is reduced to around 21.8 and 21.1 for the stress fields $Z_W(\mathbf{x})$ and $Z_G(\mathbf{x})$, respectively. The exponent of the structural strength distribution of the 3-dimensional case seems to be bounded between 21 and 22.

4.4.4 Comments on the power-law tail behavior

Based on the results of the 1-dimensional, the 2-dimensional and the 3-dimensional analyses, we may conclude that: regardless of different marginal distributions of the random stress field, the structural strength distribution always exhibits a power-law tail. This suggests that the origin of the power-law tail of structural strength distribution is the left power-law tail of the material strength distribution. Furthermore, it also appears that the exponent of this power-law tail decreases with the dimensionality of the analysis. It is suggested that the exponent of the power-law tail of structural strength distribution is bounded between $m_W - n$ an $m_W - n + 1$, where m_W is the exponent of the left power-law tail of material strength CDF and n is the dimensionality of the analysis.

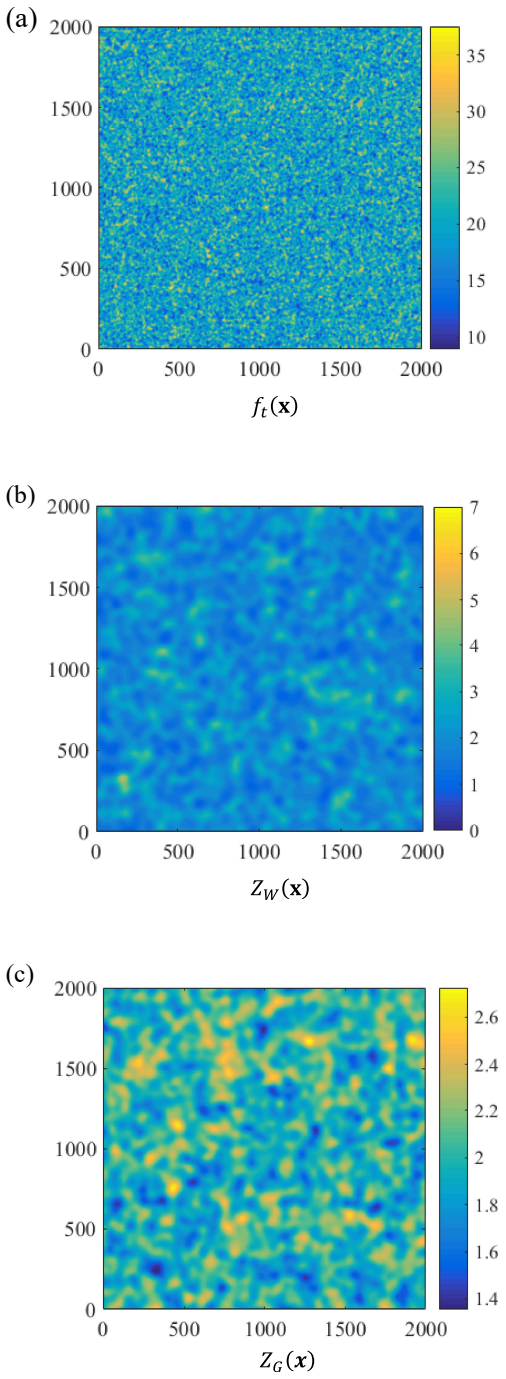

Figure 4.6: Typical realizations of the random fields in 2-dimensional: (a) random strength field $f_t(\mathbf{x})$, (b) Weibull type stress field $Z_w(\mathbf{x})$, and (c) Gaussian stress field $Z_G(\mathbf{x})$.

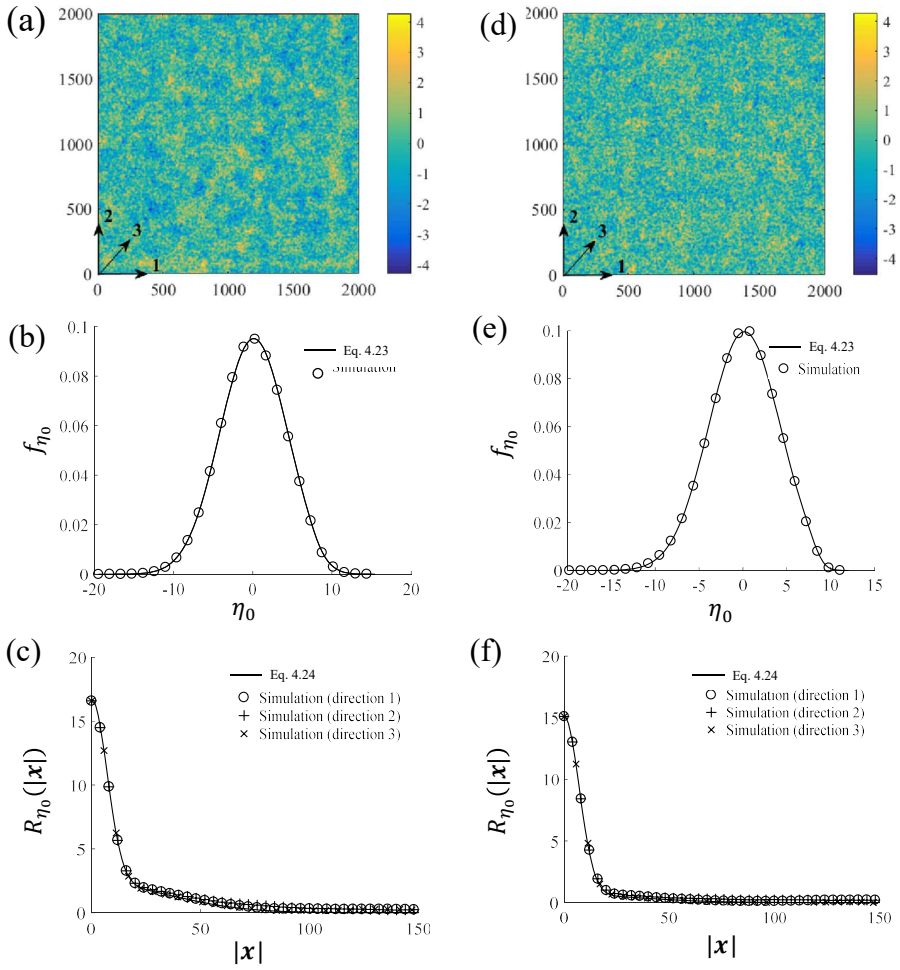

Figure 4.7: Numerical simulation of the random field $\eta_0(\mathbf{x})$ in 2-dimensional: (a) a typical realization of $\eta_0(\mathbf{x})$ by using $Z_W(\mathbf{x})$, (b) marginal PDF of $\eta_0(\mathbf{x})$ by using $Z_w(\mathbf{x})$, (c) calculated covariance function of $\eta_0(\mathbf{x})$ by using $Z_w(\mathbf{x})$, (d) a typical realization of $\eta_0(\mathbf{x})$ by using $Z_G(\mathbf{x})$, (e) marginal PDF of $\eta_0(\mathbf{x})$ by using $Z_G(\mathbf{x})$, (f) calculated covariance function of $\eta_0(\mathbf{x})$ by using $Z_G(\mathbf{x})$.

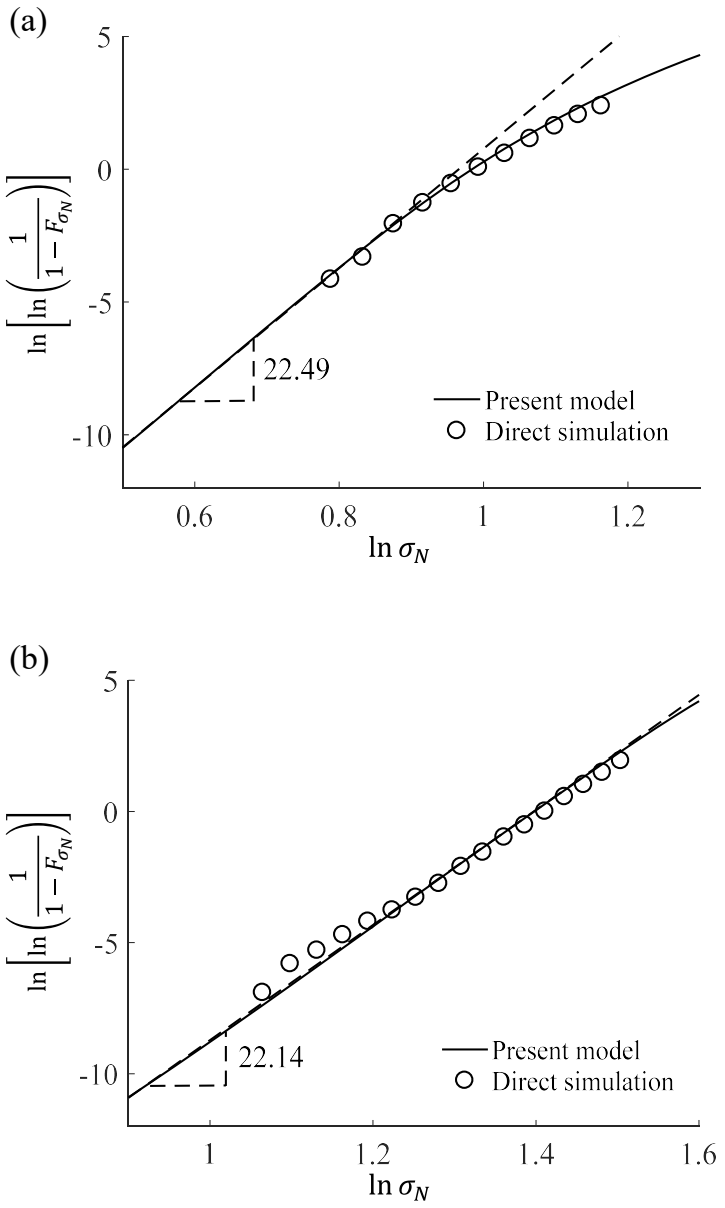

Figure 4.8: Comparison between the predicted and the numerically simulated CDFs of structural strength in 2-dimensional: (a) with a Weibull type stress field $Z_W(\mathbf{x})$, and (b) with a Gaussian stress field $Z_G(\mathbf{x})$.

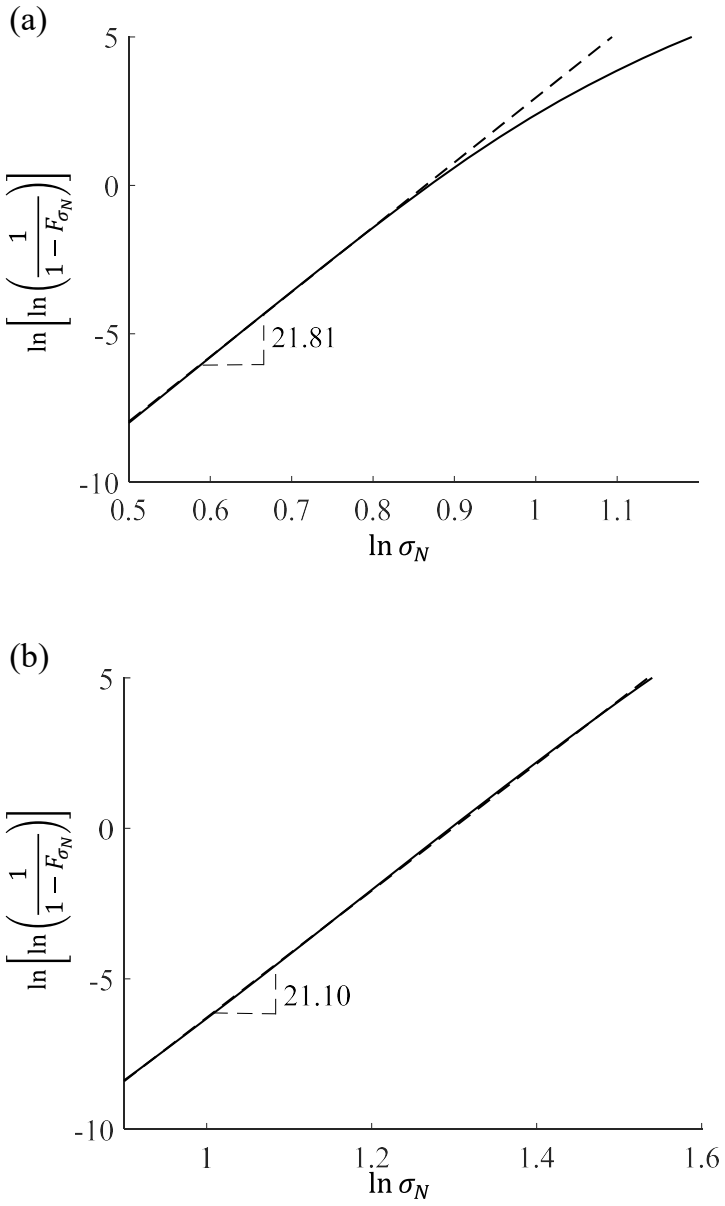

Figure 4.9: Predicted CDF of structural strength in 3-dimensional: (a) with a Weibull type stress field $Z_W(\mathbf{x})$, and (b) with a Gaussian stress field $Z_G(\mathbf{x})$.

4.5 Discussion on the power-law tail behavior

In this section, the power-law nature of structural strength distribution is discussed via the $n-$dimensional first-passage model. From Eq. (4.6), it is clear that a low value of nominal stress σ_N corresponds to a high crossing barrier, and consequently a low crossing rate. As a result, as $\sigma_N \to 0$, Eq. (4.24) can be rewritten as

$$F_{\sigma_N}(\sigma_N, \Omega) \approx 1 - F_{\eta_0}\left[\lambda(\sigma_N)\right] + \mu_{\eta_0}(\sigma_N) V_\Omega \tag{4.31}$$

Noticing that $F_{\eta_0}\left[\lambda(\sigma_N)\right]$ represents the probability that $\sigma_N Z \leq f_t$, i.e.:

$$F_{\eta_0}\left[\lambda(\sigma_N)\right] = 1 - \Pr(f_t/Z \leq \sigma_N) = 1 - \int_0^\infty F_{f_t}(z\sigma_N) f_z(z) \mathrm{d}z \tag{4.32}$$

Generally speaking, the maximum value of the dimensionless stress is finite. Therefore, we may replace the upper integration limit by a finite value z_{max}. Based on the Gauss-Weibull grafted distribution of tensile strength (Eqs. (1.24a) and (1.24b)), it is obvious that, when σ_N is sufficiently small, the CDF of f_t can be replaced by a power-law function, which yields

$$F_{\eta_0}\left[\lambda(\sigma_N)\right] \approx 1 - \int_0^{z_{max}} (z\sigma_N/s_W)^{m_W} f_z(z) \mathrm{d}z = 1 - (\sigma_N/c_1)^{m_W} \tag{4.33}$$

where $c_1 = \left[\int_0^{z_{max}} (z/s_W)^{m_W} f_z(z) \mathrm{d}z\right]^{-1/m_W}$.
Substituting Eq. (4.33) into Eq. (4.31) yields

$$F_{\sigma_N}(\sigma_N, \Omega) \approx (\sigma_N/c_1)^{m_W} + \mu_{\eta_0}(\sigma_N) V_\Omega \tag{4.34}$$

The crossing rate $\mu_{\eta_0}(\sigma_N)$ is given by Eq. (4.19), in which a closed-form expression in terms of σ_N seems to be impossible. As a result, we study the relationship between $\mu_{\eta_0}(\sigma_N)$ and σ_N numerically. Figure 4.10 presents the numerically calculated μ_{η_0} as a

function of σ_N for all the cases on the logarithmic scale. It is seen that, for a small σ_N, μ_{η_0} can be expressed by a power-law function of σ_N of an exponent m_1. Therefore, Eq. (4.34) can be rewritten as

$$F_{\sigma_N}(\sigma_N, \Omega) \approx (\sigma_N/c_1)^{m_W} + (\sigma_N/c_2)^{m_1}(V_\Omega/l_p^n) \tag{4.35}$$

$$= \sigma_N^{m_1}\left(\frac{V_\Omega}{l_p^n c_2^{m_1}} + \frac{\sigma_N^{m_W-m_1}}{c_2^{m_W}}\right) \tag{4.36}$$

where l_p = a constant length introduced for the purpose of dimensional consistency. Based on Eq. (4.36), it can be concluded that, for a finite-size domain ($V_\Omega \neq 0$), the strength distribution exhibits a power-law tail with an exponent m_1. As the structure domain becomes sufficiently large, the failure probability of the structure is governed by small values of σ_N. In such a case, the power-law behavior of $F_{\sigma_N}(\sigma_N, \Omega)$ for small values of σ_N indicates that the strength distribution should approach the Weibull distribution, i.e.:

$$F_{\sigma_N}(\sigma_N, \Omega) = 1 - \exp\left[-\frac{V_\Omega}{l_p^n}\left(\frac{\sigma_N}{c_2}\right)^{m_1}\right] \quad \text{when } V_\Omega \text{ is very large} \tag{4.37}$$

Based on Figure 4.10, it is observed that, for given stress fields and strength fields, the exponent m_1 decreases mildly with the dimensionality of the analysis. Based on the simulation results, this exponent can be written as $m_1 \approx m_W - n + k$, where parameter k depends on the stress field. Nevertheless, many engineering materials, such as concretes and ceramics, have a relatively large Weibull modulus of material tensile strength (m_W is in the range of 20-40), and therefore the effect of the dimensionality on the exponent of the power-law tail of structural strength distribution is not of significant importance, which may not be discerned by experiments because the sample size is usually limited.

If we consider that the size of the structure domain drop down to zero, the strength

distribution will become the complimentary CDF of $F_{\eta_0}(\lambda)$, leading to a power-law tail with an exponent m_W. In this limiting case, the dimensionality of the analysis becomes unimportant since the domain shrinks to a point. On contrast, for the large size limit, the structural strength statistics will be primary governed by the crossing rate and the size of the structural domain, while the influence of the term $F_{\eta_0}(\lambda)$ becomes negligible.

The key finding of the analysis of this chapter is that the power-law tail behavior of the structural strength distribution is primarily governed by the left power tail of the material strength distribution. The exponent of the power tail is mainly determined by the Weibull modulus of the material strength distribution, which also is mildly affected by the dimensionality of the analysis and by the randomness of the stress field. As mentioned earlier, recent studies on statistics of material strength [23, 18, 67, 17] showed that the power-law tail of material strength distribution stems from the thermally activated random jumps of the nano-crack tip, which can be mathematically described by the transition rate theory. Therefore, we may conclude that the power-law tail distribution of structural strength is a consequence of the mechanics of thermally activated behavior of nanocracks. By contrast, the flaw statistics surely influences the overall failure statistics of structures, but does not dictate the power-law behavior of the tail distribution of structural strength.

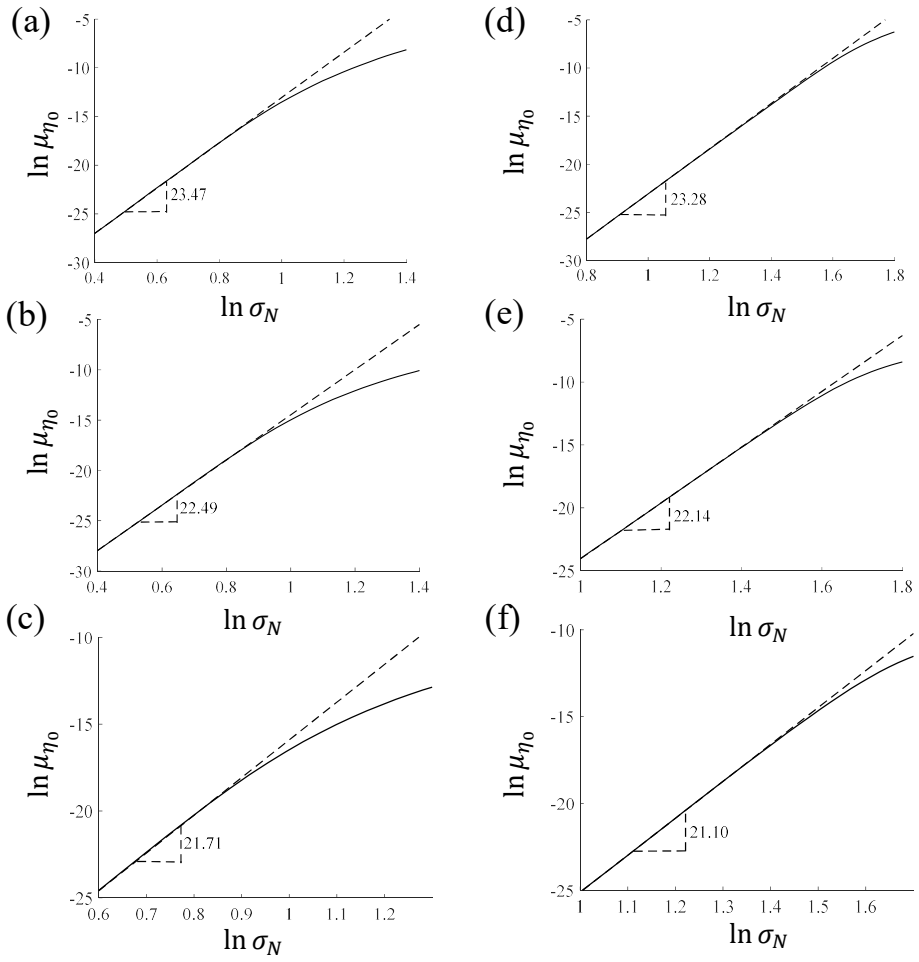

Figure 4.10: Simulated relationship between the crossing rate and the applied nominal stress: (a) 1-dimensional analysis by using $Z_W(\mathbf{x})$, (b) 2-dimensional analysis by using $Z_W(\mathbf{x})$, (c) 3-dimensional analysis by using $Z_W(\mathbf{x})$, (d) 1-dimensional analysis by using $Z_G(\mathbf{x})$, (e) 2-dimensional analysis by using $Z_G(\mathbf{x})$, and (f) 3-dimensional analysis by using $Z_G(\mathbf{x})$.

4.6 Conclusions

In this Chapter, the first-passage model is generalized to $n-$dimensional for the strength statistics of brittle and quasi-brittle structures. The origin of power-law tail of strength distribution of brittle and quasi-brittle structures is investigated by extending the first-passage model to higher dimensions. For 1-dimensional and 2-dimensional analyses, the predictions of the proposed model are verified by the corresponding Monte Carlo simulation results.

The result of the present analysis shows that, the distribution of structural strength always exhibits a power-law tail behavior regardless of the types of the random stress field. This suggests the distribution of the flaw sizes does not dictate the power-law behavior of structural strength distribution.

The exponent of the power-law tail of structural strength distribution is primarily governed by the Weibull modulus of the distribution of material strength, which is also mildly affected by the dimensionality of the analysis and the randomness of the stress field. This indicates that the origin of the power-law tail behavior of the structural strength distribution is the power-law tail of material strength distribution, which stems from the thermally activated motion of the nano-crack tip govern by the transition rate theory.

Chapter 5

Internal Length Scale of Finite Weakest-Link Model for Quasi-Brittle Fracture

5.1 Introduction

As discussed in Section 1.3, the finite weakest-link model is able to provide optimum fitting of measured strength distributions of different types of quasi-brittle structures [81, 66, 67, 68, 17]. Despite the successful applications of the finite weakest-link model, the representative volume element (RVE), as the core of the model, remains a mathematical concept, whose physical interpretation has not been fully understood. In Section 2.6, we suggested that the RVE size should be related to the autocorrelation length of the random field that governs material failure. However, the RVE size is usually determined by optimum fitting of the measured strength distribution, whose relationship with material properties is still under development. Furthermore, the experimental strength histogram testing is usually performed on a single specimen geometry. Therefore, it is unclear whether the RVE size is truly a material property, or a structural property that is influenced by the loading configuration. Exploring the relationship between the RVE size and material properties is an essential step to

advance our understanding of the weakest-link model.

In this chapter, we study the RVE size by matching the size effect curves of the mean structural strength predicted by the finite weakest-link model and by non-linear stochastic finite element simulations. The relationship among the RVE size and two essential material length scales, namely the Irwin characteristic length and the crack band width, is obtained. We first determine the functional form of RVE size as a function of both the Irwin characteristic length and the crack band width through dimensional analysis. The model parameters are calculated through matching the size effect curves of the finite weakest-link model and the stochastic simulations. For this purpose, it suffices to consider the size effect curve of the mean structural strength over the small and intermediate size range. Three different loading configurations are studied (uniaxial tension, pure bending and three-point-bending) to investigate the influence of structural geometry on the RVE size.

This chapter is planed as the following manner: Section 5.2 presents the stochastic finite element modeling approach as well as a dimensional analysis on the relationship among the RVE size, the Irwin characteristic length and the crack band width; Section 5.3 presents the details for the stochastic finite element simulations that aimed to obtain the size effect curves of the mean structural strength; Section 5.4 discusses the relationship between RVE size and the two material length sales.

5.2 Modeling approach and dimensional analysis

From the discussion in Section 1.3, it is clear that the finite weakest-link model predicts an intricate size effect on the mean structural strength. From Eq. (1.25), the size effect curve of the mean structural strength can be decribed by a dimensionless paramter D/l_0, where D is the characteristic structural size and l_0 is the RVE size. On the other hand, recent researches show that the size effect curve of the mean

structural strength predicted by the non-linear material models can be expressed by another dimensionless number D/l_c, where l_c = a material characteristic length scale [23, 67, 69, 17]. Therefore, it is expected that the RVE size l_0 must be related to the length scale l_c by matching the mean size effect curves. As will be discussed later, l_c is governed by two basic material length scales, which are the Irwin characteristic length [28] and the crack band width [27]. This section presents a dimensional analysis, which leads to a mathematical relationship among the RVE size, the Irwin characteristic length and the crack band width.

In the analysis of this chapter, the benchmark solution of the size effect curve of the mean structural strength is obtained from a series of stochastic finite element simulations, which employs a non-linear material constitutive law based on the isotropic damage model, together with a spatially random distribution of material properties. Since our attention is limited to the cases of tensile damage, the simplest constitutive model of this kind is applied, which contains the following material parameters: Young's modulus E, Poisson's ratio ν, tensile strength f_t, and fracture energy G_f. Obviously, the Irwin characteristic length can be expressed as $l_{ch} = EG_f/f_t^2$, which is considered as a measure of the size of the fracture process zone [24]. In addition, the other important material length scale is the crack band width l_w, which is approximately equal to two to three times the size of material inhomogeneity [15]. A recent study showed that, in stochastic finite element simulations, the ratio of the element size to the crack band width plays an important role in the determination of the distribution of the material's tensile strength for each Gauss point [70]. In the later numerical analysis, the element width is set to be equal to the crack band width so that a fixed CDF of material strength can be applied.

It has been demonstrated that the strength of the structure is directly governed by the tensile strength and the fracture energy[24, 15, 55, 70]. However, the relationship and the statistical dependency between the tensile strength and the fracture energy

remains unclear. Commonly speaking, a higher tensile strength corresponds to a higher fracture energy. Here the random tensile strength and the random fracture energy are considered to be fully correlated, whose relationship can be described by the following expression:

$$f_t(\mathbf{x}) = \eta(\mathbf{x})\bar{f}_{\mathrm{t}} \qquad G_f(\mathbf{x}) = [\eta(\mathbf{x})]^2\bar{G}_f \tag{5.1}$$

where $\bar{f}_{\mathrm{t}}$ and $\bar{G}_f$ are the input material tensile strength and fracture energy, respectively; $\eta(\mathbf{x})$ = a random variable whose mean is 1. Eq. (5.1) indicates that the Irwin characteristic length l_{ch} remains a constant for any combination of f_t and G_f, i.e.:

$$l_{ch}(\mathbf{x}) = \frac{EG_f}{f_t^2} = \frac{E\eta^2\bar{G}_f}{\eta^2\bar{f}_{\mathrm{t}}^2} = \frac{E\bar{G}_f}{\bar{f}_{\mathrm{t}}^2} \tag{5.2}$$

Obviously, the mean of f_t is just $\bar{f}_{\mathrm{t}}$. It is noted that, in the present setting, the mean value of G_f is related to the input fracture energy $\bar{G}_f$ by the following equation

$$\mathrm{E}[G_f] = \mathrm{E}[\eta^2\bar{G}_f] = \mathrm{E}[\eta^2]\bar{G}_f = \left(1+\omega_0^2\right)\bar{G}_f = c\bar{G}_f \tag{5.3}$$

where ω_0 = coefficient of variation (CoV) of η, and $c = 1+\omega_0^2$. Correspondingly, the CoV of G_f is then equal to $\sqrt{\mathrm{E}[\eta^4]/c^2 - 1}$.

In principle, $\eta(\mathbf{x})$ exhibits certain sptially autocorrelated features over the structure domain. However, the physical determination of the autocorrelated features of material strength still remains a challenge[55, 44]. Since this chapter focuses on the qualitative relationship between the RVE size and some basic material properties, it is assumed that the autocorrelation length of $\eta(\mathbf{x})$ is smaller than the finite element size so that the η value for each element can be regarded as statistically independent.

Following the aforementioned stochastic finite element model, the mean structural

strength can be expressed as

$$\bar{\sigma}_N = \Pi_0(D, l_{ch}, l_w, \bar{f}_\mathrm{t}, \omega_0) \tag{5.4}$$

We further consider that there exists a single length scale l_c governs the mean strength:

$$\bar{\sigma}_N = \Pi_1(D, l_c, \bar{f}_\mathrm{t}, \omega_0) \tag{5.5}$$

From dimensional analysis, it is obvious that l_c only depends on l_{ch}, l_w and ω_0. Using the Buckingham-Π theorem [31, 32], we can obtain that

$$\ell_c = F(\ell_{ch}, \omega_0) \tag{5.6}$$

where $\ell_c = l_c/l_w$ and $\ell_{ch} = l_{ch}/l_w$. It may be considered that ℓ_{ch} exhibits an incomplete self-similarity behavior with a power-law asymptotics [10], which leads to

$$\ell_c = \quad \ell_{ch}^{\alpha} f(\omega_0) \tag{5.7}$$

$$\text{or:} \quad l_c = \quad l_{ch}^{\alpha} l_w^{1-\alpha} f(\omega_0) \tag{5.8}$$

where the exponent α generally depends on ω_0. Because l_c should be a monotonic increasing function of both l_{ch} and l_w, α must range from 0 to 1. With Eq. (5.8), Eq. (5.5) can be rewritten in a dimensionless form:

$$\varsigma_N = \phi_1(d, \omega_0) \tag{5.9}$$

where $\varsigma_N = \bar{\sigma}_N/\bar{f}_\mathrm{t}$ and $d = D/l_c$.

Now consider the mean structural strength yielded by the finite weakest-link

model. From Eqs. (1.24a), (1.24b) and (1.25), the mean structural strength can be written as

$$\bar{\sigma}_N = \Pi_2(D, l_0, \mu_G, \delta_G, m_W, s_w) \tag{5.10}$$

Since our interesting is limited to the mean strength of structures of small sizes, it suffices to approximate the strength distribution of the RVE described by Eqs. (1.24a) and (1.24b), by a Gaussian distribution. Because the Weibull portion is too small to influence the mean structural strength. As a result, for small-size range, Eq. (5.10) can be written as

$$\bar{\sigma}_N = \Pi_3(D, l_0, \mu_G, \delta_G) \tag{5.11}$$

Furthermore, the mean strength of RVE can be considered to be equal to the mean tensile strength $\bar{f}_{\mathrm{t}}$, and the standard deviation δ_G of the Gaussian core can replaced by the CoV of the Gaussian core $\omega_G = \delta_G/\mu_G$. The dimensionless form of Eq. (5.11) can then be written as

$$\varsigma_N = \phi_2(d_l, \omega_G) = \phi_2(d/\ell_0, \omega_G) \tag{5.12}$$

where $d_l = D/l_0$, and $\ell_0 = l_0/l_c$. ℓ_0 can be considered as the normalized RVE size.

Now we match the size effect curves of the mean structural strength predicted by the non-linear stochastic simulations and that of the finite weakest-link model over a range of small and intermediate specimen sizes. Consider the non-linear random model as a benchmark solution for a size range $d \in [d_1, d_2]$, where $d_1 = D_1/l_c$ and $d_2 = D_2/l_c$. The normalized RVE size ℓ_0 and CoV ω_G of RVE strength can be

obtained by minimizing the difference of these two size effect curves, i.e.

$$H(\ell_0, \omega_G) = \int_{d_1}^{d_2} \left[\phi_1(d, \omega_0) - \phi_2(d/\ell_0, \omega_G)\right]^2 \mathrm{d}d \tag{5.13}$$

$$\frac{\partial H}{\partial \ell_0} = \Phi_1(d_1, d_2, \ell_0, \omega_0, \omega_G) = 0 \tag{5.14}$$

$$\frac{\partial H}{\partial \omega_G} = \Phi_2(d_1, d_2, \ell_0, \omega_0, \omega_G) = 0 \tag{5.15}$$

Given a set of d_1 and d_2, Eqs. (5.14) and (5.15) lead to the solutions of ℓ_0 and ω_G

$$\ell_0 = g(\omega_0) \tag{5.16a}$$

$$\omega_G = h(\omega_0) \tag{5.16b}$$

By substituting Eq. (5.8) into Eq. (5.16a) and rewriting it in the dimensional form, it is obtained that

$$l_0 = l_{ch}^{\alpha} l_w^{1-\alpha} F(\omega_0) \tag{5.17}$$

where $F(\omega_0) = f(\omega_0)g(\omega_0)$. Eq. (5.17) indicates that the RVE size depends on both the Irwin characteristic length l_{ch} and the crack band width l_w. It is noted that the relative dominance of these length scales could depend on the CoV of material strength, as well as on the structure geometry, which will be discussed in Section 5.4.

5.3 Stochastic computation of size effect on the mean structural strength

By using the aforementioned approach, the size effect curves of the mean structural strength for rectangular specimens of depth = D and length = $6D$ were calculated. Three loading configurations are considered: 1) uniaxial tension, 2) pure bending, and 3) three-point-bending (shown in Figure 5.1). For each case, a displacement controlled load is applied. For uniaxial tensile specimens, the horizontal movement of one end is restrained while the other end is uniformly displaced horizontally by u (Figure 5.1 (a)). For pure bending specimens, one side of the specimen is displaced in horizontal direction by $-\varphi y$, where y is vertical distance from the central axis of the cross-section (Figure 5.1 (b)), whereas the other end is fixed. The three-point-bending specimen is loaded by a mid-span displacement u on the top surface (Figure 5.1 (c)). For each loading configuration, a range of different specimen sizes is considered, which is: $D =$ 150, 300, 450, 600, 900, 1200 mm. Four-node isoparametric elements with a linear approximation of the deformation field is used. The element depth is set to be 1/30 of the beam depth, while various values of the width ($l_w = 25$, 30, 45, 50, 75, 90 mm) are considered to represent different crack band widths. The material has a Young's modulus of $E = 30$ GPa, Poisson's ratio $\nu = 0.2$, and mean tensile strength $\bar{f}_{\mathrm{t}} = 3$ MPa. Two values of the mean fracture energy ($\bar{G}_f = 100$ and 50 N/m) are considered , which leads to two different values of the Irwin characteristic length: $l_{ch} = 333.33$ mm and 166.67 mm. A simple isotropic damage model is applied to the stochastic finite element simulations, i.e.:

$$\sigma = (1 - \omega)\mathbf{D}\epsilon \tag{5.18}$$

where σ = stress tensor;,ϵ = strain tensor; $\mathbf{D}$ = elastic stiffness matrix; ω = damage parameter that ranges from 0 (intact) to 1 (completely damaged). The damage evolution law is expressed in terms of the equivalent strain [77]:

$$\varepsilon_{eq} = \sqrt{\sum_{i=1}^{3} \varepsilon_i^2} \tag{5.19}$$

where ε_i $(i = 1, 2, 3)$ are the principal strains. For the sake of simplicity, a linear softening damage law is applied[20]:

$$w = \begin{cases} 0 & \varepsilon_{\text{eq}} \leq f_t/E \\ 1 - \dfrac{f_t\,(2G_f/l_w - f_t\varepsilon_{\text{eq}})}{\varepsilon_{\text{eq}}\,(2EG_f/l_w - f_t^2)} & f_t/E < \varepsilon_{\text{eq}} \leq 2\Gamma/f_t \\ 1 & \text{otherwise} \end{cases} \tag{5.20}$$

The randomness of the simulation is induced by the random variable η. In principle, η should follow a Gauss-Weibull grafted distribution (Eqs. (1.24a) and (1.24b)). However, since our interest is limited to the size effect on the mean structural strength for small and intermediate size range, it is sufficient to assume that η follows a Gaussian distribution of whose mean equals 1, i.e.:

$$f_\eta(x) = \frac{1}{\sqrt{2\pi}\omega_0} e^{-(x-1)^2/2\omega_0^2} \tag{5.21}$$

In order to check the effect of randomness of fracture properties on the size effect on the mean structural strength, we consider different input CoVs ($\omega_0 = 0.15,\ 0.20,\ 0.25,\ 0.30,$ and 0.35). Since it is assumed that the autocorrelation length is smaller than the finite element size, each value of η is considered as independent. There is a slight chance ($< 1\%$) of sampling a negative value of η, which is discarded since its influence on the mean structural strength is minimal.

The stochastic simulations are performed on the open source software OOFEM [82, 83]. For these three loading configurations, the structural strengths can be defined using Eqs. (1.18) or (1.19) with the following values of c_n: $c_n = 1$ for uniaxial tensile specimens, $c_n = 6$ for bending specimen, and $c_n = 9$ for three-point-bending specimens, and the thickness b of the specimen is taken as 1 m. For each loading configuration, 100 realizations are generated to obtain the mean structural strength. By averaging the random simulation results, the size effect curves of the mean structural strength for each loading configuration and for each CoV value of η are obtained, which are used to calibrate the finite weakest-link model.

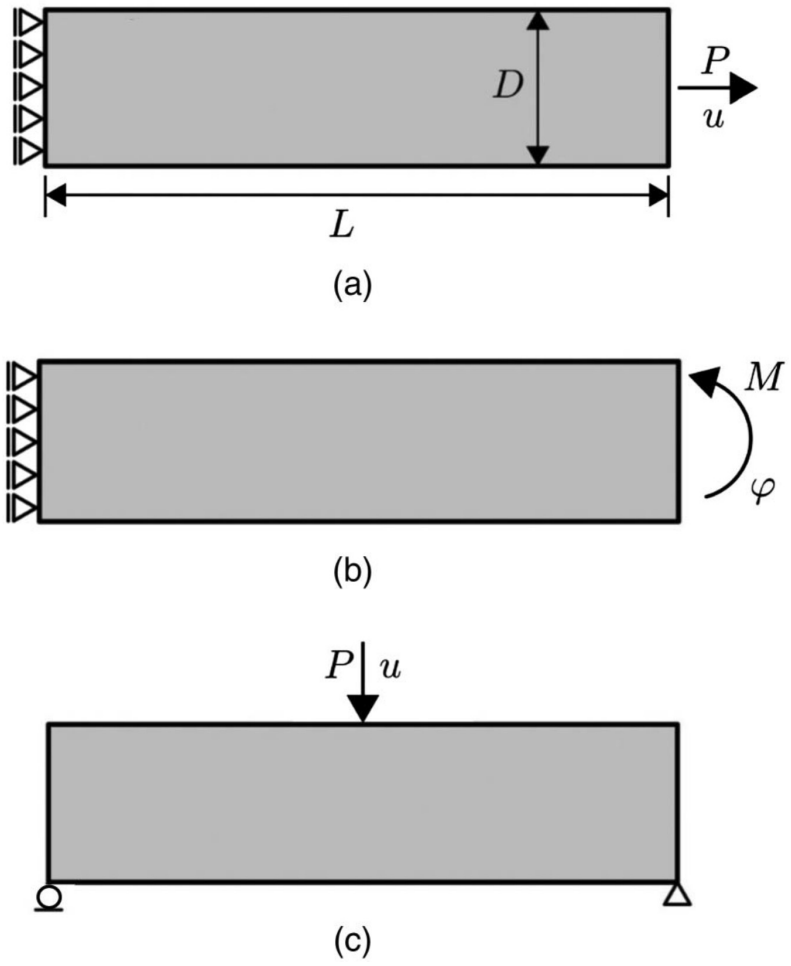

Figure 5.1: Specimens with three loading configurations:(a) uniaxial tension, (b) pure bending, and (c) three-point-bending.

5.4 Results and discussion

5.4.1 Size effect curves determined by stochastic simulations

As mentioned before, the stochastic simulations involve a number of combinations of the Irwin characteristic length l_{ch}, the crack band width l_w, and input CoV ω_0 of the random variable η. In this section, we will discuss how these three parameters affect the behavior of size effect on the mean structural strength, and whether there exists a single length scale l_c that governs this size effect, as proposed in Eq. (5.8).

The size effect curves of the mean structural strength are first presented in terms of the mean strength versus specimen size. In order to investigate the effect of l_w on the size effect on the mean structural strength, we first group these size effect curves with the same values of l_{ch} and ω_0 but different values of l_w. It is observed that these size effect curves have a similar qualitative behavior regardless of the values of different l_{ch} and different ω_0. As a demonstration, Figure 5.2 - Figure 5.4 present two groups of the simulated size effect curves of the mean structural strength ($l_{ch} = 333.33$ mm, $\omega_0 = 0.15$ and $l_{ch} = 333.33$ mm, $\omega_0 = 0.25$) with respect to all the three different loading configuration. It is clear that these size effect curves do not collapse together for different values of l_w, indicating l_w has an influence on the mean structural strength. This phenomenon can be explained by the random damage initiation sites. An increasing number of potential damage initiation sites will lead to a lower mean strength, which is the essential concept of statistical size effect of structural strength[76]. Since the total number of potential damage initiation sites is also influenced by applied stress field (i.e. loading configurations), it is expected that the influence of l_w on the mean structural size would also depend on the stress field. As shown in Figure 5.2 - Figure 5.4, the foregoing analysis is supported by the stochastic simulation results from the following three aspects:

- The mean structural strength always decreases with a decreasing l_w. This is

because a smaller l_w corresponds with a larger number of potential damage initiation sites in the specimen, decreasing the mean structural strength.

- The difference between these size effect curves for different l_w increases as the input CoV ω_0 increases. The larger value of ω_0 implies the higher randomness of the material fracture property, leading to a lower mean structural strength.

- It is observed that, among the three different loading configuration, the uniaxial tensile specimens exhibit the strongest effect of l_w on the size effect curve of the mean structural strength, while this effect decreases for bending specimens, and becomes the weakest for three-point-bending specimens. This is because, for uniaxial tensile specimens, the possible site of damage initiation location is evenly distributed on the entire structural domain, whereas for three-point-bending specimens, the damage initiation location is most likely limited in a zone around the mid-span of the bottom.

At this point, the length scale l_c (Eq. (5.8)) is introduced in order to express the size effect curve in a dimensionless form (i.e. ς_N vs d). As shown in Figure 5.5, for each input CoV ω_0, a certain value of α can be found to collapse the all these size effect curves onto a single dimensionless size effect curve. The calculation shows that the function $f(\omega_0)$ in Eq. (5.8) is approximately equal to one for all $f(\omega_0)$ and loading configurations.

Figure 5.6 presents the relationships between α and $f(\omega_0)$ for the three loading configurations. It is noted that α measures the relative dominance of l_{ch} and l_w on the size effect on the mean structural strength. A larger value of α implies that the mean structural strength is governed more by the Irwin characteristic length l_{ch} than the crack band width l_w. It can be observed that, for each loading configuration, α decreases with an increasing ω_0, which is consistent with the fact that the increasing of ω_0 implies a more significant effect of l_w on the mean structural strength. Likewise,

for a given ω_0, the α value is the highest for three-point-bending specimens, followed by the bending specimens and the uniaxial tensile specimens. From Figure 5.6, it is observed that the effect of l_{ch} on the size effect on the mean structural strength is much grater than that of l_w. This indicates that the non-linear fracture process governs the mean structural strength, which is in consistence with a well-established energetic scaling model [19, 15]. On the other hand, the present analysis also reveals that the size effect on the mean structural strength is also influenced by the crack band with and the applied stress field (i.e. loading configuration).

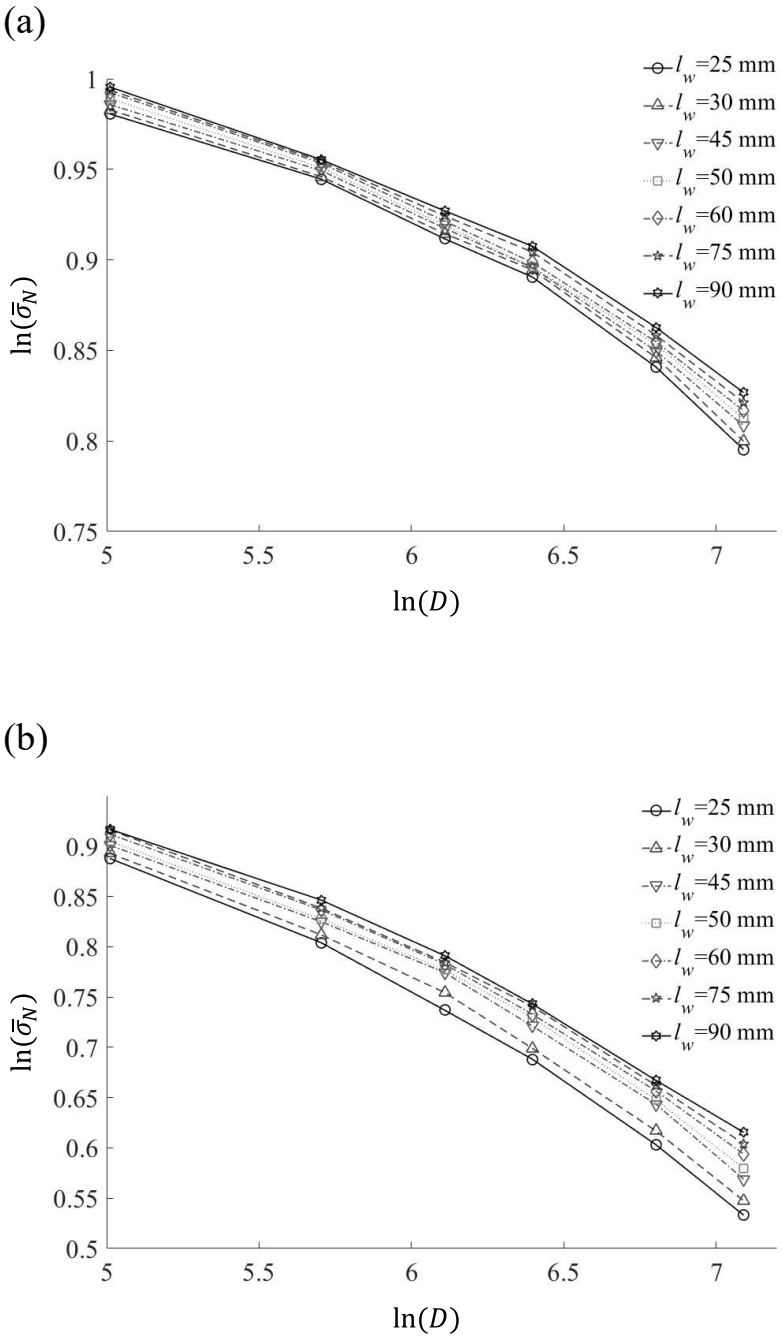

Figure 5.2: Simulated size effect curves of the mean structural strength for uniaxial tensile specimens: (a) $l_{ch} = 333.33$ mm, $\omega_0 = 0.15$; (b) $l_{ch} = 333.33$ mm, $\omega_0 = 0.25$.

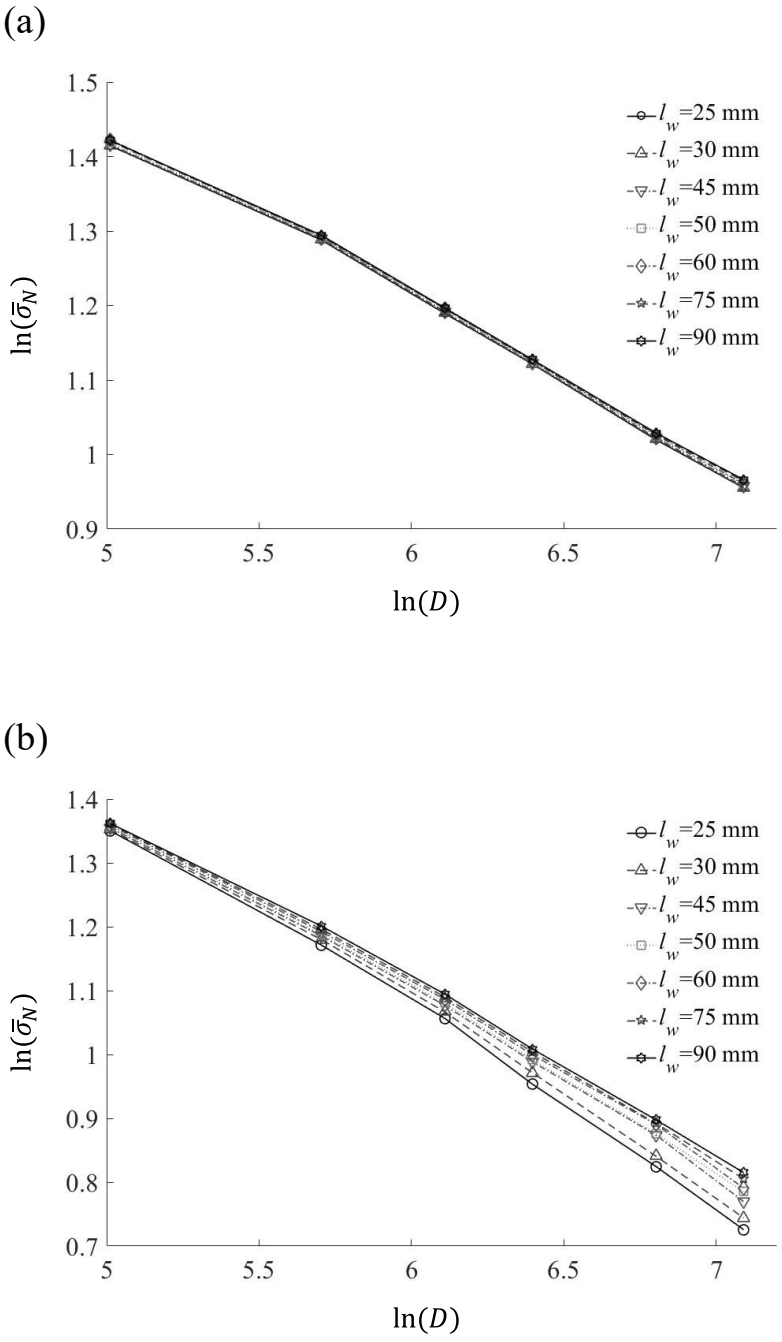

Figure 5.3: Simulated size effect curves of the mean structural strength for pure bending specimens: (a) $l_{ch} = 333.33$ mm, $\omega_0 = 0.15$; (b) $l_{ch} = 333.33$ mm, $\omega_0 = 0.25$.

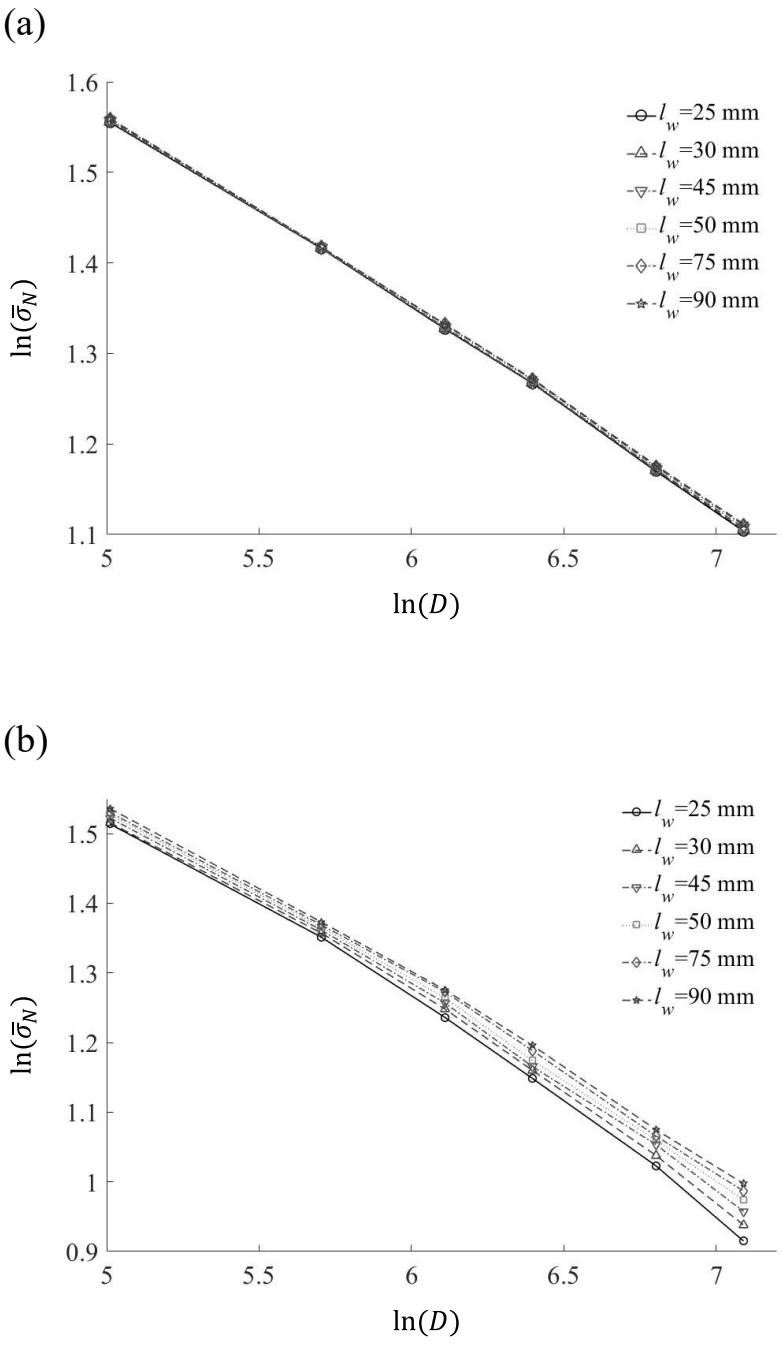

Figure 5.4: Simulated size effect curves of the mean structural strength for three-point-bending specimens: (a) $l_{ch} = 333.33$ mm, $\omega_0 = 0.15$; (b) $l_{ch} = 333.33$ mm, $\omega_0 = 0.25$.

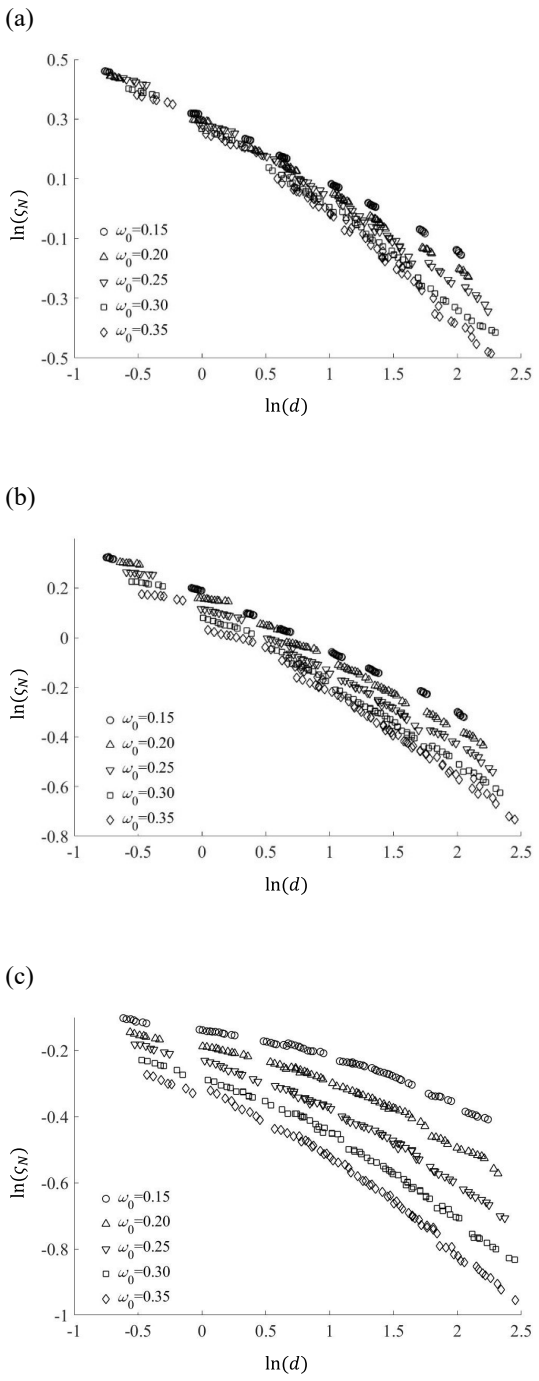

Figure 5.5: Replot of size effect curves in terms of dimensionless strength $\varsigma_N = \bar{\sigma}_N / \bar{f}_{\mathrm{t}}$ and relative size $d = D/l_c$: (a) uniaxial tensile specimens; (b) pure bending specimens; (c) three-point-bending specimens.

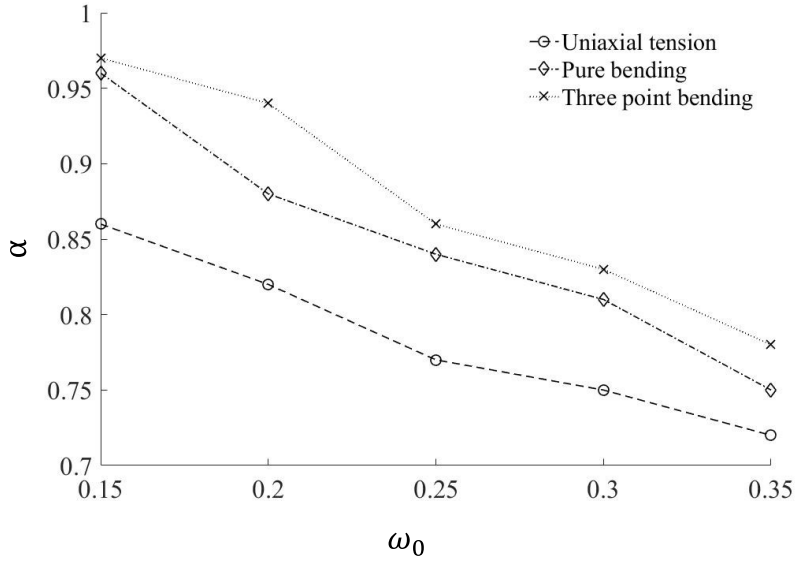

Figure 5.6: Relationship between parameter α and the input COV ω_0.

5.4.2 Determination of RVE size

Now we match the size effect curves of the mean structural strength calculated from the stochastic simulations with the corresponding results predicted by the finite weakest-link model (Eqs. (5.9) and (5.11)), from which the relative RVE size ℓ_0 and the CoV of RVE strength ω_G can be determined. As indicated by Eq. (5.13), the range of relative size for the fitting (i.e. $d \in [d_1, d_2]$) should be determined first. In the study of this chapter, we choose $d_1 = 2$ and $d_2 = 4$. Figure 5.7 plots the optimum fitting of the simulated size effect curves of the mean structural strength by the finite weakest-link model. From Figure 5.7, we can see that, even though $d_2 = 4$ was chosen for the fitting process, the two models agree reasonably well with each other even for $d_2 = 6$, which demonstrates that the fitting result will be affected minimally if a larger value of d_2 is used. It is found that, for all the three loading configurations, the non-linear stochastic simulation predicts a size effect curve bending towards a horizontal line at the small size asymptote[14, 15]. Such a trend is not observed in the finite weakest-link model due to the fact that the model is inapplicable when the specimen size is smaller than one RVE size. Howerver, such a horizontal small-size asymptote of the size effect on the mean structural strength can be well captured by the first-passage model [101]. For all the cases, unique solutions for Eqs. (5.14) and (5.15) are obtained. As a demonstration, Figure 5.8 presents the contour plot of the value of H (Eq. (5.13)) for $\omega_0 = 0.25$, which indicates that uniqueness of the solution.

Figure 5.9 shows the calibrated values of the relative RVE size ℓ_0 for all the three loading configurations and different input CoV ω_0. It is seen that the RVE size l_0 is on the same order of the Irwin characteristic length l_c. For a given loading configuration, ℓ_0 is a monotonic decreasing function of ω_0, which is because the increase of ω_0 would increase the randomness of the material strength, weaken the overall structural strength. On the other hand, for a fixed size structure, a smaller RVE size leads to more RVEs and more potential failure sites, which also decreases the over structural

strength. Furthermore, we observe that the decreasing in ℓ_0 is less significant for three-point-bending specimens as compared to uniaxial tensile specimens. This is because the effect of the input CoV ω_0 on the mean strength of three-point-bending specimens is less pronounced than that on uniaxial tensile specimens due to the significant non-uniformity of the stress field. From Figure 5.9, it is found that, for a given input CoV ω_0, the relative RVE size ℓ_0 strongly depends on the loading configuration. This is because of the weakest-link model employs the elastic stress field in the calculation of the material failure probability (1.22), and ℓ_0 is calculated such that the finite weakest-link model would yield the same size effect curve of the mean structural strength as predicted by non-linear stochastic simulations. As a result, we expect that the ℓ_0 value would depend on the loading configuration or specimen geometry. In terms of the stress field, it is consider that the bending specimens represent an intermediate case between the uniaxial tensile specimens and three-point-bending specimens. Therefore, it is seen that the ℓ_0 for bending specimens is bounded between that of the tensile specimens and the three-point-bending specimens.

Figure 5.10 presents the relationship between the CoV of RVE strength ω_G and the input CoV ω_0 for all the three loading configurations. Obviously, ω_G is a monotonic function of ω_0. This is also due to the adoption of elastic stress field in the finite weakest-link model for matching the results of non-linear simulations. As a result, the ω_G values for bending specimens are in between those for uniaxial tensile specimens and the three-point-bending specimens.

From the foregoing analysis, we show that the RVE size of the finite weakest-link model can be related to two material length scales, i.e. the Irwin characteristic length and the crack band width. This relationship (Eq. (5.17)) also depends on the stress field, which indicates that the RVE size is not a material length scale but a structural property. It is worthwhile to briefly comment the finite weakest-link model in view of the present analysis. The finite weakest-link model contains a qualitative

description of some essential failure mechanisms of quasi-brittle structures, such as macroscopic damage localization and damage redistribution inside the fracture process zone. However, the computation of the structural strength distribution using the finite weakest-link model is based the elastic stress field, which is unable to quantitatively capture the actual non-linear stress redistribution and damage localization mechanism. As a result, the RVE size of the finite weakest-link model is a structural property, because the model employs the elastic stress field rather than the actual stress field that the structure experiences when failure occur.

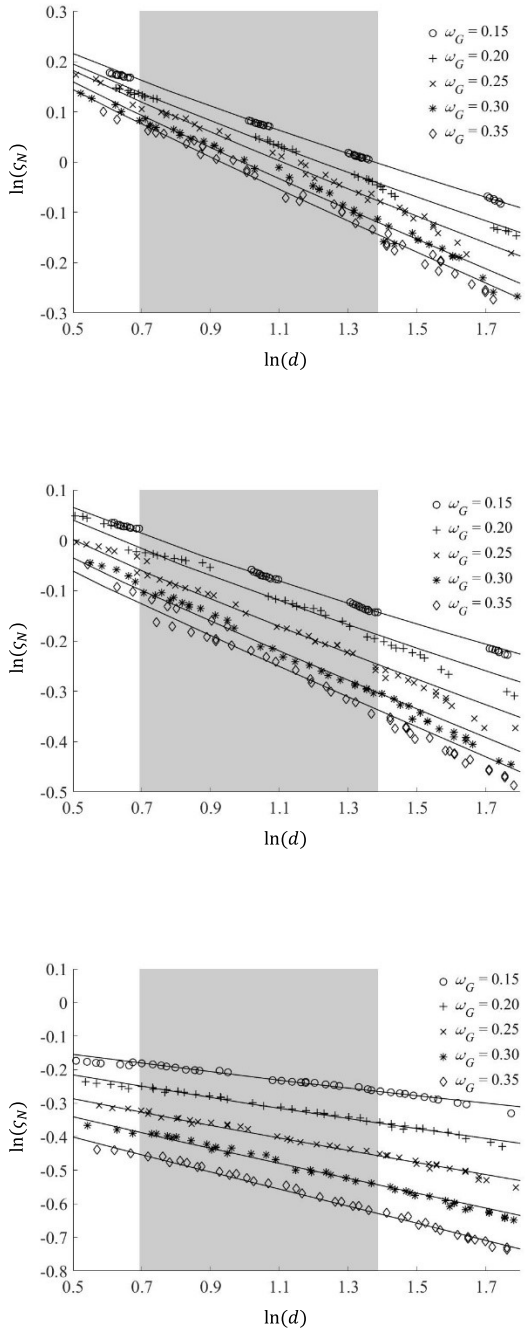

Figure 5.7: Optimum fitting of the dimensionless size effect curves by the finite weakest-link model: (a) uniaxial tensile specimens, (b) pure bending specimens, (c) three-point-bending specimens.

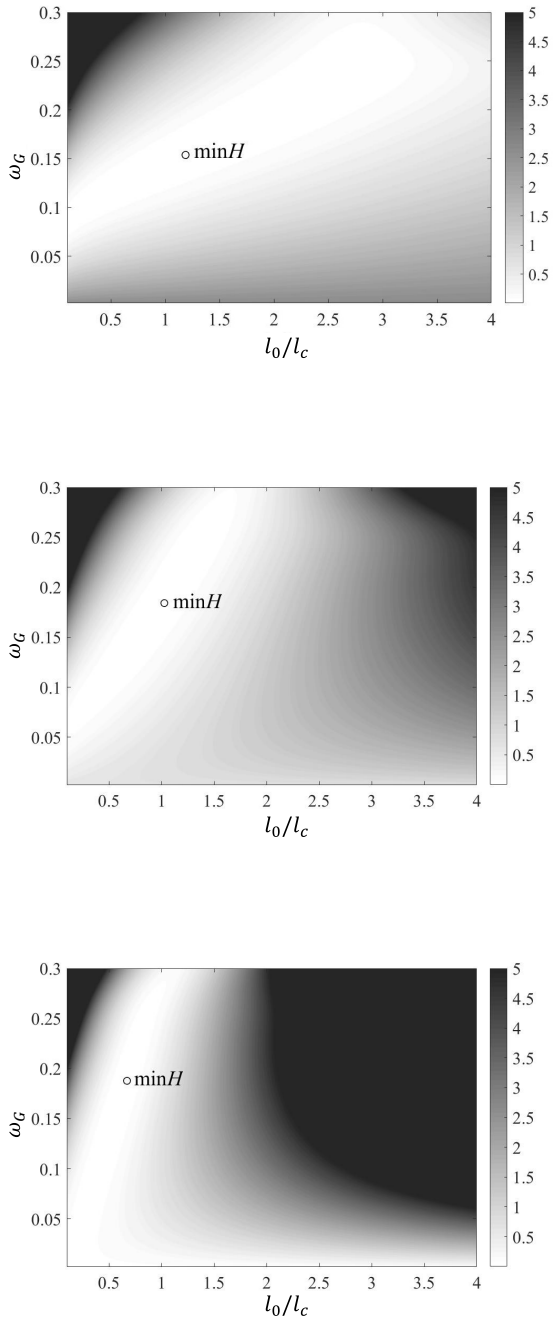

Figure 5.8: Contour plot of the value of function $H(\ell_0, \omega_G)$: (a) uniaxial tensile specimens, (b) pure bending specimens, (c) three-point-bending specimens

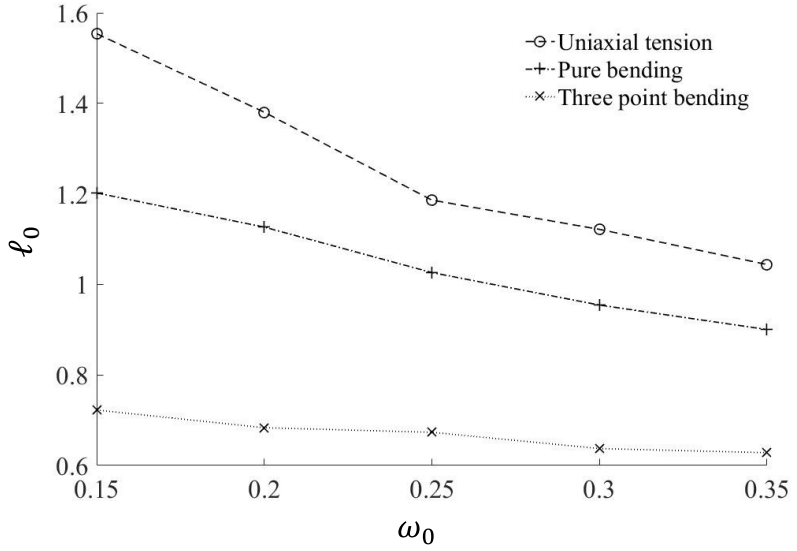

Figure 5.9: Relationships between the relative RVE size ℓ_0 and the input COV ω_0 for all three loading configurations.

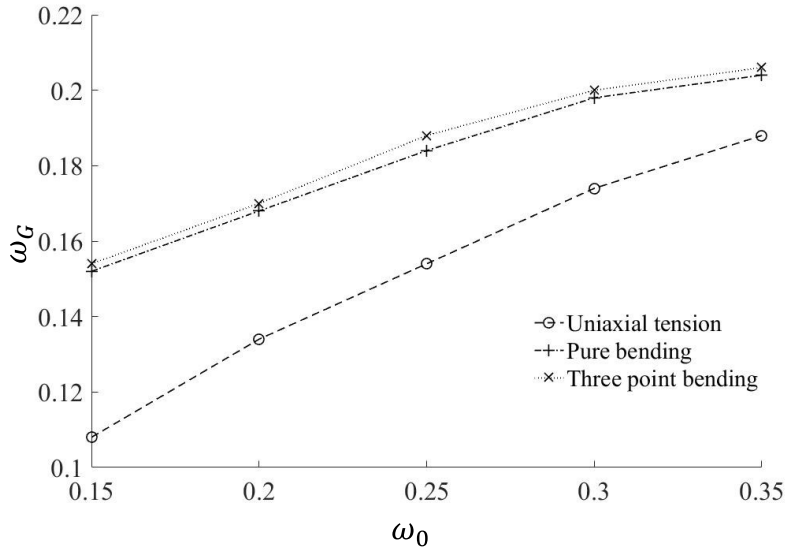

Figure 5.10: Relationships between the COV of RVE strength ω_G and the input COV ω_0 for all three loading configurations.

5.5 Conclusions

In this chapter, the relationship between the RVE size and two material length scales, which are the Irwin characteristic length and the crack band width, is investigated. Through the dimensional analysis, we first determined the functional form of the RVE size as a function of both the Irwin characteristic length and the crack band width. By matching the size effect curves of stochastic finite element simulations and the finite weakest-link model, the relationship among the RVE size, the Irwin characteristic length and the crack band width are determined quantitatively.

It is shown that the size effect on the mean structural strength is influenced by both the Irwin characteristic length and the crack band width, and the relative dominance of these two length scales depends on the loading configuration.

The RVE size is related to both the Irwin characteristic length and the crack band width, whose relationship depends on the loading configuration. Therefore, the RVE size is not a material property, but a structural property.

Chapter 6

Conclusions

In this research, two new probabilistic models are proposed for strength distributions of brittle and quasi-brittle structures. The first model is a continuous probabilistic model based on first-passage analysis of random fields, which is referred to as the first-passage model. The model is first formulated using a 1-dimensional description for the strength statistics of poly-Si MEMS structures, and is later generalized to higher dimensions for investigating the power-law behavior of strength distribution of brittle and quasi-brittle materials. The second model is a renewal weakest-link model for poly-Si MEMS structures. The model considers the random number of potential failure sites in the specimen. Lastly, the relation between the internal length scale of the finite weakest-link model and the material properties is studied through the analysis of the size effect on the mean structural strength. The following conclusions are drawn based on this study:

(1) The first-passage model is able to realistically incorporate the detailed statistical information of the random fields of both material strength and applied stress. Depending on the specimen geometry and the loading configuration, the failure statistics of the specimen can be described by either a stationary random field or a uniformly modulated non-stationary random field. The overall failure risk of the structure can be evaluated through the first-passage analysis. The model is validated by the com-

parison with the measured strength distributions of uniaxial tensile poly-Si MEMS specimens of two gauge lengths.

(2) The first-passage model yields intricate size effects on both the structural strength distribution and the mean structural strength. It predicts that the structural strength distribution transits from a non-Weibull distribution with a power-law tail to a primary Weibull distribution as the structure size increases. Due to the consideration of the autocorrelated features of the random stress field and the random strength fields, the model is able to yield a horizontal small-size asymptote of the size effect curve of the mean structural strength. At the large-size limit, the size effect curve approaches the classical Weibull size effect.

(3) It is demonstrated that the first-passage model is a generalization of the finite weakest-link model. Compared to the finite weakest-link model, the first-passage model is able to account for the spatially correlated features of the random applied stress and the random materials strength. Meanwhile, it is shown that the RVE size of the weakest-link model is directly related to the autocorrelation length of the random field governing material failure.

(4) The renewal weakest-link is able to incorporate the detail statistical information of the random side-wall geometry of the MEMS structures within the weakest-link modeling framework. It is shown that the renewal weakest-link model is able to yield accurate predictions on the strength distributions of specimens of different sizes, using the same model parameters.

(6) It is shown that the renewal weakest-link model can be approximated by an equivalent weakest-link model, which relies only on the average number of surface grooves and the expected reliability function of each groove. This simplification makes the renewal weakest-link model as computational efficient as the conventional weakest-link model.

(7) Through the generalized n-dimensional first-passage model, it is shown that,

regardless of the dimensionality of the analysis and the type of random stress field, the distribution of structural strength always exhibits a power-law tail, which is consistent with the observed Weibull strength distribution of large-size structures.

(8) The exponent of the power-law tail of structural strength distribution is primarily governed by the Weibull modulus of the left tail of the material strength, which is also mildly affected by the dimensionality of the analysis and the applied stress field. This indicates that the origin of the power-law functional form of the left tail distribution of structural strength is the thermally activated stress-driven motion of the nanocrack tip, which can be described by the transition rate theory. Though the consideration of flaw statistics is necessary for capturing the randomness of the overall failure statistics, it does not dictate the power-law form of the left tail of structural strength distribution.

(9) The RVE size of the finite weakest-link model can be determined by matching the size effect curve of the mean structural strength predicted by the stochastic finite element simulations and that yielded from the finite weakest-link model. It is showed that the RVE size is related to both the Irwin characteristic length and the crack band width, which are two material length scales. The relationship among the RVE size, the Irwin characteristic length and the crack band width also depends on the loading configuration (applied stress field). This indicates that the RVE size is a not a material property, but a structural property.

References

[1] P. Abrahamsen. *A Review of Gaussian Random Fields and Correlation Functions*. Norsk Regnesentral/Norwegian Computing Center, 1997.

[2] M. Abramowitz and I. A Stegun. *Handbook of Mathematical Functions: With Formulas, Graphs, and Mathematical Tables*, volume 55. Courier Corporation, 1964.

[3] R. J. Adler. On excursion sets, tube formulas and maxima of random fields. *Ann. Appl. Prob.*, pages 1–74, 2000.

[4] R. J. Adler, AM Hasofer, et al. Level crossings for random fields. *Ann. Probab.*, 4(1):1–12, 1976.

[5] R. J. Adler and J. E. Taylor. *Random Fields and Geometry*. Springer Science & Business Media, 2009.

[6] A. H. S. Ang and W. H. Tang. *Probability Concepts in Engineering Planning and Design. Vol II. Decision, Risk and Reliability*. J. Wiley, New York, 1984.

[7] G. Augusti, A. Baratta, and F. Casciati. *Probabilistic methods in structural engineering*. CRC Press, 1984.

[8] B. M. Ayyub and R. H. McCuen. *Probability, statistics, and reliability for engineers and scientists*. CRC press, 2016.

[9] I. Barany, V. Vu, et al. Central limit theorems for gaussian polytopes. *Ann. Probab.*, 35(4):1593–1621, 2007.

[10] G. I. Barenblatt. *Scaling, Self-Similarity, and Intermediate Asymptotics*. Cambridge University Press, Cambridge, 1996.

[11] G. I. Barenblatt. *Scaling*. Cambridge University Press, Cambridge, 2003.

[12] Z. P. Bažant. Scaling of quasibrittle fracture: Asymptotic analysis. *Int. J. Frac.*, 83(1):19–40, 1997.

[13] Z. P. Bažant. Probability distribution of energetic-statistical size effect in quasibrittle fracture. *Prob. Engrg. Mech.*, 19(4):307–319, 2004.

[14] Z. P. Bažant. Scaling theory of quaisbrittle structural failure. *Proc. Nat'l. Acad. Sci., USA*, 101(37):13400–13407, 2004.

[15] Z. P. Bažant. *Scaling of Structural Strength.* Elsevier, London, 2005.

[16] Z. P. Bažant and M. Jirásek. Nonlocal integral formulations of plasticity and damage: Survey of progress. *J. Engrg. Mech., ASCE*, 128(11):1119–1149, 2002.

[17] Z. P. Bažant and J.-L. Le. *Probabilistic Mechanics of Quasibrittle Structures: Strength, Lifetime, and Size Effect.* Cambridge University Press, Cambridge, U.K., 2017.

[18] Z. P. Bažant, J.-L. Le, and M. Z. Bazant. Scaling of strength and lifetime distributions of quasibrittle structures based on atomistic fracture mechanics. *Proc. Nat'l. Acad. Sci., USA*, 106:11484–11489, 2009.

[19] Z. P. Bažant and Z. Li. Modulus of rupture: Size effect due to fracture initiation in boundary layer. *J. Struct. Engrg., ASCE*, 121(4):739–746, 1995.

[20] Z. P. Bažant and B.-H. Oh. Crack band theory for fracture of concrete. *Mater. Struc.*, 16:155–177, 1983.

[21] Z. P. Bažant and J. Ožbolt. Nonlocal microplane model for fracture, damage, and size effect in structures. *J. Engrg. Mech., ASCE*, 116(11):2485–2505, 1990.

[22] Z. P. Bažant and S. D. Pang. Mechanics based statistics of failure risk of quasibrittle structures and size effect on safety factors. *Proc. Nat'l. Acad. Sci., USA*, 103:9434–9439, 2006.

[23] Z. P. Bažant and S. D. Pang. Activation energy based extreme value statistics and size effect in brittle and quasibrittle fracture. *J. Mech. Phys. Solids.*, 55:91–134, 2007.

[24] Z. P. Bažant and J. Planas. *Fracture and Size Effect in Concrete and Other Quasibrittle Materials.* CRC Press, Boca Raton, 1998.

[25] Z. P. Bažant and J.-L. Le. *Probabilistic mechanics of quasibrittle structures: strength, lifetime, and size effect.* Cambridge University Press, 2017.

[26] Z. P. Bažant, J.-L. Le, and M. Z. Bazant. Scaling of strength and lifetime probability distributions of quasibrittle structures based on atomistic fracture mechanics. *Proc. Natl. Acad. Sci. U.S.A.*, 106(28):11484–11489, 2009.

[27] Z. P. Bažant and B. H. Oh. Crack band theory for fracture of concrete. *Matériaux et construction*, 16(3):155–177, 1983.

[28] Z. P. Bažant and G. Pijaudier-Cabot. Measurement of characteristic length of nonlocal continuum. *J. Engrg. Mech., ASCE*, 115(4):755–767, 1989.

[29] B. L. Boyce, R. Ballarini, and I. Chasiotis. An argument for proof testing brittle microsystems in high-reliability applications. *J. Micromech. Microeng.*, 18:117001, 2008.

[30] B. L. Boyce, J. M. Grazier, T. E. Buchheit, and M. J. Shaw. Strength distributions in polycrystalline silicon MEMS. *J. Microelectromech. Syst.*, 16(2):179–190, 2007.

[31] E. Buckingham. On physically linear systems; illustration of the use of dimensional equations. *Phys. Rev. Ser. 2*, IV(4):345–376, 1914.

[32] E. Buckingham. Model experiments and the form of empirical equations. *Trans. ASME*, 37:263–296, 1915.

[33] A. Carpinteri. Stress-singularity and generalized fracture toughness at the vertex of reentrant corners. *Engrg. Frac. Mech.*, 26:143–155, 1987.

[34] E. Castillo. *Extreme value theory in engineering*. Elsevier, 2012.

[35] D. R. Cox. *Renewal theory*. Methuen, 1962.

[36] Harald Cramér and M Ross Leadbetter. *Stationary and related stochastic processes: Sample function properties and their applications*. Courier Corporation, 2013.

[37] G. Deodatis. Non-stationary stochastic vector processes: seismic ground motion applications. *Prob. Engrg. Mech.*, 11:149–168, 1996.

[38] O. Ditlevsen and H. O. Madsen. *Structural reliability methods*, volume 178. Wiley New York, 1996.

[39] S. M.-M. Dubois, G.-M. Rignanese, T. Pardoen, and J.-C. Charlier. Ideal strength of silicon: An ab initio study. *Phys. Rev. B*, 74:235203, 2006.

[40] K. Duckett. Risk analysis and the acceptable probability of failure. *The Structural Engineering*, 83(15):25–26, 2005.

[41] R. M. Dudley and R. M. Dudley. *Uniform central limit theorems*. Number 63. Cambridge university press, 1999.

[42] M. L. Dunn, W. Suwito, and S. J. Cunningham. Fracture initiation at sharp notches: Correlation using critical stress intensities. *Int. J. Solids Struct.*, 34(29):3873–3883, 1997.

[43] Isaac E. *Probabilistic Methods in the Theory of Structures: Strength of Materials, Random Vibrations, and Random Buckling*. World Scientific, 2017.

[44] J. Eliáš, M. Vořechovský, J. Skoček, and Z. P. Bažant. Stochastic discrete meso-scale simulations of concrete fracture: Comparison to experimental data. *Engrg. Fract. Mech.*, 135(1):1–16, 2015.

[45] HD. Espinosa, B. Peng, N. Moldovan, TA. Friedmann, X. Xiao, DC. Mancini, O. Auciello, J. Carlisle, and CA. Zorman. A comparison of mechanical properties of three mems materials-silicon carbide, ultrananocrystalline diamond, and hydrogen-free tetrahedral amorphous carbon (ta-c). In *11th International Conference on Fracture 2005, ICF11*, 2005.

[46] Augusto C. Falchetto, J.-L. Le, M. I. Turos, and M. O. Marasteanu. Indirect determination of size effect on strength of asphalt mixtures at low temperatures. *Mater. Struct.*, 47(1-2):157–169, 2014.

[47] L. Faravelli. Response-surface approach for reliability analysis. *J. Engrg. Mech., ASCE*, 115(12):2763–2781, 1989.

[48] F. J. Ferrante, S. R. Arwade, and L. L. Graham-Brady. A translational model for non-stationary, non-Gaussian random processes. *Prob. Engrg. Mech.*, 20:215–228, 2005.

[49] R. A. Fisher and L. H. C. Tippett. Limiting form of the frequency distribution the largest and smallest number of a sample. *Proc. Cambridge Philos. Soc.*, 24:180–190, 1928.

[50] A. M. Fitzgerald, D. M. Pierce, B. M. Huigens, and C. D. White. A general methodology to predict the reliability of single-crystal silicon MEMS devices. *J. Microelectromech. Syst.*, 18(4):962–970, 2009.

[51] M. Fréchet. Sur les ensembles compacts de fonctions mesurables. *Fund. Math.*, 9(1):25–32, 1927.

[52] A. M. Freudenthal. Statistical approach to brittle fracture. In *Fracture: An Advanced Treatise, vol. 2*, pages 591–619, New York, 1968.

[53] Y. Fu, H. Du, W. Huang, S. Zhang, and M. Hu. Tini-based thin films in mems applications: a review. *Sens. Actuators, A*, 112(2-3):395–408, 2004.

[54] F. J. Gomez and M. Elices. A fracture criterion for sharp V-notched samples. *Int. J. Frac.*, 123(3-4):163–175, 2003.

[55] P. Grassl and Z. P. Bažant. Random lattice-particle simulation of statistical size effect in quasi-brittle structures failing at crack initiation. *J. Engrg. Mech., ASCE*, 135(2):85–92, 2009.

[56] M. Grigoriu. Crossings of non-Gaussian translation processes. *J. Engrg. Mech., ASCE*, 110(4):610–620, 1984.

[57] M. Grigoriu. Simulation of stationary non-gaussian translation processes. *J. Engrg. Mech., ASCE*, 124(2):121–126, 1998.

[58] B. Gross. Least squares best fit method for the three parameter weibull distribution: analysis of tensile and bend specimens with volume or surface flaw failure. *NASA Technical Report*, TM-4721:1–21, 1996.

[59] E. J. Gumbel. *Statistics of Extremes*. Columbia University Press, New York, 1958.

[60] S. S. Hazra, M. S. Baker, J. L. Beuth, and M. P. de Boer. Demonstration of an in-situ on-chip tester. *J. Micromech. Microeng.*, 19:082001 (5 pp.), 2009.

[61] R. Hill. Elastic properties of reinforced solids: some theoretical principles. *J. Mech. Phys. Solids*, 11:357–362, 1963.

[62] H. Kim and M.D. Shields. Modeling strongly non-Gaussian non-stationary stochastic processes using the Iterative Translation Approximation method and Karhunen-Loeve expansion. *Comp. Struct.*, 161:31–42, 2015.

[63] S. Kotz and S. Nadarajah. *Extreme value distributions: theory and applications*. World Scientific, 2000.

[64] V. G. Kulkarni. *Modeling and analysis of stochastic systems*. Chapman and Hall/CRC, 2016.

[65] J.-L. Le, R. Ballarini, and Z. Zhu. Modeling of probabilistic failure of polycrystalline silicon MEMS structures. *J. Amer. Cer. Soc.*, 98(6):1685–1697, 2015.

[66] J.-L. Le and Z. P. Bažant. Strength distribution of dental restorative ceramics: Finite weakest link model with zero threshold. *Dent. Mater.*, 25(5):641–648, 2009.

[67] J.-L. Le, Z. P. Bažant, and M. Z. Bazant. Unified nano-mechanics based probabilistic theory of quasibrittle and brittle structures: I. Strength, crack growth, lifetime and scaling. *J. Mech. Phys. Solids.*, 59:1291–1321, 2011.

[68] J.-L. Le, A. Cannone Falchetto, and M. O. Marasteanu. Determination of strength distribution of quasibrittle structures from mean size effect analysis. *Mech. Mater.*, 66:79–87, 2013.

[69] J.-L. Le, J. Eliáš, and Z. P. Bažant. Computation of probability distribution of strength of quasibrittle structures failing at macrocrack initiation. *J. Engrg. Mech., ASCE*, 138(7):888–899, 2011.

[70] J.-L. Le and J. Eliáš. A probabilistic crack band model for quasibrittle fracture. *J. Appl. Mech. ASME*, 83(5):051005, 2016.

[71] J.-L. Le, A. C. Falchetto, and M. O. Marasteanu. Determination of strength distribution of quasibrittle structures from mean size effect analysis. *Mech. Mater.*, 66:79–87, 2013.

[72] J.-L. Le, M. Pieuchot, and R. Ballarini. Effect of stress singularity magnitude on scaling of strength of quasibrittle structures. *J. Engrg. Mech., ASCE*, 140(5):04014011, 2014.

[73] J.-L. Le, Z. Xu, and J. Eliáš. Internal length scale of weakest-link statistical model for quasi-brittle fracture. *J. Engrg. Mech., ASCE*, 144(4):04018017, 2018.

[74] D. Leguillon. Strength or toughness? A criterion for crack onset at a notch. *Eur. J. Mech., A/Solids*, 21:61–72, 2002.

[75] T. S. Lin and R. B. Corotis. Reliability of ductile systems with random strengths. *J. Struct. Eng., ASCE*, 111(6):1306–1325, 1985.

[76] E. Mariotte. *Traité du mouvement des eaux, posthumously edited by M. de la Hire; Eng. Transl. by J. T. Desvaguliers, London (1718), p. 249; also Marriotte's collected works, 2nd ed., The Hague (1740).* 1686.

[77] J. Mazars. *Application de la mécanique de l'endommagement au comportement non linéaire et à la rupture du béton de structure.* PhD thesis, Univ. Paris VI, Paris, France, 1984.

[78] M. Mehregany and C. A. Zorman. Sic mems: opportunities and challenges for applications in harsh environments. *Thin solid films*, 355:518–524, 1999.

[79] Nordic Committee for Building Structures (NKB). Recommendation for loading and safety regulations for structural design. Technical Report 36, 1978.

[80] A. S. Nowak and K. R. Collins. *Reliability of structures*. CRC Press, 2012.

[81] S.-D. Pang, Z. P. Bažant, and J.-L. Le. Statistics of strength of ceramics: Finite weakest link model and necessity of zero threshold. *Int. J. Frac.*, 154:131–145, 2008.

[82] B. Patzák. OOFEM-an object-oriented simulation tool for advanced modeling of materials and structures. *Acta Polytechnica*, 52:59–66, 2012.

[83] B. Patzák and D. Rypl. Object-oriented, parallel finite element framework with dynamic load balancing. *Advances in Engineering Software*, 47:35–50, 2012.

[84] E. D. Reedy Jr. Singular stress fields at the intersection of a grain boundary and a stress-free edge in a columnar polycrystal. *J. Appl. Mech. ASME*, 78:014502, 2011.

[85] E. D. Reedy, Jr., B. L. Boyce, J. W. Foulk, III, R. V. Field Jr., M. P. de Boer, and S. S. Hazra. Predicting fracture in micrometer-scale polycrystalline silicon MEMS structures. *J. Microelectromech. Syst.*, 20(4):922–932, 2011.

[86] S. O. Rice. Mathematical analysis of random noise. *Bell Labs Technical Journal*, 23(3):282–332, 1944.

[87] B. D. Ripley. *Spatial statistics*, volume 575. John Wiley & Sons, 2005.

[88] M. E. Saleh, J. L. Beuth, and M. P. de Boer. Validated prediction of the strength size effect in polycrystalline silicon using the three-parameter weibull function. *J. Am. Ceram. Soc.*, 97(12):3982–3990, 2014.

[89] A. Seweryn. Brittle fracture criterion for structures with sharp notches. *Engrg. Fract. Mech.*, 47:673–681, 1994.

[90] M. Shinozuka and G. Deodatis. Simulation of multi-dimensional Gaussian stochastic fields by spectral representation. *Appl. Mech. Rev. ASME*, 49:29–53, 1996.

[91] B. W. Silverman. *Density estimation for statistics and data analysis*. Routledge, 2018.

[92] J. J. Sniegowski and M. P. De Boer. Ic-compatible polysilicon surface micromachining. *Annu. Rev. Mater. Sci.*, 30(1):299–333, 2000.

[93] T. Tsuchiya, O. Tabata, J. Sakata, and Y. Taga. Specimen size effect on tensile strength of surface-micromachined polycrystalline silicon thin films. *J. Microelectromech. Syst., IEEE*, 7(1):106–113, 1998.

[94] E. Vanmarcke. On the distribution of the first-passage time for normal stationary random processes. *J. Appl. Mech. ASME*, 42:215–220, 1975.

[95] E. Vanmarcke. *Random Fields Analysis and Synthesis*. World Scientific Publishers, Singapore, 2010.

[96] M. Vořechovský. Incorporation of statistical length scale into weibull strength theory for composites. *Comp. Struct.*, 92(9):2027–2034, 2010.

[97] W. Weibull. The phenomenon of rupture in solids. *Proc. Royal Sweden Inst. Engrg. Res.*, 153:1–55, 1939.

[98] W. Weibull. A statistical distribution function of wide applicability. *J. Appl. Mech. ASME*, 153(18):293–297, 1951.

[99] A. Witvrouw and A. Mehta. The use of functionally graded poly-sige layers for mems applications. In *Materials science forum*, volume 492, pages 255–260. Trans Tech Publ, 2005.

[100] Z. Xu, R. Ballarini, and J.-L. Le. A renewal weakest-link model of strength distribution of polycrystalline silicon mems structures. *J. Appl. Mech. ASME*, pages 1–26, 2019.

[101] Z. Xu and J.-L. Le. A first passage model for probabilistic failure of polycrystalline silicon MEMS structures. *J. Mech. Phys. Solids*, 99:225–241, 2017.

[102] Z. Xu and J.-L. Le. On power-law tail distribution of strength statistics of brittle and quasibrittle structures. *Eng. Fract. Mech.*, 197:80–91, 2018.

[103] K. Yasutake, M. Iwata, K. Yoshii, M. Umeno, and H. Kawabe. Crack healing and fracture strength of silicon crystals. *J. Mater. Sci.*, 21(6):2185–2192, 1986.

vita

Born in Wuhan, Hubei Province, China, Zhifeng Xu obtained his Bachelor of Science in Civil Engineering and Master of Science in Structural Engineering from Huazhong University of Science and Technology in 2012 and 2015, respectively. In 2015, he started his doctoral studies in Civil Engineering focusing on structural mechanics at University of Minnesota under Professor Jia-Liang Le's advisership. His research interests include: probabilistic mechanics, fracture mechanics, structural reliability, and probabilistic modeling. His journal publications include:

1. Z. Xu, R. Ballarini, and J.-L. Le. A Renewal weakest-link model of strength distribution of polycrystalline silicon MEMS structures. Journal of Applied Mechanics, In press.

2. J.-L. Le, and Z. Xu. A simplified probabilistic model for nanocrack propagation and its implications for tail distribution of structural strength. Physical Mesomechanics 21.6 (2018).

3. Z. Xu, and J.-L. Le. On power-law tail distribution of strength statistics of brittle and quasi-brittle structures. Engineering Fracture Mechanics 197 (2018): 80-91.

4. J.-L. Le, Z. Xu, and J. Eliáš. Internal length scale of weakest-link statistical model for quasi-brittle fracture. Journal of Engineering Mechanics 144.4 (2018): 04018017.

5. Z. Xu and J.-L. Le. A first passage model for probabilistic failure of polycrystalline silicon MEMS structures. Journal of the Mechanics and Physics of Solids, 99 (2017): 225-241.